

Fall 2017

# Nano/Submicro-Structured Iron Cobalt Oxides Based Materials for Energy Storage Application

Hongyan Gao

Western Kentucky University, hongyan.gao408@topper.wku.edu

Follow this and additional works at: <https://digitalcommons.wku.edu/theses>

 Part of the [Inorganic Chemistry Commons](#), [Materials Chemistry Commons](#), and the [Other Materials Science and Engineering Commons](#)

---

## Recommended Citation

Gao, Hongyan, "Nano/Submicro-Structured Iron Cobalt Oxides Based Materials for Energy Storage Application" (2017). *Masters Theses & Specialist Projects*. Paper 2057.  
<https://digitalcommons.wku.edu/theses/2057>

This Thesis is brought to you for free and open access by TopSCHOLAR®. It has been accepted for inclusion in Masters Theses & Specialist Projects by an authorized administrator of TopSCHOLAR®. For more information, please contact [topscholar@wku.edu](mailto:topscholar@wku.edu).

NANO/SUBMICRO-STRUCTURED IRON COBALT OXIDES BASED MATERIALS  
FOR ENERGY STORAGE APPLICATION

A Thesis  
Presented to  
The Faculty of the Department of Chemistry  
Western Kentucky University  
Bowling Green, Kentucky


In Partial Fulfillment  
Of the Requirements for the Degree  
Master of Science

By  
Hongyan Gao

December 2017

NANO/SUBMICRO-STRUCTURED IRON COBALT OXIDES BASED MATERIALS  
FOR ENERGY STORAGE APPLICATION

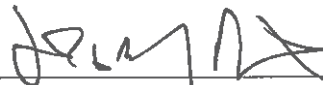
Date Recommended 10/30/17



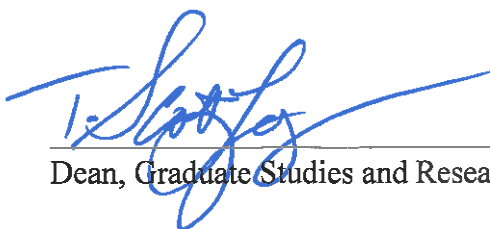
Dr. Yan Cao, Director of Thesis



Dr. Bangbo Yan



Dr. Jeremy Maddox



Dean, Graduate Studies and Research

11/6/17

Date

I dedicate this thesis to my family, Guoan Gao, Junru Zhou, Hongyu Gao, who are a great inspiration to me. Also, I dedicate this work to my advisor Yan Cao, who helped greatly in research process and editing this manuscript.

## ACKNOWLEDGEMENT

I am using this opportunity to express my appreciation and thanks to the people who have given me invaluable support.

First and foremost, I would like to thank my research supervisor, Prof. Yan Cao, who has instructed me for two years. His creative ideas, profound knowledge, flexible thought, have taught me how to be an eligible researcher. His advices on both of my research work and my career will certainly benefit me in my future life. I really appreciate all his mentorship.

I also appreciate Prof. Bangbo Yan and Prof. Jeremy Maddox for their willingness to serve as my thesis committee members and their insightful suggestions. I really thank all their time and guidance for the thesis and defense. Also, I would like to express my thankfulness to Prof. Burris and Prof. Conte. I really appreciate their encouragements and supports in my research and my life in WKU. Moreover, I would like to appreciate Dr. John Andersland for his training and instruction in electron microscope, thank Prof. Rui Zhang for his help in my Ph.D. application and suggestions for my research work.

At last, I would like to express my feeling of gratitude my partners Junjie Xiang, Ying Chen, Haihong Zhao, Chuanchuan Cai, Yue Zhang, Xinju Dong, Zifeng Sui who have kept company with me during my two years in WKU.

I would also like to thank everyone who has ever helped me!

## PREFACE

This dissertation is submitted for my Master's degree at Western Kentucky University. The research described in here was instructed by Prof. Yan Cao in the Department of Chemistry, Western Kentucky University, from January 2016 to December 2017 to the best of my knowledge. Except for the acknowledgements and references, this work is original. Neither this, nor any substantially similar dissertation has been or is submitted for any other degree, diploma.

The environmental issues caused by consumption of fossil fuels has drawn my attention since I was in my undergraduate period. These problems lead an urgent need to develop clean, efficient and renewable energy sources to maintain a sustainable economic development. This is my motivation of pursuing Master degree. By chance, introduced through Dr. Yan Cao, I decided to continue my advanced study in the Chemistry Department of Western Kentucky University after completing my undergraduate study in China.

As an international student, I faced a lot of challenges, such as cultural differences, communication barriers and research environment. However, I do appreciate these challenges today, as they pushed me out of my previous thoughts and behavior. My experience in WKU teaches me how to be a creative, perseverant, competent and accomplished student. As a graduate student and research assistant, I have developed a series of advanced nano/micro-structured materials, applied in electrochemical redox reactions and photocatalysis. During my stay in WKU, I have successfully published 7

peer-reviewed articles. Among of them, 4 as the first author (one of them was a featured article).

I have a great deal of enthusiasm and motivation about research, and enjoy the process of discovery. I really hope my work would be valuable and useful in the future.

# CONTENTS

|  |    |
|--|----|
| I. INSTRUCTION .....   | 1  |
| 1.1 Background .....   | 1  |
| 1.2 The application of iron cobalt oxides for energy storage and conversion. ....  | 4  |
| 1.2.1.....Application for supercapacitor   | 4  |
| 1.2.2.....Application for lithium-ion batteries  | 5  |
| 1.2.3..... Application for fuel cells  | 9  |
| 1.3 General research goals .....   | 11 |
| II. EXPERIMENTAL .....   | 13 |
| 2.1 Chemicals .....  | 13 |
| 2.2 Synthesis of electrode materials .....   | 13 |
| 2.3 Assembly of asymmetric supercapacitors .....   | 17 |
| 2.4 Characterization .....   | 17 |
| 2.5 Electrochemical measurement.....   | 18 |
| III. RESULTS AND DISCUSSION.....   | 20 |
| 3.1 Hierarchically porous $\text{CoFe}_2\text{O}_4$ nanosheets supported on Ni foam with excellent<br>electrochemical properties for asymmetric supercapacitor ..... | 20 |
| 3.1.1 Material characterization.....   | 20 |



|   |    |
|---|----|
| 3.1.2 Electrochemical properties of $\text{CoFe}_2\text{O}_4$ electrode .....   | 25 |
| 3.1.3 Electrochemical performance of $\text{CoFe}_2\text{O}_4//\text{AC}$ asymmetric supercapacitor   | 29 |
| 3.2 $\text{FeCo}_2\text{O}_4$ submicron prisms grown on Ni foam as high-performance positive<br>electrode for supercapacitor .....  | 34 |
| 3.2.1 Material Characterization .....   | 34 |
| 3.2.2 Electrochemical properties of $\text{FeCo}_2\text{O}_4$ electrode .....   | 40 |
| 3.3 Hierarchical core-shell nanosheet arrays with $\text{MnO}_2$ grown on mesoporous<br>$\text{CoFe}_2\text{O}_4$ support for high-performance asymmetric supercapacitors .....   | 47 |
| 3.3.1 Material Characterization .....   | 47 |
| 3.3.2 Electrochemical properties of $\text{CoFe}_2\text{O}_4@\text{MnO}_2$ electrode.....   | 55 |
| 3.3.3 Electrochemical performance of $\text{CoFe}_2\text{O}_4@\text{MnO}_2//\text{AC}$ asymmetric<br>supercapacitor .....   | 62 |
| 3.4 Controlled synthesis of $\text{MnO}_2$ nanosheets vertically covered $\text{FeCo}_2\text{O}_4$ nanosheets as<br>binder-free electrode durable asymmetric supercapacitor ..... | 68 |
| 3.4.1 Material Characterization .....   | 68 |
| 3.4.2 Electrochemical properties of $\text{FeCo}_2\text{O}_4@\text{MnO}_2$ electrode.....   | 75 |
| 3.4.3 Electrochemical performance of $\text{FeCo}_2\text{O}_4@\text{MnO}_2//\text{AC}$ asymmetric<br>supercapacitor .....   | 81 |

IV. CONCLUSION .....86

V. LITERATURE CITED .....89

VI. ACHIEVEMENT .....102

## LIST OF FIGURES

|  |    |
|--|----|
| Figure 1. Simplified Ragone plot of the energy storage domains for the various electrochemical energy storage and conversion systems compared to an internal combustion engine and turbines and conventional capacitors.....   | 2  |
| Figure 2. Schematic diagram of the charging-discharging process in a Li-ion battery .....  | 7  |
| Figure 3. (a) XRD patterns and (b) Raman spectra of $\text{CoFe}_2\text{O}_4$ nanosheets on Ni foam; (c) $\text{N}_2$ adsorption-desorption isotherms and inset shows the pore size distribution of $\text{CoFe}_2\text{O}_4$ nanosheets. ....   | 21 |
| Figure 4. (a-d) SEM images of typical $\text{CoFe}_2\text{O}_4$ nanosheets on Ni foam, (e) EDX analysis of $\text{CoFe}_2\text{O}_4$ nanosheets and (f-h) TEM images of $\text{CoFe}_2\text{O}_4$ nanosheets scratched from Ni foam. ....  | 23 |
| Figure 5. XPS spectra of the (a) survey, (b) O 1s (c) Co 2p, and (d) Fe 2p regions of $\text{CoFe}_2\text{O}_4$ nanosheets on Ni foam. ....  | 24 |
| Figure 6. (a) CV curves of $\text{CoFe}_2\text{O}_4$ nanosheets at different scan rates. (b) Galvanostatic charge-discharge of the $\text{CoFe}_2\text{O}_4$ nanosheets at various current densities. (c-e) Comparing bare $\text{CoFe}_2\text{O}_4$ electrode (black), $\text{Co}_3\text{O}_4$ electrode (red) and $\text{Fe}_3\text{O}_4$ electrode (blue), all grown on Ni foam: (c) CV curves at $10 \text{ mV s}^{-1}$ , (d) galvanostatic charge-discharge at $2 \text{ A g}^{-1}$ , (e) specific capacitances versus discharge current density. |    |

Galvanostatic charge-discharge of the (f)  $\text{Co}_3\text{O}_4$  and (g)  $\text{Fe}_3\text{O}_4$  at various current densities. (h) EIS curves (inset shows the EIS curves at high frequency).....27

Figure 7. (a) Comparative CV curves of the activated carbon electrode and  $\text{CoFe}_2\text{O}_4$  electrode at  $20 \text{ mV s}^{-1}$ . (b) CV curves at different cell voltages at a scan rate of  $20 \text{ mV s}^{-1}$  and (c) different scan rates for  $\text{CoFe}_2\text{O}_4 // \text{AC-ASC}$  device. (d) Galvanostatic charge-discharge curves at different current densities. (e) Specific capacitances of the  $\text{CoFe}_2\text{O}_4 // \text{AC-ASC}$  device at different current densities. (f) Cycling stability of  $\text{CoFe}_2\text{O}_4 // \text{AC-ASC}$  device at a current density of  $4.8 \text{ A g}^{-1}$ . (g) First and (h) last 10 charge-discharge curves of  $\text{CoFe}_2\text{O}_4//\text{AC ASC}$  at  $4.8 \text{ A g}^{-1}$  in the potential range between 0-1.5 V. (i) EIS curves of the fresh  $\text{CoFe}_2\text{O}_4 @ \text{MnO}_2$  electrode and after 5000th cycles. ....31

Figure 8. (a) Ragone plot of the  $\text{CoFe}_2\text{O}_4 // \text{AC-ASC}$  device. The values reported for others devices are given here for a comparison. (b) A digital image showing the two ASC devices in series can light up one red LED indicator. (c) Images of the red LED at different stages; powered by the 10 s charged series supercapacitors (d) CV curves at different scan rates and (e) Galvanostatic charge-discharge curves at different current densities for  $\text{CoFe}_2\text{O}_4 // \text{CoFe}_2\text{O}_4 \text{ SSC}$  device. (f) Ragone plot of the  $\text{CoFe}_2\text{O}_4//\text{AC ASC}$  and  $\text{CoFe}_2\text{O}_4//\text{CoFe}_2\text{O}_4 \text{ SSC}$  devices. ....33

|   |    |
|---|----|
| Figure 9. (a) Schematic illustration of the fabrication of $\text{MCo}_2\text{O}_4$ SMPs on NF; (b) XRD patterns of $\text{MCo}_2\text{O}_4$ (M= Co and Fe) SMPs on NFs. TGA curves of (c) $\text{Co}_3\text{O}_4$ and (d) $\text{FeCo}_2\text{O}_4$ .....  | 35 |
| Figure 10. SEM and element mapping images of $\text{MCo}_2\text{O}_4$ SMPs on NF: (a), (c) and (e) for $\text{Co}_3\text{O}_4$ , (b), (d) and (f) for $\text{FeCo}_2\text{O}_4$ . EDX analysis of (g) $\text{Co}_3\text{O}_4$ and (h) $\text{FeCo}_2\text{O}_4$ . .....   | 36 |
| Figure 11. TEM and HRTEM images of $\text{MCo}_2\text{O}_4$ SMPs scratched from NFs. (a-c) for $\text{Co}_3\text{O}_4$ , (d-f) for $\text{FeCo}_2\text{O}_4$ . (Insets of b, e are the SAED patterns of $\text{MCo}_2\text{O}_4$ SMPs)  | 38 |
| Figure 12. (a-c) XPS spectra of the $\text{Co}_3\text{O}_4$ (a) survey, (b) Co 2p, (c) O 1s and (d-g) $\text{FeCo}_2\text{O}_4$ , (d) survey, (e) Fe 2p, (f) Co 2p, (g) O 1s. ....  | 39 |
| Figure 13. (a) CV curves of $\text{MCo}_2\text{O}_4$ (M= Co, Fe) SMPs at a scan rate of $5 \text{ mV s}^{-1}$ ; (b) GCD curves of $\text{MCo}_2\text{O}_4$ (M= Co, Fe) SMPs at a current density of $10 \text{ mA cm}^{-2}$ ; Discharge curves of (c) $\text{Co}_3\text{O}_4$ , (d) $\text{FeCo}_2\text{O}_4$ SMPs at different current densities. (e) areal capacitance and (f) specific capacitance of $\text{MCo}_2\text{O}_4$ (M= Co, Fe) SMPs at different current densities. .... | 42 |
| Figure 14. CV curves of (a) $\text{Co}_3\text{O}_4$ , (b) $\text{FeCo}_2\text{O}_4$ SMPs at different scan rates. (c) Relationship between the anodic peak current densities and square root of scan rates for the $\text{MCo}_2\text{O}_4$ (M= Co, Fe) SMPs electrodes; (b) EIS curves (inset shows the EIS curves at the high frequency) and (c) cycling stability of $\text{MCo}_2\text{O}_4$ (M= Co, Fe) SMPs electrodes. ....  | 44 |

Figure 15. (a and c) First ten GCD curves and (b and d) last ten GCD curves for  $MCo_2O_4$  (M= Co, Fe). SEM images of (e-f) for  $Co_3O_4$ , (g-h) for  $FeCo_2O_4$ , after 5000 cycling tests in three-electrode system. ....46

Figure 16. (a) XRD patterns of  $CoFe_2O_4$  nanosheets on Ni foam before (black curve) and after  $MnO_2$  covering (red curve). (b)  $N_2$  adsorption-desorption isotherms and (c) pore-size distribution of  $CoFe_2O_4$  and  $CoFe_2O_4@MnO_2$  core-shell NSAs. ....47

Figure 17. (a-b) SEM images of typical  $CoFe_2O_4$  nanosheets on Ni foam. (c-d) SEM images of typical  $CoFe_2O_4 @ MnO_2$  core-shell NSAs on Ni foam. (e) SEM image and the corresponding element (Mn, Fe and Co) mapping of the  $CoFe_2O_4 @ MnO_2$  core-shell NSAs. (f) EDX data of  $CoFe_2O_4 @ MnO_2$  core-shell nanosheet arrays obtained from element mapping. ....50

Figure 18. TEM images of (a-c)  $CoFe_2O_4$  nanosheets and (c-f)  $CoFe_2O_4 @ MnO_2$  NSAs scratched from Ni foam. The insets in Figure b and e are the corresponding SAED patterns of  $CoFe_2O_4$  nanosheets and  $CoFe_2O_4@MnO_2$  NSAs, respectively. (g) STEM-EDX mapping of an individual  $CoFe_2O_4 @ MnO_2$  core-shell NSA. ....52

Figure 19. XPS spectra of the (a) Co 2p and (b) Fe 2p regions of  $CoFe_2O_4$  nanosheets. XPS spectra of the (c) Mn 2p and (d) O 1s of  $CoFe_2O_4 @ MnO_2$  core-shell NSAs. 54

Figure 20. SEM images of the  $CoFe_2O_4 @ MnO_2$  core-shell NSAs obtained at different reaction times: (a) 0h; (b) 5h; (c) 10h; (d) 15h; and (e) 20h. Insets show the high-magnification SEM images. (f) Areal capacitances of  $CoFe_2O_4 @ MnO_2$  core-shell

NSAs electrodes obtained at different reaction times and at different current densities.

.....55

Figure 21. (a) CV curves of  $\text{CoFe}_2\text{O}_4 @ \text{MnO}_2$  core-shell arrays fabricated with different reaction times at a scan rate of  $10 \text{ mV s}^{-1}$ . (b-d) Galvanostatic charge-discharge of the  $\text{CoFe}_2\text{O}_4 @ \text{MnO}_2$  core-shell arrays fabricated with different reaction times at various current densities. (b) 5h; (c) 10h; (d) 20h.....57

Figure 22. (a) CV curves of  $\text{CoFe}_2\text{O}_4 @ \text{MnO}_2$  core-shell NSAs at different scan rates. (b) Galvanostatic charge-discharge of the  $\text{CoFe}_2\text{O}_4 @ \text{MnO}_2$  core-shell NSAs at various current densities. (c-f) Comparing bare  $\text{CoFe}_2\text{O}_4$  electrode (black), bare  $\text{MnO}_2$  electrode (red) and optimal  $\text{CoFe}_2\text{O}_4 @ \text{MnO}_2$  electrode (blue), all grown on Ni foam: (c) CV curves at  $20 \text{ mV s}^{-1}$ , (d) galvanostatic charge-discharge at  $5 \text{ mA cm}^{-2}$ , (e) areal specific capacitances versus discharge current density, and (f) EIS curves (inset shows the EIS curves at high frequency).....61

Figure 23. (a) Schematic illustration of the as-fabricated  $\text{CoFe}_2\text{O}_4 @ \text{MnO}_2//\text{AC-ASC}$  device. (b) Comparative CV curves of the activated carbon electrode and  $\text{CoFe}_2\text{O}_4 @ \text{MnO}_2$  electrode at  $10 \text{ mV s}^{-1}$ . (c) CV curves at different cell voltages at a scan rate of  $20 \text{ mV s}^{-1}$  and (d) different scan rates for  $\text{CoFe}_2\text{O}_4 @ \text{MnO}_2// \text{AC-ASC}$  device. (e) Galvanostatic charge-discharge curves at different current densities. (f) Specific capacitances of the  $\text{CoFe}_2\text{O}_4 @ \text{MnO}_2// \text{AC-ASC}$  device at different current densities.

.....62

Figure 24. (a) Ragone plot of the  $\text{CoFe}_2\text{O}_4 @ \text{MnO}_2//\text{AC-ASC}$  device. The values reported for others devices and some commercial supercapacitors are given here for a comparison. (b) A digital image showing the two ASC devices in series can light up ten red LED indicators. (c) A rotating motor derived by two supercapacitors in series. (d) Cycling stability of  $\text{CoFe}_2\text{O}_4 @ \text{MnO}_2//\text{AC-ASC}$  device at a current density of  $41 \text{ mA cm}^{-2}$ . (e) EIS curves of the fresh  $\text{CoFe}_2\text{O}_4 @ \text{MnO}_2$  electrode and after 2250th cycle. (f-g) SEM images of  $\text{CoFe}_2\text{O}_4 @ \text{MnO}_2$  NSAs after cycling test. ....64

Figure 25. (a) XRD patterns of  $\text{FeCo}_2\text{O}_4$  nanosheets on the Ni foam before (black curve) and after the growth of  $\text{MnO}_2$  (red curve). (b) The nitrogen adsorption-desorption isotherms and (c) the corresponding BJH pore-size distribution of  $\text{FeCo}_2\text{O}_4$  and  $\text{FeCo}_2\text{O}_4@\text{MnO}_2$  NSAs. ....68

Figure 26. (a-b) SEM images of typical  $\text{FeCo}_2\text{O}_4$  nanosheets on Ni foam. (d-e) SEM images of typical  $\text{FeCo}_2\text{O}_4@\text{MnO}_2$  NSAs on Ni foam. EDX analysis of (c)  $\text{FeCo}_2\text{O}_4$  nanosheets on the Ni foam and (f)  $\text{FeCo}_2\text{O}_4@\text{MnO}_2$  NSA on the Ni foam. ....70

Figure 27. TEM images of (a-c)  $\text{FeCo}_2\text{O}_4$  nanosheets and (d-f)  $\text{FeCo}_2\text{O}_4@\text{MnO}_2$  NSAs scratched from Ni foam. The insets of Figure b and e are the corresponding SAED pattern of  $\text{FeCo}_2\text{O}_4$  nanosheets and  $\text{FeCo}_2\text{O}_4@\text{MnO}_2$  NSAs, respectively. ....72

Figure 28. XPS spectra of the (a) Co 2p and (b) Fe 2p regions of  $\text{FeCo}_2\text{O}_4$  nanosheets. XPS spectra of the (c) Mn 2p and (d) O 1s of  $\text{FeCo}_2\text{O}_4@\text{MnO}_2$  NSAs. ....74



Figure 29. SEM images of the FeCo<sub>2</sub>O<sub>4</sub>@MnO<sub>2</sub> NSAs obtained at different reaction times: (a) 0h; (b) 5h; (c) 10h; (d) 15h; and (e) 20h. Insets show the high-magnification SEM images. (f) Areal capacitances of FeCo<sub>2</sub>O<sub>4</sub>@MnO<sub>2</sub> NSAs electrodes obtained at different reaction times and at different current densities. ....75

Figure 30. (a) CV curves of FeCo<sub>2</sub>O<sub>4</sub>@MnO<sub>2</sub> NSAs fabricated with different reaction times at a scan rate of 20 mV s<sup>-1</sup>. (b-d) Galvanostatic charge-discharge of the FeCo<sub>2</sub>O<sub>4</sub>@MnO<sub>2</sub> NSAs fabricated with different reaction times at various current densities. (b) 5h; (c) 10h; (d) 20h. (e) Low- and (f) high-magnification SEM images of MnO<sub>2</sub> nanosheets on the Ni foam prepared by the same hydrothermal synthesis (without pre-grown FeCo<sub>2</sub>O<sub>4</sub> nanosheets).....77

Figure 31. (a) CV curves of FeCo<sub>2</sub>O<sub>4</sub>@MnO<sub>2</sub> NSAs at different scan rates. (b) Galvanostatic charge-discharge of the FeCo<sub>2</sub>O<sub>4</sub>@MnO<sub>2</sub> NSAs at various current densities. (c-f) Comparing bare FeCo<sub>2</sub>O<sub>4</sub> electrode (black), bare MnO<sub>2</sub> electrode (red) and optimal FeCo<sub>2</sub>O<sub>4</sub>@MnO<sub>2</sub> NSAs electrode (blue), all grown on Ni foam: (c) CV curves at 20 mV s<sup>-1</sup>, (d) galvanostatic charge-discharge at 5 mA cm<sup>-2</sup>, (e) areal specific capacitances versus discharge current density, and (h) EIS curves (inset shows the EIS curves at high frequency, the equivalent circuit model is shown on the top right). Galvanostatic charge-discharge of the (f) FeCo<sub>2</sub>O<sub>4</sub> nanosheets and (g) MnO<sub>2</sub> nanosheets on nickel foam at various current densities.....80

Figure 32. (a) Comparative CV curves of the activated carbon electrode and FeCo<sub>2</sub>O<sub>4</sub>@MnO<sub>2</sub> NSAs electrode at 10 mV s<sup>-1</sup>. (b) CV curves at different cell voltages at a scan rate of 20 mV s<sup>-1</sup> and (c) different scan rates for FeCo<sub>2</sub>O<sub>4</sub>@MnO<sub>2</sub>//AC ASC device. (d) Galvanostatic charge-discharge curves at different current densities. (e) Specific capacitances of the FeCo<sub>2</sub>O<sub>4</sub>@MnO<sub>2</sub>//AC ASC device at different current densities. (f) Self-discharge curve of the FeCo<sub>2</sub>O<sub>4</sub>@MnO<sub>2</sub>//AC ASC device. ....83

Figure 33. (a) Ragone plot of the FeCo<sub>2</sub>O<sub>4</sub>@MnO<sub>2</sub>//AC ASC device. Inset shows a digital image of two ASC devices in series which can light up ten green LED indicators. (b) Cycling stability of FeCo<sub>2</sub>O<sub>4</sub>@MnO<sub>2</sub>//AC ASC device at a current density of 40 mA cm<sup>-2</sup>. (c) First and (d) last 10 charge-discharge curves of FeCo<sub>2</sub>O<sub>4</sub>@MnO<sub>2</sub>//AC-ASC device at 40 mA cm<sup>-2</sup> current density in the potential range between 0-1.65 V for 5000 cycles. (e) Images of the green LEDs at different stages. ....85

# NANO/SUBMICRO-STRUCTURED IRON COBALT OXIDES BASED MATERIALS FOR ENERGY STORAGE APPLICATION

Hongyan Gao

December 2017

104 Pages

Directed by: Dr. Yan Cao, Dr. Bangbo Yan, Dr. Jeremy Maddox

Department of Chemistry

Western Kentucky University

Supercapacitors, as promising energy storage devices, have been of interest for their long lifespan compared to secondary batteries, high capacitance and excellent reliability compared to conventional dielectric capacitors. Transition metal oxides can be applied as the electrode materials for pseudocapacitors and offer a much higher specific capacitance.  $\text{Co}_3\text{O}_4$  is one of the most investigated transition metal oxides for supercapacitor. Besides simple monometallic oxides, bimetallic transition oxides have recently drawn growing attention in electrochemical energy storage. They present many unique properties such as achievable oxidation states, high electrical conductivities because of the coexistence of two different cations in a single crystal structure.

This study focuses on the bimetallic iron cobalt oxide based materials for the application of energy storage. We selected iron as the substituent in spinel  $\text{Co}_3\text{O}_4$ , by virtue of its abundant and harmless character. Four types of iron cobalt oxides based electrode materials with different morphologies and components have been synthesized for the first time. The hydrothermal method was the main strategy for the synthesis of iron cobalt based materials, which achieved the control of morphology and ratio of components. Multiple characterization methods, including SEM, TEM, XRD, XPS, TGA, BET, have been

applied to study the morphologies and nano/submicron structures. The electrochemical properties of as-fabricated samples were performed by electrochemical workstation. In addition, in order to investigate the practical application of electrode materials, asymmetric supercapacitors have been assembled by using as-prepared samples as the positive electrodes and activated carbon as the negative electrodes.

# I. INSTRUCTION

## 1.1 Background

With the rapid consumption of fossil fuels and severe environmental issues, there is an urgent need to develop high-efficiency energy conversion and storage devices, such as fuel cells, supercapacitors and Lithium-ion batteries.<sup>1-3</sup> Despite that the energy storage and conversion mechanisms are different among these three devices, they still share some electrochemical similarities. All the energy storage and conversion processes occur at the interface of electrode and electrolyte and the electron and ion transport are separated.<sup>4</sup> A simplified Ragone plot (Figure. 1) demonstrates the domains of these three energy storage and conversion systems compared with traditional systems including combustion engine, turbines and capacitors. Among these three energy providing systems, fuel cells belong to high-energy systems as the anode and cathode are used to transfer charge and the fuels will undergo the redox reactions without involving the process of combustion, whereas supercapacitors belong to high-power system since supercapacitors stores electrical charges both at the electrode surface and in the bulk near the surface of the solid electrode. Lithium-ion batteries have intermediate power and energy characteristics. Note that electrode materials are the most important components for energy storage and conversion systems and carbon materials, conducting polymers and transition metal oxides have become three of the most popular electrode materials. It is mentionable that some of these three energy storage and conversion systems all depend on the redox reactions of electrodes,

so some materials such as transition metal oxides can be applied as the electrode materials for all these energy providing devices.

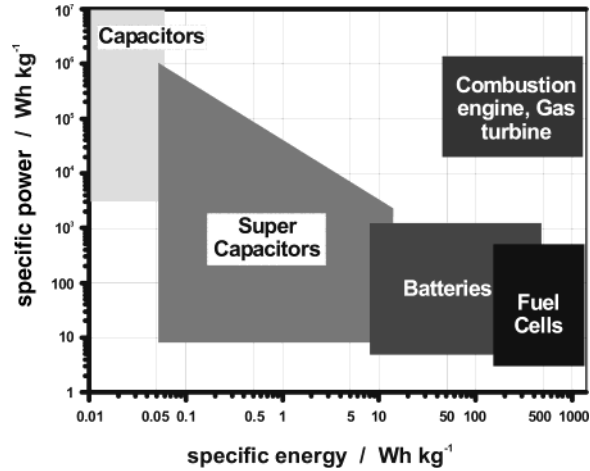


**Figure 1.** Simplified Ragone plot of the energy storage domains for the various electrochemical energy storage and conversion systems compared to an internal combustion engine and turbines and conventional capacitors.<sup>4</sup>

Among all the electrode materials, transition metal oxides possess several oxidation states which are favorable for a rapid redox reaction, leading to efficient and high-quality energy storage and conversion systems. However, some of the single metal oxides suffer from low conductive property and stability which constrain the performance of energy storage and conversion systems such as NiO,<sup>5-6</sup> Co<sub>3</sub>O<sub>4</sub>,<sup>7-9</sup> and MnO<sub>2</sub>.<sup>10</sup> Nanostructures and composite engineering of materials are approaches to conquer these issues.<sup>11</sup> Recently, binary metal oxides have aroused much attention in energy storage and conversion applications by virtue of their better conductivity and electrochemical performance than single component oxides. Among all these binary metal oxides, spinel cobaltites, M<sub>x</sub>Co<sub>3-x</sub>O<sub>4</sub> (M = Ni, Mn, Zn, Cu and so on), have exhibited better characteristics in fuel cells, Li-

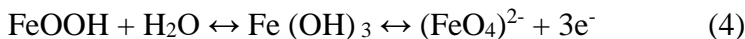
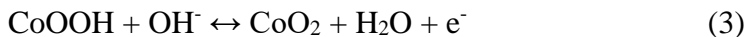
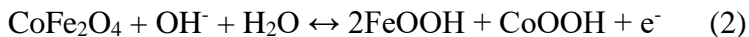
ion batteries and supercapacitors.<sup>12-14</sup> Not only can the conductivity and electrochemical activity be increased, but the toxicity and cost can be reduced through substituting the Co-content with other metals. Among these substitutable metals, iron has attracted great interest due to its abundance, harmless character and excellent performance.  $\text{FeCo}_2\text{O}_4$  and  $\text{CoFe}_2\text{O}_4$  are two kinds of binary metal oxides which have been widely investigated as promising electrode materials for supercapacitors, fuel cells and Li-ion batteries.

Actually,  $\text{FeCo}_2\text{O}_4$  and  $\text{CoFe}_2\text{O}_4$  based electrodes store charges and convert energy mainly on the surface and in the bulk near the surface of the electrode. High specific surface area is one of the most important factors need to be considered. Compared with bulk materials, nanostructured materials possess much higher specific surface which can provide short transport and diffusion path lengths for ions and electrons as well as more electroactive sites for energy storage and conversion. On the other hand, the fabrication of iron cobalt oxide based composite materials also is another strategy to enhance the performance of supercapacitors, Li-ion batteries and fuel cells. They can display the advantages of all constituents and overcome the drawbacks of individual materials such as low conductivity, mechanical degradation and nanostructured agglomeration.

## 1.2 The application of iron cobalt oxides for energy storage and conversion.

### 1.2.1 Application for Supercapacitor

According to the energy storage mechanism, supercapacitors can be further divided into two categories: one is electrochemical double-layer capacitor (EDLC) which store energy by accumulating charge in the electrode/electrolyte interface, and the other is the pseudo-capacitors based on the fast and reversible redox reactions at electrochemically active sites.<sup>15-16</sup> Just like other spinel cobaltites and ferrites materials,  $\text{FeCo}_2\text{O}_4$  and  $\text{CoFe}_2\text{O}_4$  based materials can be used as the electrodes for pseudo-capacitors. They store charges both on the surface and in the bulk near the surface of the solid electrode where the Faradic reactions occur.<sup>17</sup> As previous reports show, the energy storage mechanisms for pseudo-capacitors of  $\text{FeCo}_2\text{O}_4$  and  $\text{CoFe}_2\text{O}_4$  in alkaline solution can be described by the following equations:<sup>18</sup>



There are several kinds of morphologies reported in previous literature, including nanoparticles, nanowires, nanosheets and nanoshelled-microspheres. Recently, nanostructured  $\text{FeCo}_2\text{O}_4$  and  $\text{CoFe}_2\text{O}_4$  electrode materials have been grown on conductive

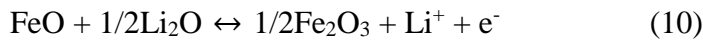
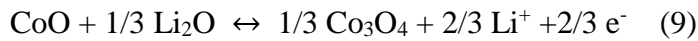
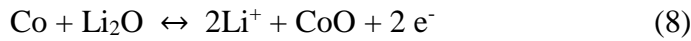
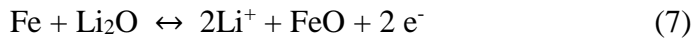
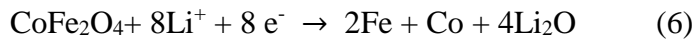
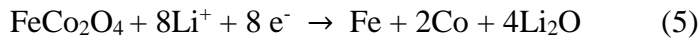


substrates such as nickel foam and stainless steel directly. Direct contact of  $\text{FeCo}_2\text{O}_4$  and  $\text{CoFe}_2\text{O}_4$  on highly conductive substrate avoid the use of binder and additives, resulting to almost all available surface can be exposed and participate in energy storage and conversion process. Pendasheh. et. al. fabricated nanostructured porous wires of  $\text{FeCo}_2\text{O}_4$  supported on nickel foam which exhibited  $407 \text{ F g}^{-1}$  at a scan rate of  $10 \text{ mV s}^{-1}$ . Interestingly, after cycling for 2000 cycles, the electro-activation of the material or pore opening lead to a subsequent increase in capacitance up to  $610 \text{ F g}^{-1}$ , which are significant characteristics of this material for supercapacitor.<sup>18</sup> In addition, several other materials which also own the electrochemical capacitance properties such as carbon materials, metal oxides and conducting polymers have been combined with iron cobalt oxides to fabricate composite material electrodes. As expected, these composited materials displayed an enhanced performance and showed synergistic effects in supercapacitor applications. Zhu. et al. reported  $\text{MnO}_2$ -nanosheet covered submicronmeter- $\text{FeCo}_2\text{O}_4$ -tube forest for high energy density supercapacitors. After the deposition of  $\text{MnO}_2$  nanosheets, the specific capacitance reached  $3.3 \text{ F cm}^{-2}$  at  $1 \text{ mA cm}^{-2}$ , which was one time higher than that of bare  $\text{FeCo}_2\text{O}_4$ -tube electrode about  $1.8 \text{ F cm}^{-2}$  at  $1 \text{ mA cm}^{-2}$ .<sup>19</sup>

### **1.2.2 Application for Lithium-ion batteries**

Compared with supercapacitors, Lithium-ion batteries possess high energy storage and high cell voltage but have a lower power output. Also, the energy densities and power densities of Lithium-ion batteries are twice and five times greater than those of current Pb-

acid and Ni-Cd batteries.<sup>20</sup> However, the application of Lithium-ion batteries is hampered by the electrode material. Conventional electrode materials such as graphite only possesses a theoretical specific capacity about 372 mA h g<sup>-1</sup>.<sup>21</sup> In recent years, transition metal oxides have been intensively explored as promising anode materials because of their high theoretical specific capacitance. Generally, both of FeCo<sub>2</sub>O<sub>4</sub> and CoFe<sub>2</sub>O<sub>4</sub> own excellent electrochemical performance for Lithium-ion batteries and CoFe<sub>2</sub>O<sub>4</sub> possesses a high theoretical specific capacity of 914 mA h g<sup>-1</sup> which is two times higher than that of graphite.<sup>22</sup> What's more, iron is the most abundant material on the earth as well as eco-friendly. Consequently, iron cobalt oxides have been widely investigated as anode materials for Lithium-ion batteries. According to previous literature, the electrochemical mechanism of FeCo<sub>2</sub>O<sub>4</sub> and CoFe<sub>2</sub>O<sub>4</sub> storing Li ions obey to the displacive redox reaction, demonstrated by the following equations.



Similar to supercapacitors, the binary metal oxide electrode stores Li ion mainly on the interface of the electrode/electrolyte and in the bulk near the surface of the solid electrode.

Figure 2 shows a schematic diagram of the charging-discharging process in a Li-ion

batteries. During the charging-discharging process, the electrode involves a reversible insertion and extraction of Li ions as described by above equations. The charging process is accompanied with Li ions extracted from cathode and inserted into anode. During discharging process, Li ions are deintercalated from the anode and intercalated into cathode. The energy storage is realized by the intercalation and deintercalation of Li ions between the anode and cathode. However, there exists an irreversible capacity loss after the first cycle due to the incomplete conversion reaction and the solid electrolyte interface (SEI) layer formation at the electrode/electrolyte interface caused by the reduction of electrolyte.<sup>23</sup> In addition, the large volume change, the severe aggregation and the low conductivity will take place during the Li ion insertion/extraction process, leading to capacity fade and poor cycling stability.<sup>24-25</sup>

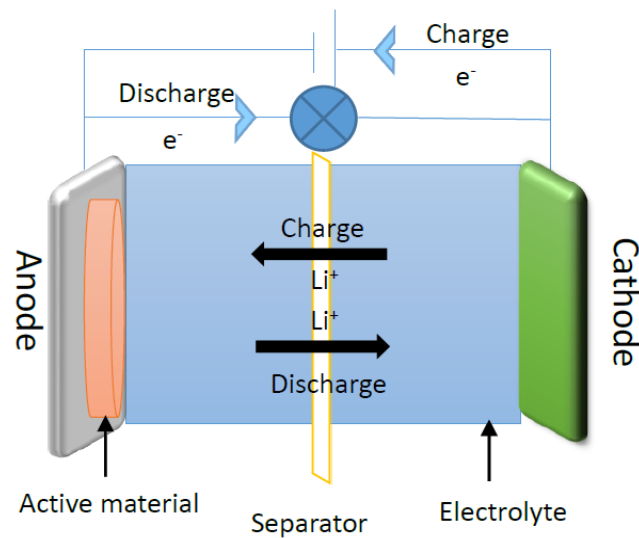


**Figure 2.** Schematic diagram of the charging-discharging process in a Li-ion battery

A lot of efforts have been devoted to remedy the above-mentioned disadvantages of  $\text{FeCo}_2\text{O}_4$  and  $\text{CoFe}_2\text{O}_4$ . For pure  $\text{FeCo}_2\text{O}_4$  and  $\text{CoFe}_2\text{O}_4$  materials, various structures have been fabricated, which show different performance. Since P. Lavela et al.<sup>26</sup> synthesized  $\text{CoFe}_2\text{O}_4$  by the sol-gel process and Y. Sharma et al.<sup>27</sup> fabricated  $\text{FeCo}_2\text{O}_4$  by the urea combustion method, then they confirmed that the Lithium-ion battery performance of  $\text{CoFe}_2\text{O}_4$  and  $\text{FeCo}_2\text{O}_4$  are better than  $\text{NiFe}_2\text{O}_4$  and  $\text{MgCo}_2\text{O}_4$ , respectively. A large number of  $\text{CoFe}_2\text{O}_4$  and  $\text{FeCo}_2\text{O}_4$  materials with different morphologies such as 1D nanowires, 2D nanosheets and 3D nanospheres have been synthesized via different methods. In general, the 1D and 3D nanostructures tend to have higher reversible capacities and better rate capability than microstructures and 2D nanostructures. Especially, the hollow-typed morphology have an advantage over solid-typed morphology in energy storage. This excellent performance which is realized by the unique structures in Lithium-ion batteries are ascribed to the following virtues: (1) 1D and 3D nanostructures provide high surface area which is favorable to reduced electron and lithium ions diffusion paths and more active sites for lithium ions insertion/extraction process,<sup>28-29</sup>(2) these structures can afford adequate spaces to relax the large volume changes during constant charge/discharge processes.<sup>30</sup> As a typical example, H. Guo et al. fabricated hollow porous  $\text{CoFe}_2\text{O}_4$  nanocubes via metal-organic frameworks, the BET surface area of the sample is  $102.7 \text{ m}^2 \text{ g}^{-1}$ .<sup>31</sup> The reversible capacity of  $\text{CoFe}_2\text{O}_4$  nanocubes remained stable as high as  $1115 \text{ mA h g}^{-1}$  after 200 cycles at constant current density of 1C. In addition, the capacity still could reach  $815 \text{ mA h g}^{-1}$  even at a high current density of 20 C, indicating the excellent rate

performance of hollow porous  $\text{CoFe}_2\text{O}_4$  nanocubes.

### 1.2.3 Application for fuel cells

As shown in Figure 1, fuel cells are electrochemical energy conversion devices with high energy density. Unlike supercapacitor and Lithium-ion batteries, fuel cells convert chemical energy directly into electricity without involving combustion resulting in a highly efficient utilization of fuels. According to the difference of electrolytes, fuel cells can be divided into five types: Phosphoric Acid Fuel Cell (PAFC), Proton Exchange Membrane Fuel Cell (PEMFC), Alkaline Fuel Cell (AFC), Molten Carbonate Fuel Cell (MCFC) and Solid Oxide Fuel Cell (SOFC).<sup>32</sup> AFCs have aroused more attention for the potential application of non-platinum catalysts to achieve more efficient kinetics of both the oxygen reduction reaction (ORR) and methanol oxidation reaction (MOR) in alkaline system.<sup>33</sup> In alkaline electrolyte, oxygen can be reduced through either a four-electron process ( $\text{O}_2 + 2\text{H}_2\text{O} + 4\text{e}^- \rightarrow 4\text{OH}^-$ ) or two two-electron processes ( $\text{O}_2 + \text{H}_2\text{O} + 2\text{e}^- \rightarrow \text{HO}_2^- + \text{OH}^-$ ;  $\text{HO}_2^- + \text{H}_2\text{O} + 2\text{e}^- \rightarrow 3\text{OH}^-$ ).<sup>34</sup> Noble metal materials such as Pt,<sup>35</sup> Pd<sup>36</sup> and Ru<sup>37</sup> and Pt-based alloys<sup>38</sup> have been considered as the most efficient catalysts for the ORR reaction in the past decades. However, the high cost of noble metals restrains the commercialization of AFCs. Recently, a new concept was put forward to explore low cost and high activity transitional metal oxide catalysts as a substitute for traditional noble metals in AFC applications.

Remarkably,  $\text{CoFe}_2\text{O}_4$  and  $\text{FeCo}_2\text{O}_4$  showed excellent electrocatalytical activity for the

ORR reaction. R. Z. Yang's group designed and fabricated several cobalt iron oxide nanostructures and nanocomposites. They successfully fabricate solid and hollow  $\text{CoFe}_2\text{O}_4$  nanospheres.<sup>39</sup> Compared with the most efficient Pt/C, the hollow  $\text{CoFe}_2\text{O}_4$  nanospheres showed a negative shift of 180mV at the half-wave potential which is 40 mV positive shift than the solid one, indicating the electrocatalytic activity also depends on the structures and morphologies of materials. In addition, when they combined  $\text{CoFe}_2\text{O}_4$  nanospheres with graphene via a one-pot solvothermal method,<sup>40</sup> the  $\text{CoFe}_2\text{O}_4$  nanospheres/graphene nanocomposite showed a low onset potential about -0.11V (vs. Ag/AgCl) which is higher than -0.17 for  $\text{CoFe}_2\text{O}_4$  nanospheres and excellent stability for ORR reaction which still maintained 94% in ORR current density after 72000s of continuous operation. The enhanced performance of  $\text{CoFe}_2\text{O}_4$  nanospheres/graphene should be attributed to the suppressed agglomeration  $\text{CoFe}_2\text{O}_4$  nanospheres and restacking of graphene as well as synergistic electrocatalytical effects of  $\text{CoFe}_2\text{O}_4$  nanospheres and graphene, in ORR reaction. Among the  $\text{CoFe}_2\text{O}_4$  and  $\text{FeCo}_2\text{O}_4$  based nanocomposites,  $\text{FeCo}_2\text{O}_4$ /hollow graphene spheres exhibited the best performance with an onset potential about -0.09V (vs. Ag/AgCl) which was close to -0.01V of Pt/C.<sup>41</sup> In addition,  $\text{FeCo}_2\text{O}_4$ /hollow graphene spheres exhibited high durability with 92.1% retention in the ORR current density over 86400s while the commercial Pt/C only maintained 41.1%, indicating  $\text{FeCo}_2\text{O}_4$ /hollow graphene spheres could be a substitutable low-cost and efficient material for the ORR process. However, the main problem to fabricate a composite is the proper guest material and the optimal stoichiometric ratio and morphologies. Hence, it is necessary to design and

synthesize novel materials aimed at enhancing the optimal electrocatalytical performance for the ORR reaction.

### **1.3 General research goals**

In order to realize better electrochemical performance, researchers have developed different morphologies, structures, and composites of  $\text{CoFe}_2\text{O}_4$  and  $\text{FeCo}_2\text{O}_4$  based materials and applied them in supercapacitors, Lithium ion batteries and fuel cells. However, the optimal performance of  $\text{CoFe}_2\text{O}_4$  and  $\text{FeCo}_2\text{O}_4$  based materials for energy storage and conversion applications have not yet been achieved, there are still several problems need to be figured out which can be summarized as follows: (1) Although a lot of work has been devoted on fabricating novel morphologies and composites, the essential mechanism and process for energy storage and conversion is still not clear. This will hamper the optimization of  $\text{CoFe}_2\text{O}_4$  and  $\text{FeCo}_2\text{O}_4$  based materials. (2) Current approaches which can be applied to fabricate  $\text{CoFe}_2\text{O}_4$  and  $\text{FeCo}_2\text{O}_4$  based materials are mainly confined among some classical methods such as hydrothermal, solvothermal and sol-gel. These methods may introduce some impurities into electrode materials which will affect the performance to some extent. It is necessary to refine the current methods and develop new strategies to fabricate  $\text{CoFe}_2\text{O}_4$  and  $\text{FeCo}_2\text{O}_4$  based materials. (3) The preparation of large-scale devices is one of the most serious obstacles for commercial applications of  $\text{CoFe}_2\text{O}_4$  and  $\text{FeCo}_2\text{O}_4$  based materials as well as some other transition metal oxides. Some works only focus on improving the performance and neglect the practical application. The

current state cannot satisfy these energy requirements and there is still a long way to go.

In order to obtain the optimal  $\text{CoFe}_2\text{O}_4$  and  $\text{FeCo}_2\text{O}_4$  based materials for energy storage and conversion, my research study has been focused on the novel nano/micro-structured iron cobalt oxides based materials and their characterization, electrochemical properties and practical applications.



## II. EXPERIMENTAL

### 2.1 Chemicals

All the chemicals and solvents in this report were analytical grade and used without further purification. Iron (II) perchlorate hydrate ( $\text{Fe}(\text{ClO}_4)_2 \cdot \text{H}_2\text{O}$ , 99.9%, Alfa Aesar, USA), potassium permanganate ( $\text{KMnO}_4$ , 99.7%, Fisher Chemical, USA), iron nitrate nonahydrate ( $\text{Fe}(\text{NO}_3)_3 \cdot 9\text{H}_2\text{O}$ , 99.8%, ACROS, USA), cobalt nitrate hexahydrate ( $\text{Co}(\text{NO}_3)_2 \cdot 6\text{H}_2\text{O}$ , 99.8%, ACROS, USA), urea ( $\text{CO}(\text{NH}_2)_2$ , 99.8%, ACROS, USA), oxalic acid dihydrate ( $\text{H}_2\text{C}_2\text{O}_4 \cdot 2\text{H}_2\text{O}$ , 98%, Fisher Chemical) ethylene glycol ( $(\text{CH}_2\text{OH})_2$ , 99.87%, ACROS, USA) and nickel foam (>99.99%, 350 g m<sup>-2</sup>, MTI, USA), potassium hydroxide (KOH, > 85%, Fisher Chemical), ethanol (99.5%, 200 proof, ACROS, USA), acetone (99.8%, ACROS, USA), hydrochloride acid (HCl, 36.5 to 38.0% w/w, Fisher Chemical), carbon black (> 99.9%, Alfa Aesar<sup>TM</sup>), poly (tetrafluoro-ethylene) preparation (60 wt% dispersion in H<sub>2</sub>O, ALDRICH).

### 2.2 Synthesis of electrode materials

**Synthesis of  $\text{CoFe}_2\text{O}_4$  nanosheets:** In a typical procedure,  $\text{Co}(\text{NO}_3)_2 \cdot 6\text{H}_2\text{O}$  (1 mmol),  $\text{Fe}(\text{ClO}_4)_2 \cdot \text{H}_2\text{O}$  (2 mmol) and 14 mmol urea were added with vigorous stirring to a mixed solvent, which were 20 ml deionized water and 20 ml ethylene glycol. The Ni foam (2cm×5cm piece) was ultrasonically cleaned using a concentrated HCl for the removal of the nickel oxide layer. The treated Ni foam was finally cleaned with ethanol, acetone and

deionized water in an ultrasound bath (30 min of successive sonication in each). The aforementioned solution, together with the Ni foam, were transferred into a 100 mL Teflon-lined autoclave and heated gradually to 90 °C and maintained at the same temperature for 10 h. After the autoclave was cooled to the ambient condition, the as-synthesized material on Ni substrate was taken from the reaction media, washed, dried, and calcined at 400 °C for 2 h in air (2 °C min<sup>-1</sup> heating rate). The loading mass of CoFe<sub>2</sub>O<sub>4</sub> on the prepared supercapacitor electrode was 0.6 mg cm<sup>-2</sup>.

**Synthesis of FeCo<sub>2</sub>O<sub>4</sub> submicron prisms (SMPs):** For the synthesis of FeCo<sub>2</sub>O<sub>4</sub> SMPs, iron nitrates (1 mmol) and cobalt nitrate (2 mmol) were first dissolved in 25 mL deionized water and stirred for 15 min as the Solution A. Then, oxalic acid dihydrate (6 mmol) was dissolved in 25 mL deionized water and stirred for 15 min as the Solution B. The NF (2 cm×3 cm piece) was carefully cleaned with concentrated HCl solution by ultrasonication for 10 min in order to remove the nickel oxide layer on its surface and then ultrasonically cleaned by acetone, ethanol and deionized water (15 min of successive sonication in each). The as-prepared the Solution A together with the NF were transferred into an 80 mL Teflon-lined autoclave and kept for 1 h. Then the Solution B was slowly injected into the autoclave with gently shaking till homogenous precipitation was formed. Then the hydrothermal process was conducted at 100 °C in a Muffle oven. After 2 h, the Teflon-lined autoclave was cooled down by cool water. The NF coated with the precursor was rinsed with ethanol and ultrasonically cleaned by deionized water for 2 min. The product calcination was carried out at 400 °C for 2 h in air with a heating rate of 2 °C min<sup>-1</sup>. The loading mass of

FeCo<sub>2</sub>O<sub>4</sub> SMPs on Ni foam was 1.53 mg cm<sup>-2</sup>.

**Synthesis of CoFe<sub>2</sub>O<sub>4</sub>@MnO<sub>2</sub> core-shell nanosheet arrays (NSAs):** The formation process of CoFe<sub>2</sub>O<sub>4</sub> NSs was based on a hydrothermal method, followed by a post-annealing treatment. Co(NO<sub>3</sub>)<sub>2</sub>•6H<sub>2</sub>O (1 mmol) and Fe(ClO<sub>4</sub>)<sub>2</sub>•H<sub>2</sub>O (2 mmol) in a total 3 mmol and urea in 14 mmol were added to a mixed solvent of deionized water in 15 ml and ethylene glycol in 15 ml with vigorous stirring to obtain Solution A. Nickel foam (2 cm×4 cm piece) was carefully cleaned with 6M HCl solution in an ultrasound bath for 5 min in order to remove the nickel oxide layer on its surface and then ultrasonically cleaned using ethanol, deionized and acetone (30 min of successive sonication in each). The as-obtained Solution A together with the nickel foam were transferred into a 50 ml Teflon-lined autoclave, which was heated gradually to 120 °C and maintained at the same temperature for 7h. After the autoclave cooled down to room temperature naturally, the nickel foam coated with the precursor was rinsed with deionized water and ethanol. The product calcination was finished at 400 °C for 2h in air with 2.5 °C min<sup>-1</sup> heating rate. To prepare CoFe<sub>2</sub>O<sub>4</sub>@MnO<sub>2</sub> core-shell NSAs, 30 ml of 50 mM KMnO<sub>4</sub> aqueous solution was added to a 50 ml Teflon-lined autoclave containing the nickel foam supported CoFe<sub>2</sub>O<sub>4</sub> NSs. The autoclave was kept at 160 °C for 5h, 10h, 15h and 20 h. Then the product was rinsed with deionized water and absolute ethanol and dried at 60 °C for 6h. The loading mass of CoFe<sub>2</sub>O<sub>4</sub> electrode and CoFe<sub>2</sub>O<sub>4</sub>@MnO<sub>2</sub> NSAs were 0.6 mg cm<sup>-2</sup> and 1.8 mg cm<sup>-2</sup> respectively.

**Synthesis of FeCo<sub>2</sub>O<sub>4</sub>@MnO<sub>2</sub> core-shell nanosheet arrays (NSAs):** FeCo<sub>2</sub>O<sub>4</sub>

nanosheets were synthesized in the following procedure.  $\text{Co}(\text{NO}_3)_2 \cdot 6\text{H}_2\text{O}$  (2 mmol) and  $\text{Fe}(\text{ClO}_4)_2 \cdot \text{H}_2\text{O}$  (1 mmol) and 14 mmol urea were dissolved in a mixed solvent composed of deionized water in 15 mL and ethylene glycol in 15 mL, and vigorously stirred for 10 minutes. The above solution together with a piece of Ni foam (2cm  $\times$  4cm) were transferred to a 50 mL Teflon-lined autoclave and maintained at 95 °C for 8h. After the autoclave cooled down to the room temperature naturally, the nickel foam coated with the precursor was rinsed with deionized water and ethanol. The product calcination was finished at 400 °C for 2h in air with 2.5 °C min<sup>-1</sup> heating rate. For the synthesis of  $\text{FeCo}_2\text{O}_4@ \text{MnO}_2$  NSAs, 30 mL of 50 mM  $\text{KMnO}_4$  aqueous solution and previously-prepared nickel foam supported  $\text{FeCo}_2\text{O}_4$  nanosheets was added to a 50 mL Teflon-lined autoclave. The reaction mixture was kept at 160 °C for 5h, 10h, 15h and 20 h. Then the product was rinsed with deionized water and absolute ethanol and dried at 60 °C for 6h. The loading mass of  $\text{FeCo}_2\text{O}_4$  electrode and  $\text{FeCo}_2\text{O}_4@ \text{MnO}_2$  NSAs were 0.5 mg cm<sup>-2</sup> and 1.7 mg cm<sup>-2</sup> respectively.

**Synthesis of  $\text{MnO}_2$  NSs on Ni foam:** To fabricate bare  $\text{MnO}_2$  NSs on Ni foam, 30 ml of 50 mM  $\text{KMnO}_4$  aqueous solution was added to a 50 ml Teflon-lined autoclave containing the cleaned nickel foam. The reaction autoclave was sealed and maintained at 160 °C for 15h. Then the product was rinsed with deionized water and absolute ethanol and dried at 60 °C for 6h. The loading mass of  $\text{MnO}_2$  nanosheets on Ni foam was about 1.8 mg cm<sup>-2</sup>.

**Synthesis of activated carbon (AC) negative electrode:** The negative electrode was firstly prepared by dispersing 80 wt% AC, 10 wt% carbon black and 10 wt% poly (tetrafluoro-ethylene) (PTFE) in ethanol and then pasted the homogeneous paste onto a 1

$\times 1 \text{ cm}^2$  Ni foam by a spatula. The obtained AC electrode was pressed and then dried at  $80 \text{ }^\circ\text{C}$  for 24h.

### 2.3 Assembly of asymmetric supercapacitors

To assemble ASCs, the fabricated electrodes were used as positive electrode, activated carbon (AC) as their negative electrodes. The membrane (NKK, MPF20AC-100) was used as separator to separate the positive and negative electrodes. The cell was encapsulated by a container to prevent the leak of electrolyte. In order to obtain optimal ASC, the mass of positive and negative electrodes were adjusted according to equation (11)

$$C^+ \times \Delta V^+ \times m^+ = C^- \times \Delta V^- \times m^- \quad (11)$$

Where  $C$  in  $\text{F g}^{-1}$  is the specific capacitance of positive and negative electrode,  $\Delta V$  in  $\text{V}$  is the potential window, and  $m$  in  $\text{g}$  is the mass of active material.

### 2.4 Characterization

The as-prepared samples were characterized by the X-ray diffraction (XRD; ARL™ X'TRA Powder Diffractometer,  $\text{Cu K}\alpha$  radiation,  $\lambda = 1.5406 \text{ \AA}$ ) was characterized in the  $2\theta$  range of  $10 - 80^\circ$  with a scan step of  $0.02$  and a scanning speed of  $0.2 \text{ s/step}$ . The morphology and structure were characterized using a scanning electron microscopy (SEM; Model JSM-6510LV, JEOL Ltd., Tokyo, Japan) equipped with an energy dispersive X-ray spectrometer (EDX), and a transmission electron microscopy (TEM; Model JEM-1400 Plus 2100F, JOEL Ltd., Tokyo, Japan,  $200 \text{ kV}$ ). Raman spectra of samples were collected

using a DXR Raman microscope (Thermo DXR, a 780 nm excitation laser and a confocal microscope). The X-ray photoelectron spectroscopy (XPS) measurements were performed using a multi-functional photoelectron spectrometer (Axis Ultra DLD, Kratos) using Al Ka radiation. Nitrogen adsorption-desorption isotherms of samples were analyzed using a Micromeritics ASAP2020M+C Analyzer at 77.45 K. The weight loss curves were measured in air atmosphere with a heating rate of 10 °C min<sup>-1</sup> from the ambient temperature to 500 °C using thermogravimetric analysis (SDT, TA Instrument).

## 2.5 Electrochemical measurement

The electrochemical experiments were carried out in a three-electrode system in 3M KOH solution as the electrolyte. A platinum foil served as the counter electrode and an Ag/AgCl electrode as the reference electrode. Ni Foam with active materials were used as working electrodes (1 cm<sup>2</sup> immersed area), a platinum foil served as the counter electrode and an Ag/AgCl electrode as the reference electrode. The 3M KOH was applied as the aqueous electrolyte. The cyclic voltammetry (CV) and galvanostatic charge-discharge (GCD) tests were conducted using an electrochemical workstation (CHI 660E, Chenhua, Shanghai). All EIS measurements were carried out on Zennium electrochemical workstation (Zahner, INC. Germany). The impedance spectra were recorded under an AC perturbation signal of 5 mV over the frequency range of 0.01 Hz to 100,000 Hz. Corresponding area capacitances ( $C_a$ ), specific capacitances ( $C_s$ ) are calculated according to the following equations:

$$C_a = I\Delta t / S\Delta V \quad (12)$$

$$C_s = I\Delta t / m\Delta V \quad (13)$$

Where  $I$  (A) is the current during the discharge process.  $\Delta t$  (s) is the discharge time,  $S$  ( $\text{cm}^2$ ) is the area of electrode,  $m$  (g) is the mass of electrode materials and  $\Delta V$  (V) is the potential window.

The electrochemical performance of the asymmetric supercapacitor was based on the capacitance obtained from GCD curves. The energy density and power density of the devices were obtained according to the following equations:

$$E = 0.5 C_s (\Delta V)^2 / 3.6 \quad (14)$$

$$P = 3600 E / \Delta t \quad (15)$$

Where  $E$  is the energy density is in  $\text{W h kg}^{-1}$ ,  $P$  is the power density in  $\text{W kg}^{-1}$ ,  $\Delta V$  (V) is the potential window of device, and  $\Delta t$  (s) is the discharge time.

## III. RESULTS AND DISCUSSION

### 3.1 Hierarchically porous CoFe<sub>2</sub>O<sub>4</sub> nanosheets supported on Ni foam with excellent electrochemical properties for asymmetric supercapacitor

#### 3.1.1 Material characterization

The successful fabrication of CoFe<sub>2</sub>O<sub>4</sub> nanosheets was confirmed by XRD and Raman spectra. As shown in Figure 3a, excluding the peaks marked as “star”, contributed to those of Ni, the remaining peaks at  $2\theta = 30.5, 36.0, 37.8, 57.4, 63.1$  and  $71.4$  can be indexed to the (220), (311), (222), (511), (440) and (620) reflections of spinel CoFe<sub>2</sub>O<sub>4</sub> (JCPDS No:00-022-1068), respectively. The whole diffraction peaks were in good agreement with the previous reports.<sup>42-43</sup> Raman spectroscopy was further performed to investigate the structure and phase composition of the samples. The Raman spectra of CoFe<sub>2</sub>O<sub>4</sub> nanosheets (Figure 3b) shows the inverse spinel structure like Fe<sub>3</sub>O<sub>4</sub> with cubic  $O_h^7(Fd3m)$  symmetry. The characteristic peaks at 186, 313, 478, 567 and 652 cm<sup>-1</sup> corresponded to T<sub>1g</sub>-3, E<sub>g</sub>, T<sub>1g</sub>-2, T<sub>1g</sub>-1 and A<sub>1g</sub>-1 vibration modes of the CoFe<sub>2</sub>O<sub>4</sub>, respectively.<sup>44-45</sup> Both the XRD and Raman spectrums confirmed the successful fabrication of CoFe<sub>2</sub>O<sub>4</sub>. In order to characterize the specific surface area and pore structure of CoFe<sub>2</sub>O<sub>4</sub> nanosheets, nitrogen absorption-desorption isotherms were performed. As shown in Figure 3c, the existence of hysteresis loops at the relative pressure of 0.5-1.0 P/P<sub>0</sub> suggested the mesoporous property of



CoFe<sub>2</sub>O<sub>4</sub> nanosheets. The BET specific surface areas of CoFe<sub>2</sub>O<sub>4</sub> nanosheets was about 68.3 m<sup>2</sup> g<sup>-1</sup>. The inset of Figure 3c shows that the pore-size distribution of CoFe<sub>2</sub>O<sub>4</sub> nanosheets was mainly centered at 2-4 nm, also implying the mesoporous structure of the material.

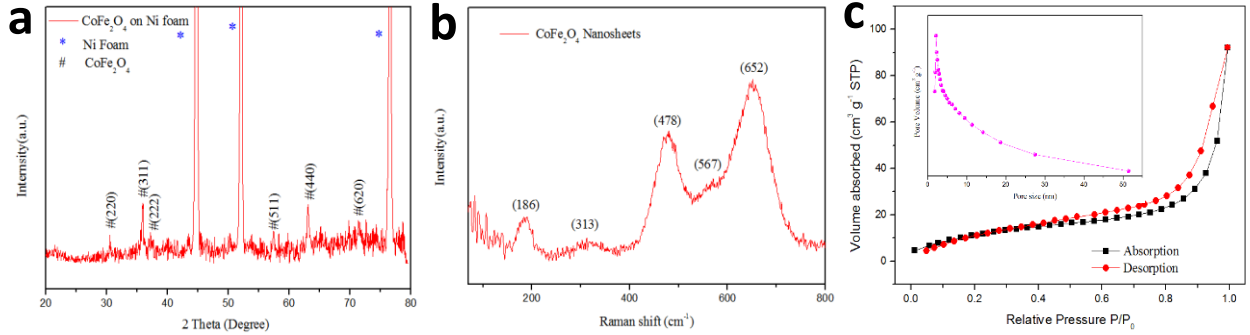


**Figure 3.** (a) XRD patterns and (b) Raman spectra of CoFe<sub>2</sub>O<sub>4</sub> nanosheets on Ni foam; (c) N<sub>2</sub> adsorption-desorption isotherms and inset shows the pore size distribution of CoFe<sub>2</sub>O<sub>4</sub> nanosheets.

Figure 4a-d present the morphologies of the as-obtained CoFe<sub>2</sub>O<sub>4</sub> nanosheets on the Ni foams. After hydrothermal growth and post-annealing process, uniform CoFe<sub>2</sub>O<sub>4</sub> nanosheets with high density grow aggregately on the Ni foam forming a channel opening and interconnecting architecture. Figure 4d and e show high magnification SEM and EDX analysis of CoFe<sub>2</sub>O<sub>4</sub> nanosheets. The thickness of CoFe<sub>2</sub>O<sub>4</sub> nanosheets were between 30 nm and 60 nm. The porous structure and ultrathin property of CoFe<sub>2</sub>O<sub>4</sub> nanosheets can shorten the diffusion distance from the external electrolyte to the interior reactive surface, facilitating an efficient, reversible Faradaic redox reaction and improving the utilization

rate of electrode material.<sup>46</sup> The atomic ratio of Fe/Co of the  $\text{CoFe}_2\text{O}_4$  nanosheets was approximately 2:1 according to the EDX data, confirming the formation of  $\text{CoFe}_2\text{O}_4$  nanosheets. The transmission electron microscopy (TEM) images further revealed highly porous texture as well as an ultrathin feature of  $\text{CoFe}_2\text{O}_4$  nanosheets, shown in Figure 4f-h. The magnified images (Figure 3h) clearly shows white spots in 2-4 nm, indicating that the mesopores are uniformly distributed throughout the surface of the nanosheets and consistence to the pore size distribution obtained by the  $\text{N}_2$  adsorption-desorption isotherms test. The formation of the pores in the nanosheets were likely attributed to the gas liberation of the decomposition of the precursors during thermal treatment.<sup>47</sup> The images of low magnifications (Figure 4f and 4g) implied that the nanosheets possessed coarse surfaces in which the interconnected nanoparticles formed sheet-like structures.

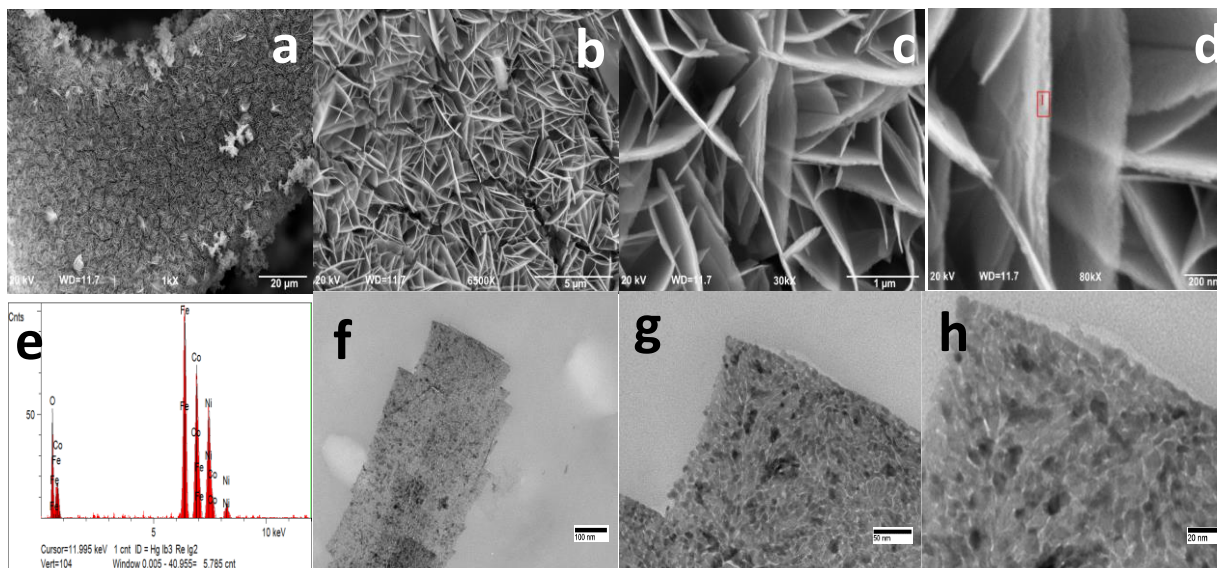


**Figure 4.** (a-d) SEM images of typical CoFe<sub>2</sub>O<sub>4</sub> nanosheets on Ni foam, (e) EDX analysis of CoFe<sub>2</sub>O<sub>4</sub> nanosheets and (f-h) TEM images of CoFe<sub>2</sub>O<sub>4</sub> nanosheets scratched from Ni foam.

XPS was further revealed elemental chemical states and chemical compositions on the surface of CoFe<sub>2</sub>O<sub>4</sub> nanosheets. Figure 5a is the full scan elemental survey of CoFe<sub>2</sub>O<sub>4</sub> nanosheets, confirming the presence of Co, Fe, O, C and Ni (coming from the Ni foam) elements. Figure 5b manifests the high-resolution O 1s spectra, in which a main peak at 529.8 eV and a low intensity peak at 531.5 eV were observed. The O1 peak at 529.8 eV represented a typical metal-oxygen bond and O2 peak at 531.5 corresponded to O in the multiplicity of physic- and chemisorbed water at the surface.<sup>48</sup> Figure 5c shows two core level peaks with a spin-orbit splitting about 15 eV correlated to the Co 2p spectra of CoFe<sub>2</sub>O<sub>4</sub> nanosheets. They were corresponded to Co 2p<sub>2/3</sub> and Co 2p<sub>1/2</sub> levels. The fitting peaks at 780.1 eV and the satellite peak of 787.5 eV were indexed to Co<sup>3+</sup>, while the fitting

peaks at 781.5 eV and 795.4 eV were associated with  $\text{Co}^{2+}$ .<sup>27, 49</sup> Figure 5d presents the Fe 2p core level spectra. The Fe 2p<sub>3/2</sub> split into two subpeaks after fitting at 710.6 and 712.7 eV (main peaks,  $\text{Fe}^{3+}$ ) with a “shoulder” satellite peak at 718.3 eV (satellite peaks,  $\text{Fe}^{2+}$ ). The fitting peak of Fe 2p<sub>1/2</sub> at 724.5 eV was indexed to  $\text{Fe}^{3+}$ .<sup>50</sup> The XPS spectra revealed the surface of the as-prepared  $\text{CoFe}_2\text{O}_4$  nanosheets was a mixed valence compound, which possessed a composition containing  $\text{Co}^{2+}$ ,  $\text{Co}^{3+}$ ,  $\text{Fe}^{2+}$  and  $\text{Fe}^{3+}$ .

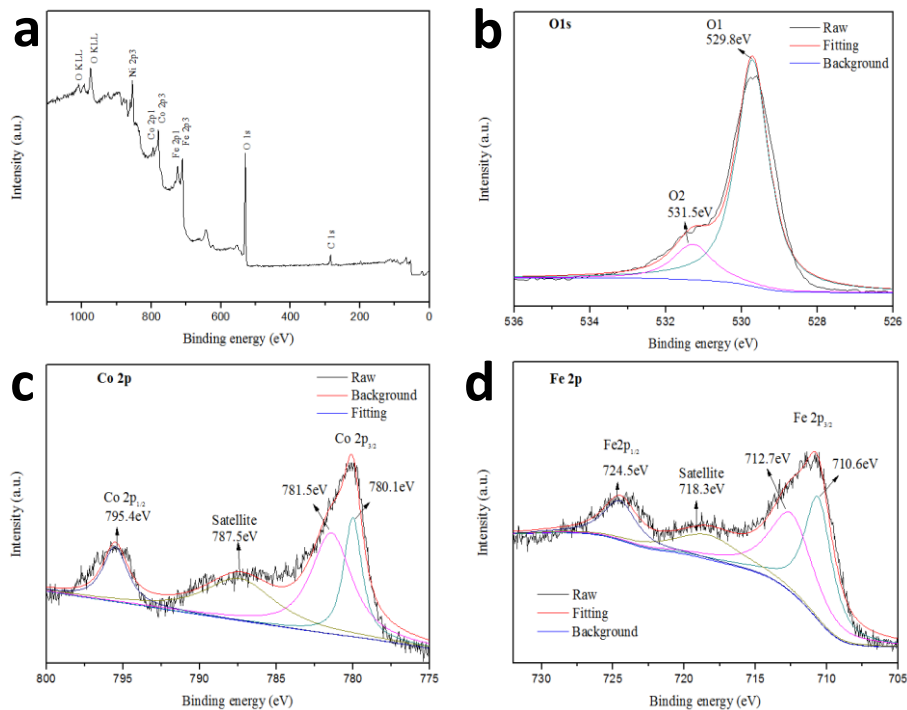


**Figure 5.** XPS spectra of the (a) survey, (b) O 1s (c) Co 2p, and (d) Fe 2p regions of  $\text{CoFe}_2\text{O}_4$  nanosheets on Ni foam.

### 3.1.2 Electrochemical properties of CoFe<sub>2</sub>O<sub>4</sub> electrode

The electrochemical performance of the CoFe<sub>2</sub>O<sub>4</sub> nanosheets grown on Ni foam was evaluated as binder-free electrodes for supercapacitors. The typical CV curves of the CoFe<sub>2</sub>O<sub>4</sub> nanosheets were obtained at different scan rates of 5, 10, 20, 40, 60, 80 and 100 mV s<sup>-1</sup>, as shown in Figure 6a. The CV curves of CoFe<sub>2</sub>O<sub>4</sub> nanosheets were deviated from rectangular character within the potential windows ranging from 0 to 0.5 V, indicating the pseudocapacitive behavior of the electrode. The shapes of these CV curves showed no significant change as the scan rate increasing, suggesting the excellent reversibility of the Faradaic redox reaction. The redox current almost increased linearly with the increase of scan rate, indicating the redox reaction was a diffusion-controlled process and the kinetics of interfacial Faradic redox reactions were efficient.<sup>51</sup> The property of the electrode was also studied by galvanostatic charge-discharge tests between 0 and 0.4 V (vs. Ag/AgCl) at different current densities. Figure 6b shows the charge-discharge curves of CoFe<sub>2</sub>O<sub>4</sub> nanosheets at different current densities. The specific capacitances of the CoFe<sub>2</sub>O<sub>4</sub> nanosheets electrode were 503, 482.5, 450, 420, 395 F g<sup>-1</sup> at different current densities of 2, 5, 10, 15 and 20 A g<sup>-1</sup>, respectively. Figure 6(c) shows CV curves of CoFe<sub>2</sub>O<sub>4</sub> and its two monometallic counterparts at a common scan rate of 10 mV s<sup>-1</sup>. The larger CV area of CoFe<sub>2</sub>O<sub>4</sub> than those of Co<sub>3</sub>O<sub>4</sub> and Fe<sub>3</sub>O<sub>4</sub> indicated a superior CoFe<sub>2</sub>O<sub>4</sub> in its capacitance. In addition, Figure 6(d) shows typical charge-discharge curves of CoFe<sub>2</sub>O<sub>4</sub>, Co<sub>3</sub>O<sub>4</sub> and Fe<sub>3</sub>O<sub>4</sub> at a current density of 2 A g<sup>-1</sup>, that was in accordance with the aforementioned CV curves.

The non-triangular shape of these charge-discharge curves manifested the Faradaic nature of the charge storage mechanism. The plateaus between 0.2 V and 0.3 V for  $\text{Fe}_3\text{O}_4$ , 0.3 and 0.35 for  $\text{Co}_3\text{O}_4$  and between 0.28 and 0.32 for  $\text{CoFe}_2\text{O}_4$  corresponded to the redox peaks in CV curves as shown in Figure 6(c). All samples presented symmetric charge and discharge curves indicating their good columbic efficiencies. The enhanced electrochemical properties including specific capacitance and conductivity of  $\text{CoFe}_2\text{O}_4$  nanosheets should be attributed the coexistence of two different cations in the bimetallic  $\text{CoFe}_2\text{O}_4$  and its unique nanosheets structure.

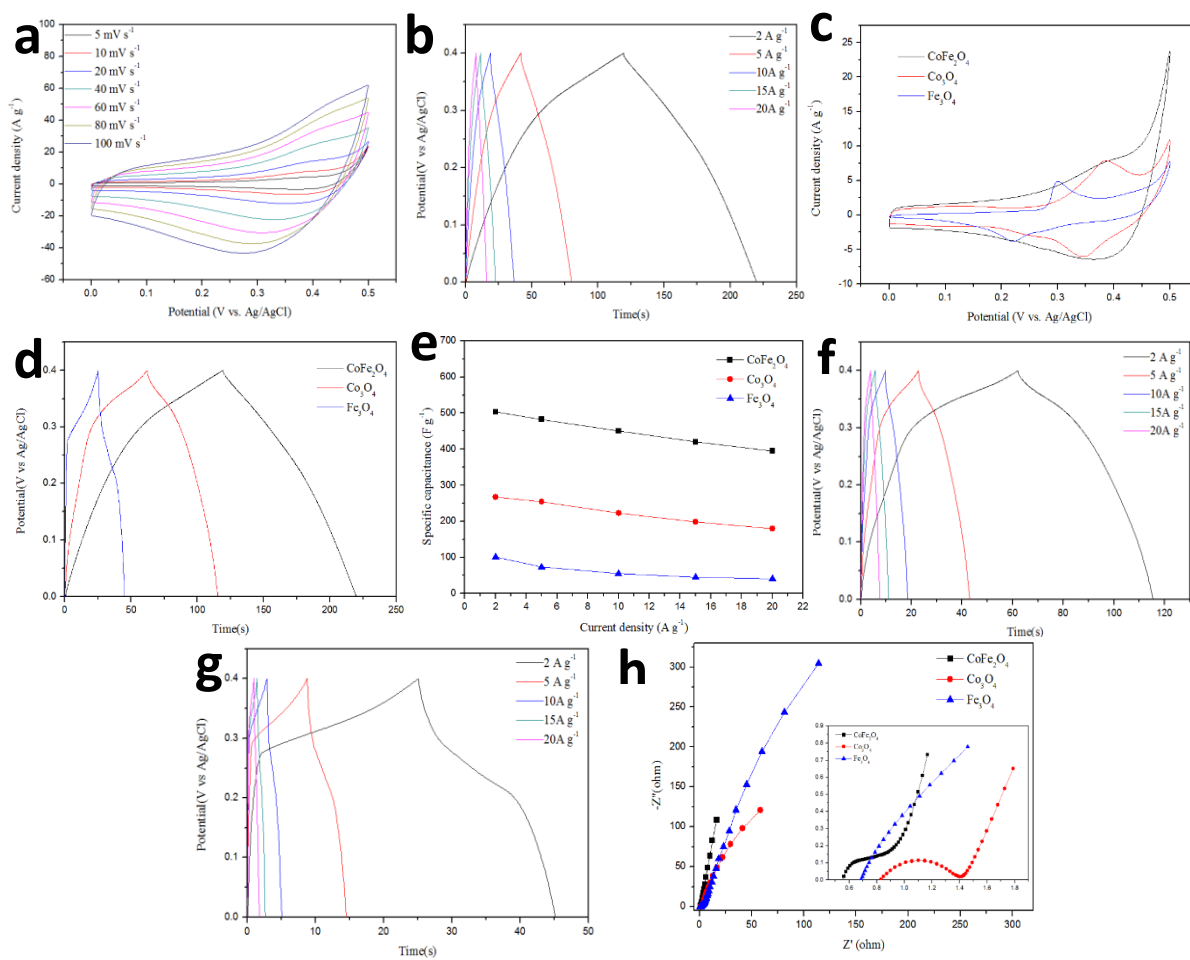


**Figure 6.** (a) CV curves of  $\text{CoFe}_2\text{O}_4$  nanosheets at different scan rates. (b) Galvanostatic charge-discharge of the  $\text{CoFe}_2\text{O}_4$  nanosheets at various current densities. (c-e) Comparing bare  $\text{CoFe}_2\text{O}_4$  electrode (black),  $\text{Co}_3\text{O}_4$  electrode (red) and  $\text{Fe}_3\text{O}_4$  electrode (blue), all grown on Ni foam: (c) CV curves at  $10 \text{ mV s}^{-1}$ , (d) galvanostatic charge-discharge at  $2 \text{ A g}^{-1}$ , (e) specific capacitances versus discharge current density. Galvanostatic charge-discharge of the (f)  $\text{Co}_3\text{O}_4$  and (g)  $\text{Fe}_3\text{O}_4$  at various current densities. (h) EIS curves (inset shows the EIS curves at high frequency).

The rate capability test and EIS measurement were also carried out to further understand

the superior pseudocapacitive performance of CoFe<sub>2</sub>O<sub>4</sub> nanosheets electrode. As shown in Figure 6e, when the current density was increased to 20 A g<sup>-1</sup>, which was 10-fold of the initial value, the capacitance of CoFe<sub>2</sub>O<sub>4</sub> nanosheets still remained 395 F g<sup>-1</sup>. The capacitance retention was 78.5% for CoFe<sub>2</sub>O<sub>4</sub> nanosheets, versus 67.4% for Co<sub>3</sub>O<sub>4</sub> and 40% for Fe<sub>3</sub>O<sub>4</sub>, indicating the excellent rate capability of the CoFe<sub>2</sub>O<sub>4</sub> nanosheets. The galvanostatic charge-discharge curves of Co<sub>3</sub>O<sub>4</sub> and Fe<sub>3</sub>O<sub>4</sub> at different current densities can be referred to Figure 6f-g, respectively. Figure 6h shows the EIS spectra of all samples with a semicircle at the high-frequency region and a straight line at the low-frequency region. The high-frequency intercept of the semicircle on the real axis can represent the series resistance (R<sub>s</sub>) and its diameter can represent the charge-transfer resistance (R<sub>ct</sub>) of the Faradaic process. Contrasting, the linear part in the low-frequency area is associated with resistance (Warburg resistance W) of electrolyte and ionic diffusion/transport into the electrode surface.<sup>52-53</sup> The inset of Figure 5f clearly shows that the R<sub>s</sub> for CoFe<sub>2</sub>O<sub>4</sub> nanosheets, Co<sub>3</sub>O<sub>4</sub> and Fe<sub>3</sub>O<sub>4</sub> electrodes are 0.56 Ω, 0.81 Ω and 0.69 Ω. In addition, the impedance spectra of CoFe<sub>2</sub>O<sub>4</sub> nanosheets electrode revealed a smaller semicircle compared to those of Co<sub>3</sub>O<sub>4</sub> and Fe<sub>3</sub>O<sub>4</sub> electrodes, indicating that the CoFe<sub>2</sub>O<sub>4</sub> electrode possessed a higher charge-transfer conductivity. The greater slope of the straight line in the low frequency range indicated the prominent capacitive performance.



### 3.1.3 Electrochemical performance of CoFe<sub>2</sub>O<sub>4</sub>//AC asymmetric supercapacitor

To further evaluate the practical application potentials of CoFe<sub>2</sub>O<sub>4</sub> nanosheets electrode, an aqueous ASC was first assembled using the CoFe<sub>2</sub>O<sub>4</sub> nanosheets electrode as a positive electrode and AC as a negative electrode. Figure 7a shows CV curves of AC electrode (black curve) and CoFe<sub>2</sub>O<sub>4</sub> nanosheets electrode (red curve) at a scan rate of 20 mV s<sup>-1</sup>. The rectangular-like shape between -1.0 and 0 V of AC electrode revealed its electrochemical double layer capacitance performance. In order to determine the optimal voltage window of this ASC, the CV measurements of the full cell were conducted within different cell voltages varying from 0-1.1 V to 0-1.5 V (Figure 7b). When the voltage window extended to 1.5 V, the CV curve of full cell still maintained a quasi-rectangular shape. Hence, the voltage window of 0-1.5 V was chosen to investigate the performance of the assembled CoFe<sub>2</sub>O<sub>4</sub>//AC ASC. Figure 7c shows the CV curves of CoFe<sub>2</sub>O<sub>4</sub>//AC ASC. When the scan rate was increased, the shape of the CV curves did not change significantly, indicating the high rate capability and good reversibility of the assembled cell. Figure 7d presents the galvanostatic charge-discharge curves of the ASC in a voltage window of 0-1.5 V. When the current density was higher than 1.6 A g<sup>-1</sup>, both charge and discharge curves showed a good symmetry, indicating an excellent capacitive character of CoFe<sub>2</sub>O<sub>4</sub>//AC ASC. The specific capacitances of the CoFe<sub>2</sub>O<sub>4</sub>//AC ASC were calculated according to the corresponding galvanostatic charge-discharge tests. It was found that the CoFe<sub>2</sub>O<sub>4</sub>//AC

ASC could deliver the maximum specific capacitance of  $73.12 \text{ F g}^{-1}$  at  $1.2 \text{ A g}^{-1}$  and still remained  $34.13 \text{ F g}^{-1}$  at  $8 \text{ A g}^{-1}$ . The cycling-life test of the  $\text{CoFe}_2\text{O}_4//\text{AC}$  ASC was recorded via a continuous charge-discharge at  $4.8 \text{ A g}^{-1}$ , as shown in Figure 7f. Impressively, the specific capacitance of the full cell still remain 98% of its initial value even after 5000 cycles (more than 150 000s), indicating long lifespan property of this ASC. Figure 7g-h shows the typical first and last ten charge-discharge cycles of 5000, revealing curves remained undistorted and almost symmetric. In order to further investigate electrochemical stability for the assembled  $\text{CoFe}_2\text{O}_4//\text{AC}$  ASC, EIS measurement of the  $\text{CoFe}_2\text{O}_4$  electrode after cycling test was performed (Figure 7i). EIS data implied that the value of  $R_s$  increased from  $0.56$  to  $0.85 \text{ } \Omega$  at the high-frequency region. Remarkably, the diameter of the semicircle was decreased after cycling test, revealing an improved charge-transfer conductivity was achieved after cycling tests.

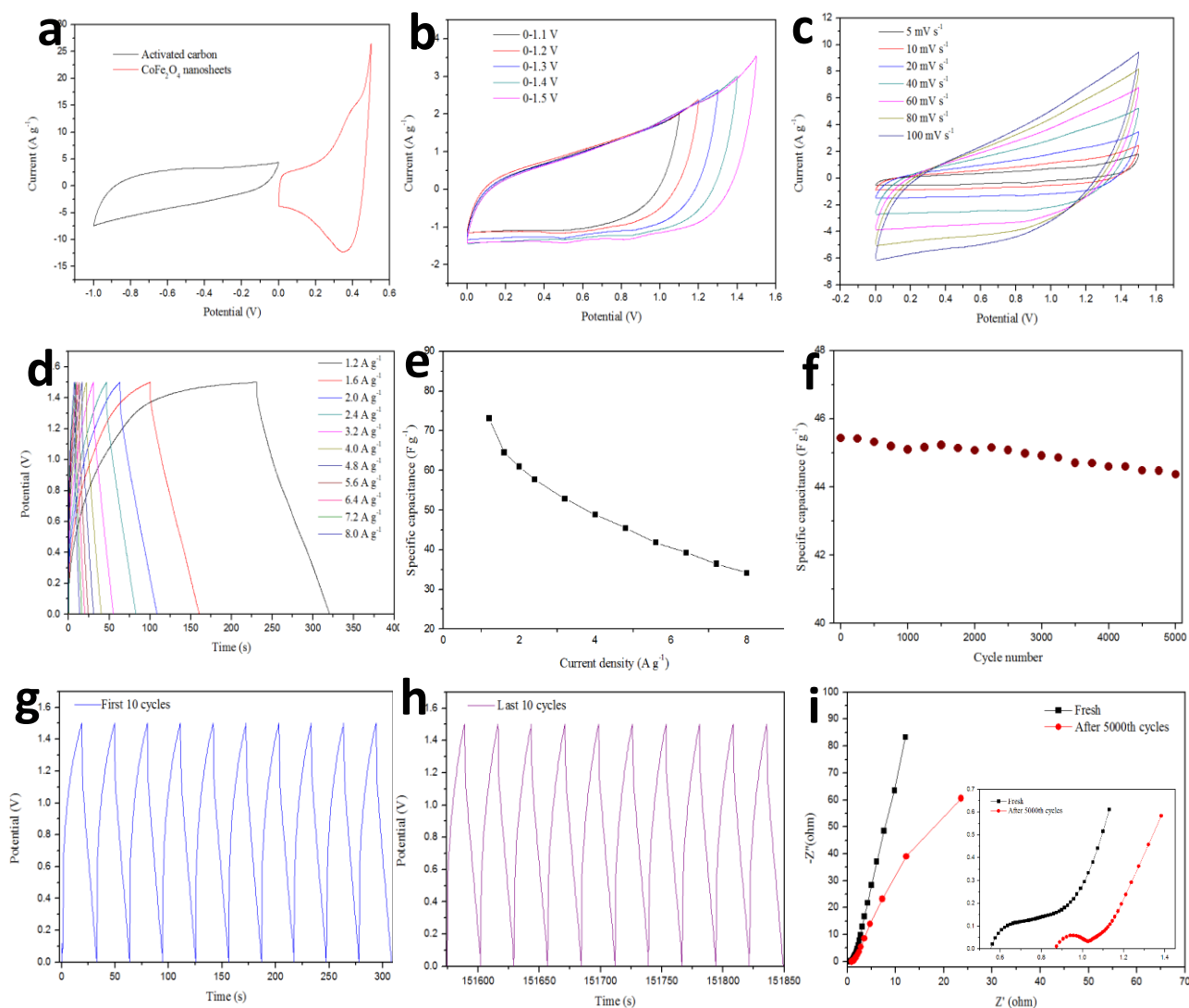


**Figure 7.** (a) Comparative CV curves of the activated carbon electrode and CoFe<sub>2</sub>O<sub>4</sub> electrode at 20 mV s<sup>-1</sup>. (b) CV curves at different cell voltages at a scan rate of 20 mV s<sup>-1</sup> and (c) different scan rates for CoFe<sub>2</sub>O<sub>4</sub> // AC-ASC device. (d) Galvanostatic charge-discharge curves at different current densities. (e) Specific capacitances of the CoFe<sub>2</sub>O<sub>4</sub> // AC-ASC device at different current densities. (f) Cycling stability of CoFe<sub>2</sub>O<sub>4</sub> // AC-ASC device at a current density of 4.8 A g<sup>-1</sup>. (g) First and (h) last 10 charge-discharge curves of CoFe<sub>2</sub>O<sub>4</sub>//AC ASC at 4.8 A g<sup>-1</sup> in the potential range between 0-1.5 V. (i) EIS curves of the fresh CoFe<sub>2</sub>O<sub>4</sub> @ MnO<sub>2</sub> electrode and after 5000th cycles.

Figure 8a presents the Ragone plot of CoFe<sub>2</sub>O<sub>4</sub>//AC ASC as well as several typical ASC reported in the literatures. The maximum energy density of CoFe<sub>2</sub>O<sub>4</sub>//AC ASC in this study was 22.85 W h kg<sup>-1</sup> at a power density of 900 W kg<sup>-1</sup>, and 10.67 W h kg<sup>-1</sup> was still maintained even at a high power density of 6000 W kg<sup>-1</sup>, which was higher than previously reported ASC such as Co<sub>3</sub>O<sub>4</sub> NWs//CA (17.9 W h kg<sup>-1</sup> at 750 W kg<sup>-1</sup>),<sup>54</sup> NiCo<sub>2</sub>O<sub>4</sub> NSs @ HMRA//AC (15.42 W h kg<sup>-1</sup> at 1000 W kg<sup>-1</sup>),<sup>55</sup> FeCo<sub>2</sub>O<sub>4</sub> NWs//AC (20 W h kg<sup>-1</sup> at about 2000 W kg<sup>-1</sup>),<sup>18</sup> NiO NSs//Fe<sub>2</sub>O<sub>3</sub> NRs (3.64 W h kg<sup>-1</sup> at 951 W kg<sup>-1</sup>),<sup>56</sup> Co(OH)<sub>2</sub>//AC (20.3 W h kg<sup>-1</sup> at 90.6 W kg<sup>-1</sup>),<sup>57</sup> CuCo<sub>2</sub>O<sub>4</sub>/CuO//AC (13 W h kg<sup>-1</sup> at 1509 W kg<sup>-1</sup>)<sup>58</sup> and GNCC//AC (7.6 W h kg<sup>-1</sup> at 5600 W kg<sup>-1</sup>).<sup>59</sup> After two CoFe<sub>2</sub>O<sub>4</sub>//AC ASCs were further connected in series and charged for 10s to about 3.0 V, the connected devices efficiently powered a red LED (1.8 V, 20 mA) and lasted for about 5 min (Figure 8b-c). In order to further study the benefit of asymmetric supercapacitor and the effect of negative electrode for the whole cell. A symmetric supercapacitor (SSC) was also assembled using CoFe<sub>2</sub>O<sub>4</sub> nanosheets electrodes as its both positive and negative electrodes, named as CoFe<sub>2</sub>O<sub>4</sub>//CoFe<sub>2</sub>O<sub>4</sub> SSC. The electrochemical properties of CoFe<sub>2</sub>O<sub>4</sub>//CoFe<sub>2</sub>O<sub>4</sub> SSC were studied by CV and GCD tests (Figure 8 d-e). Based on the GCD tests, the CoFe<sub>2</sub>O<sub>4</sub>//CoFe<sub>2</sub>O<sub>4</sub> SSC also achieved a high specific capacitance of 130 A g<sup>-1</sup> at a current density of 0.5 A g<sup>-1</sup>. The calculated maximum energy density (Figure 8f) of CoFe<sub>2</sub>O<sub>4</sub>//CoFe<sub>2</sub>O<sub>4</sub> SSC, based on the specific capacitance obtained from GCD tests, was 18.08 W h kg<sup>-1</sup> at a power density of 250 W kg<sup>-1</sup> and decreased to 4.8 W h kg<sup>-1</sup> at a power density of 2500 W kg<sup>-1</sup>. Obviously, the energy density and power density of CoFe<sub>2</sub>O<sub>4</sub>//CoFe<sub>2</sub>O<sub>4</sub> SSC were lower than those of

the  $\text{CoFe}_2\text{O}_4//\text{AC}$  ASC, indicating the ASC is an efficient strategy to improve the performance of supercapacitor cell.

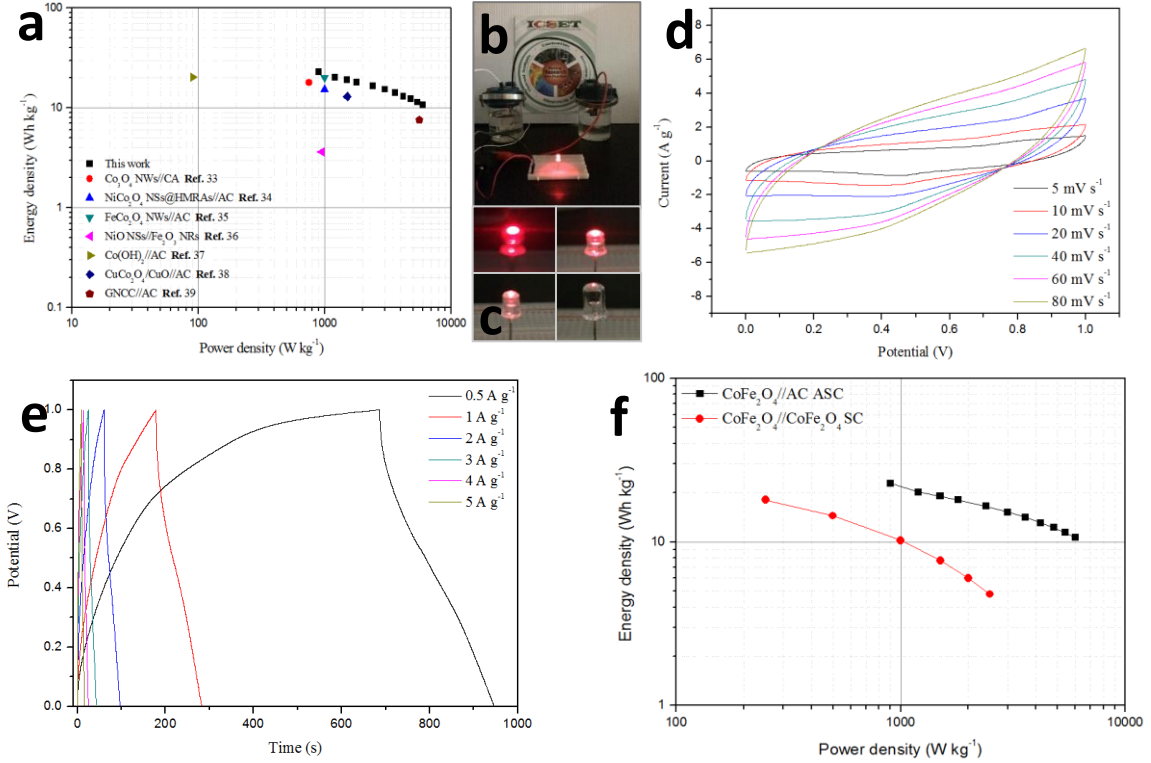
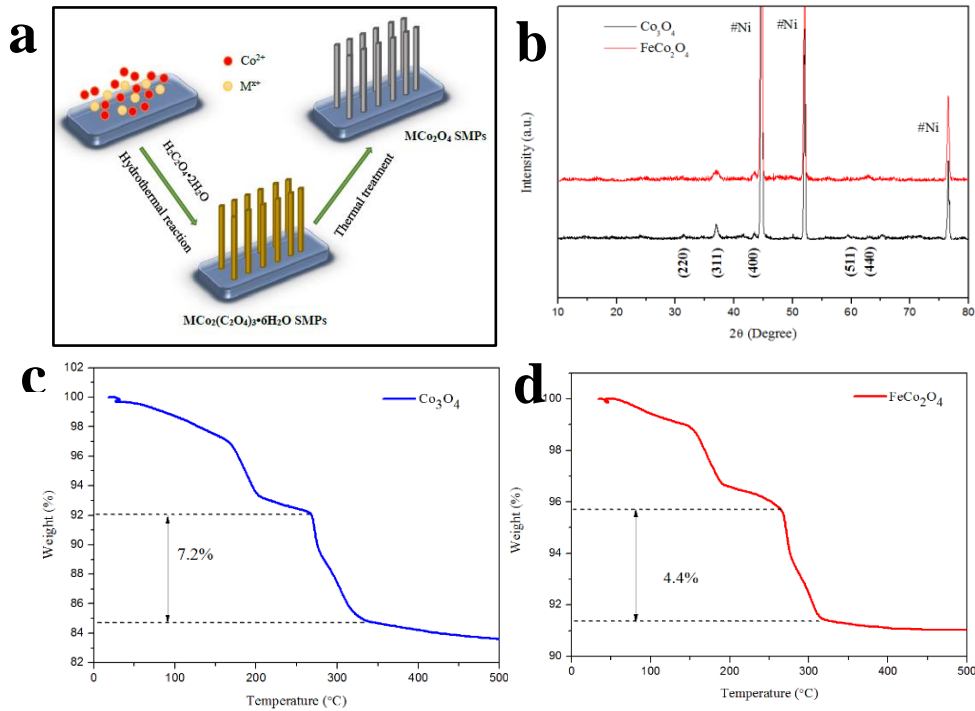
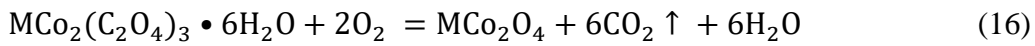


**Figure 8.** (a) Ragone plot of the  $\text{CoFe}_2\text{O}_4//\text{AC}$ -ASC device. The values reported for others devices are given here for a comparison. (b) A digital image showing the two ASC devices in series can light up one red LED indicator. (c) Images of the red LED at different stages; powered by the 10 s charged series supercapacitors (d) CV curves at different scan rates and (e) Galvanostatic charge-discharge curves at different current densities for  $\text{CoFe}_2\text{O}_4//\text{CoFe}_2\text{O}_4$  SSC device. (f) Ragone plot of the  $\text{CoFe}_2\text{O}_4//\text{AC}$  ASC and  $\text{CoFe}_2\text{O}_4//\text{CoFe}_2\text{O}_4$  SSC devices.

## 3.2 FeCo<sub>2</sub>O<sub>4</sub> submicron prisms grown on Ni foam as high-performance positive electrode for supercapacitor

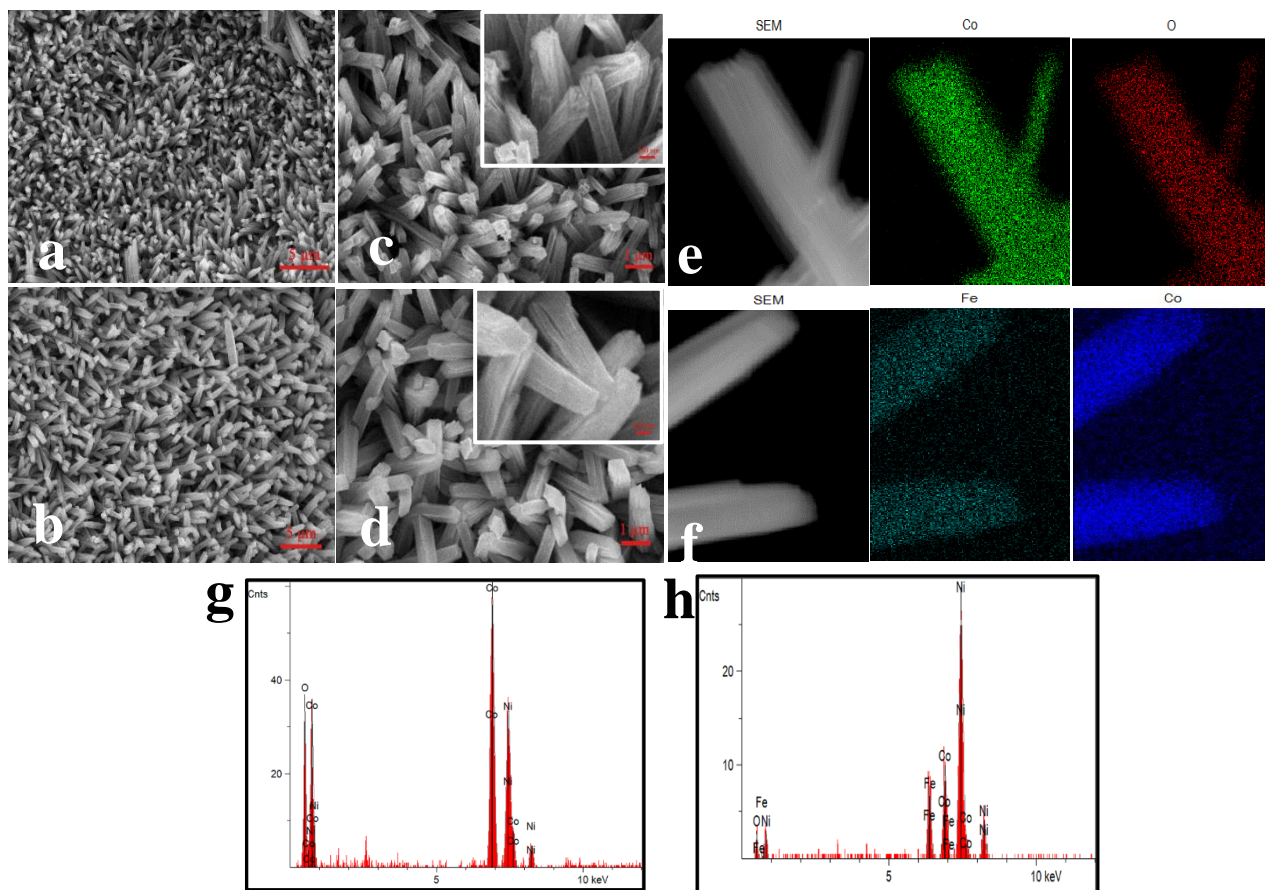
### 3.2.1 Material Characterization

Figure 9a schematically illustrates the synthesis route of MCo<sub>2</sub>O<sub>4</sub> SMPs (M=Fe and Co) on NF. Before the injection of oxalic acid solution, Co<sup>2+</sup> and M<sup>x+</sup> cations were attached on the surface of NF via the immersion process. After the introduction of oxalic acid solution, the cations reacted with oxalic acid to form the oxalate complex. Then, the oxalate seeds loaded on the NF evolved into the SMPs. The oxalate precursor would transfer into MCo<sub>2</sub>O<sub>4</sub> SMPs during thermal treatment according to the following equation:



**Figure 9.** (a) Schematic illustration of the fabrication of  $\text{MCo}_2\text{O}_4$  SMPs on NF; (b) XRD patterns of  $\text{MCo}_2\text{O}_4$  (M= Co and Fe) SMPs on NFs. TGA curves of (c)  $\text{Co}_3\text{O}_4$  and (d)  $\text{FeCo}_2\text{O}_4$ .

The crystal structures of the as-prepared materials were characterized using XRD. Figure 1b shows the XRD patterns of  $\text{MCo}_2\text{O}_4$  SMPs on NF. Except for three strong peaks at  $44.5^\circ$ ,  $52.1^\circ$ , and  $76.5^\circ$  which could be ascribed to Ni substrate, the remaining peaks were assigned to the (220), (311), (440), (511) and (440) reflections of cubic spinel-type  $\text{MCo}_2\text{O}_4$  with the space group of  $\text{Fd}\bar{3}\text{m}$ . The annealing temperatures and mass of active materials were obtained by TGA tests. Figure 9c-d shows the TGA curves of  $\text{MCo}_2\text{O}_4$  SMPs precursors. All the TGA exhibited weight losses in the  $120 - 200^\circ\text{C}$  and  $270 - 330^\circ\text{C}$  ranges. The first weight loss corresponded to the dehydration of chemically bonded water in  $\text{MCo}_2(\text{C}_2\text{O}_4)_3 \cdot 6\text{H}_2\text{O}$  complex.<sup>60</sup> The second mass loss was attributed to the decomposition of anhydrous oxalate precursors to  $\text{MCo}_2\text{O}_4$ . Based on the TGA analysis, the temperature for the calcination of the  $\text{MCo}_2(\text{C}_2\text{O}_4)_3 \cdot 6\text{H}_2\text{O}$  complex was set to  $400^\circ\text{C}$  to ensure the complete decomposition of the oxalate.<sup>61</sup> The loaded active materials in NFs also could be determined by TGA tests. The second weight losses for  $\text{Co}_3\text{O}_4$   $\text{FeCo}_2\text{O}_4$  are about 7.2%, 4.4% respectively. Thus, the mass densities of  $\text{MCo}_2\text{O}_4$  SMPs on NFs were about  $2.41 \text{ mg cm}^{-2}$  for  $\text{Co}_3\text{O}_4$ ,  $1.53 \text{ mg cm}^{-2}$  for  $\text{FeCo}_2\text{O}_4$  respectively.



**Figure 10.** SEM and element mapping images of  $M\text{Co}_2\text{O}_4$  SMPs on NF: (a), (c) and (e) for  $\text{Co}_3\text{O}_4$ , (b), (d) and (f) for  $\text{FeCo}_2\text{O}_4$ . EDX analysis of (g)  $\text{Co}_3\text{O}_4$  and (h)  $\text{FeCo}_2\text{O}_4$ .

The morphologies and submicron structures of  $M\text{Co}_2\text{O}_4$  SMPs on NFs were investigated by SEM. The scanning electron micrographs of the five types of  $M\text{Co}_2\text{O}_4$  SMPs clearly revealed submicron-prisms structure. The cross sections of all submicron prisms showed the quadrangle shapes. Figure 10a-b show the low-magnification SEM images of the  $M\text{Co}_2\text{O}_4$  SMPs ( $M = \text{Co}$  and  $\text{Fe}$  respectively). Surfaces of NFs were covered by SMPs uniformly and each single SMP was isolated from the others to form a porous architecture. Figure 10c-d and their insets present the magnifying SEM images of the  $M\text{Co}_2\text{O}_4$  SMPs.



The closer view of metal cobaltite oxides demonstrated these  $\text{MCo}_2\text{O}_4$  SMPs with different edge lengths. The average quadrangle edge lengths of  $\text{Co}_3\text{O}_4$ ,  $\text{FeCo}_2\text{O}_4$  were about 350 nm, 450 nm respectively. The components of  $\text{MCo}_2\text{O}_4$  SMPs were confirmed by the elemental mapping (Figure 10e-f). The co-existence and similar shapes of O and Co for  $\text{Co}_3\text{O}_4$ , Fe and Co for  $\text{FeCo}_2\text{O}_4$  confirmed the uniform distribution of the corresponding elements of  $\text{MCo}_2\text{O}_4$  in the whole investigation regions. The atomic ratios of O/Co and Fe/Co were verified by the EDX spectroscopy (Figure 10g-h). The EDX data displayed that the  $\text{Co}_3\text{O}_4$  SMPs comprised O and Co elements with atomic ratio of 4:3 and  $\text{FeCo}_2\text{O}_4$  SMPs comprised Fe and Co elements with atomic ratio of almost of 1:2, suggesting the successful fabrication of  $\text{Co}_3\text{O}_4$  and  $\text{FeCo}_2\text{O}_4$  SMPs.

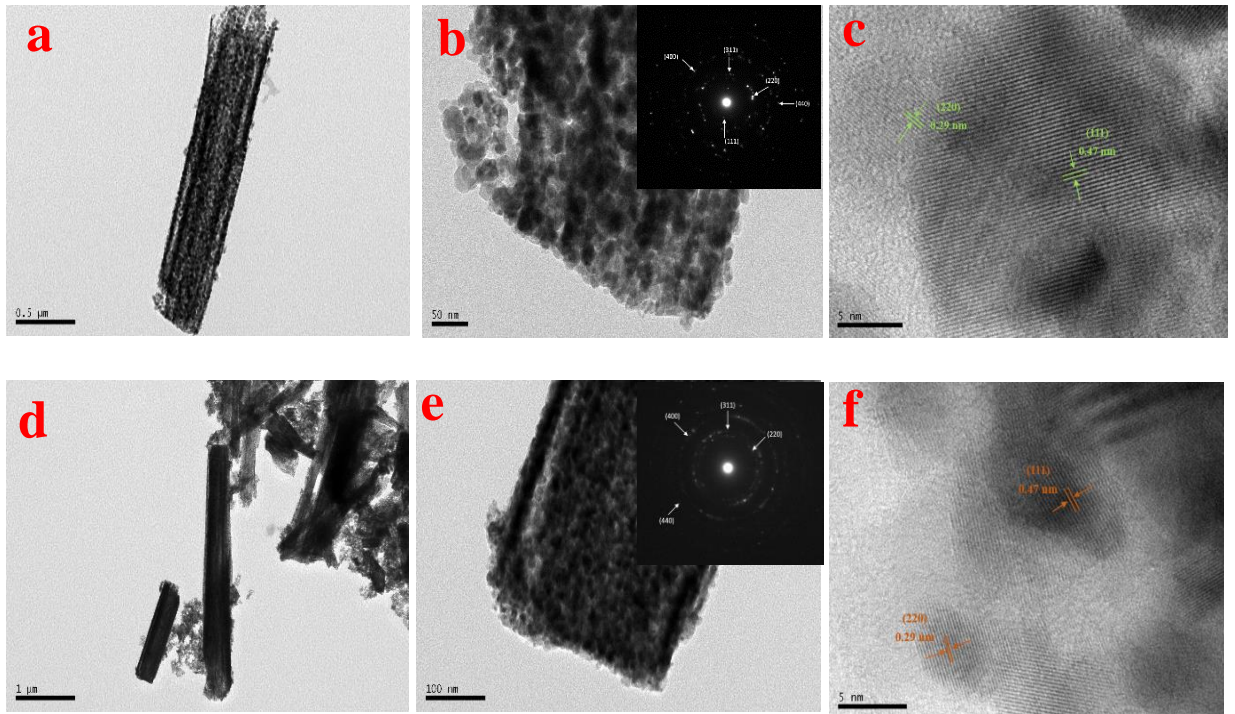


**Figure 11.** TEM and HRTEM images of  $\text{MCo}_2\text{O}_4$  SMPs scratched from NFs. (a-c) for  $\text{Co}_3\text{O}_4$ , (d-f) for  $\text{FeCo}_2\text{O}_4$ . (Insets of b, e are the SAED patterns of  $\text{MCo}_2\text{O}_4$  SMPs)

Figure 11 presents the TEM and HRTEM images of as-synthesized  $\text{MCo}_2\text{O}_4$  SMPs. The submicron-structured prisms of  $\text{MCo}_2\text{O}_4$  (M= Co and Fe) were revealed by the TEM images. The edge lengths of  $\text{MCo}_2\text{O}_4$  SMPs were also confirmed by TEM images which were close to the results observed in SEM results. Figure 11b and e exhibited the magnified TEM images of  $\text{MCo}_2\text{O}_4$  (M= Co and Fe) SMPs. Some pores (the white spots) distributed in the whole SMPs uniformly, which could likely be generated by the liberation of gases during the heat treatment of precursors. The porous structure facilitated the diffusion of electrolyte into the active materials, providing more reactive sites for redox reactions. All the SAED patterns revealed that the  $\text{MCo}_2\text{O}_4$  SMPs were generally crystalline and consistent with the diffraction patterns obtained by XRD. The resolved lattice fringes shown in the HRTEM images of  $\text{MCo}_2\text{O}_4$  SMPs were approximately 0.47 nm, 0.29 nm, and 0.25 nm, corresponding to the (111), (220) and (311) planes of the  $\text{MCo}_2\text{O}_4$  spinel phase.<sup>62</sup> The HRTEM and SAED patterns further confirmed the formation of crystalline phase metal oxides.

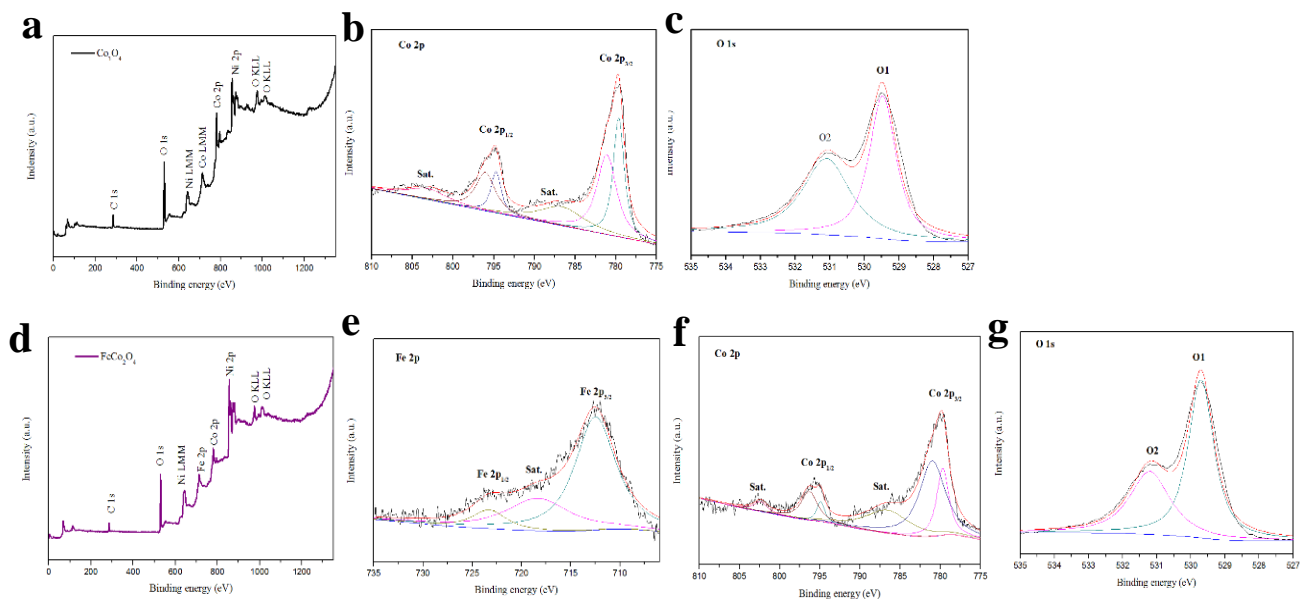


**Figure 12.** (a-c) XPS spectra of the  $\text{Co}_3\text{O}_4$  (a) survey, (b) Co 2p, (c) O 1s and (d-g)  $\text{FeCo}_2\text{O}_4$ , (d) survey, (e) Fe 2p, (f) Co 2p, (g) O 1s.

The elemental chemical states and chemical compositions on the surfaces of as-prepared materials were further investigated by X-ray photoelectron (XPS). Figure 12 a and d show the full scan elemental surveys of  $\text{Co}_3\text{O}_4$  and  $\text{FeCo}_2\text{O}_4$  SMPs on NFs. Amongst, the co-existence of Fe and Co also confirmed the formation of  $\text{FeCo}_2\text{O}_4$  on NFs. The peak deconvolution and fitting were conducted using Gaussian-Lorentzian method. Figure 12 b and f exhibit the high-resolution Co 2p of  $\text{Co}_3\text{O}_4$  and  $\text{FeCo}_2\text{O}_4$ , respectively. Two main peaks which can be attributed to the Co  $2p_{3/2}$  and Co  $2p_{1/2}$  and two satellite peaks (denoted as Sat.) were observed. After fitting, the peaks at 779.7 eV, 794.8 eV, and satellite peak at 786.6 eV were indexed to  $\text{Co}^{3+}$ , while the remaining peaks were attributed to the existence

of  $\text{Co}^{2+}$ .<sup>63-64</sup> This result indicated the cobalt in  $\text{Co}_3\text{O}_4$  SMPs were a mixture of  $\text{Co}^{3+}$  and  $\text{Co}^{2+}$ . Figure 12e presents two main peaks corresponding to Fe  $2p_{3/2}$  and Fe  $2p_{1/2}$  and one broad satellite peak. The fitted peaks at 712.7 eV and 724.3 eV could be characterized to  $\text{Fe}^{3+}$ , while the “shoulder” satellite peak at 718.3 eV was ascribed to  $\text{Fe}^{2+}$ . The result also indicated that the  $\text{FeCo}_2\text{O}_4$  SMPs was a composition containing  $\text{Fe}^{2+}$  and  $\text{Fe}^{3+}$ . Figure 12c and g elucidate the O 1s XPS spectra of  $\text{Co}_3\text{O}_4$  and  $\text{FeCo}_2\text{O}_4$  SMPs on NFs. Likewise, all the O 1s were divided into two fitting peaks at 529.7 eV and 531.3 eV, which could be attributed to the typical metal-oxygen bond and the multiplicity of physis- and chemisorbed water at the surface.<sup>65</sup>

### 3.2.2 Electrochemical properties of $\text{FeCo}_2\text{O}_4$ electrode

The electrochemical properties of  $\text{MCo}_2\text{O}_4$  (M= Co, Fe) SMPs were investigated using CV tests first. Figure 13a shows the CV curves of  $\text{MCo}_2\text{O}_4$  (M= Co, Fe) SMPs electrodes at a scan rate of  $5 \text{ mV s}^{-1}$  within a potential window of  $-0.1 - 0.6 \text{ V}$ . All the CV curves of  $\text{MCo}_2\text{O}_4$  (M= Co, Fe) SMPs showed obvious redox peaks corresponding to the reversible faradaic reactions of  $\text{M-O/M-O-OH}$ . It is noteworthy that the redox peaks of  $\text{FeCo}_2\text{O}_4$  was wider than  $\text{Co}_3\text{O}_4$ , indicating enhanced redox reactions were occurred with the introduction of elements Fe. Figure 13b demonstrates the GCD processes of  $\text{MCo}_2\text{O}_4$  (M= Co, Fe) SMPs at a current density of  $10 \text{ mA cm}^{-2}$ . All the GCD curves exhibited two visible potential plateaus in the charge and discharge processes, which were in agreement with the

CV measurements. The GCD curves of  $M\text{Co}_2\text{O}_4$  ( $M = \text{Co}, \text{Fe}$ ) indicated the capacitive and battery-type properties of these materials. Furthermore, the rate capabilities of the  $M\text{Co}_2\text{O}_4$  ( $M = \text{Co}, \text{Fe}$ ) were studied by the GCD tests at different current densities. Figure 13c-d show the discharge curves of  $\text{Co}_3\text{O}_4$  and  $\text{FeCo}_2\text{O}_4$ , respectively. After integrating the covered areas of their discharge curves at different current densities, the areal capacitances and specific capacitances were calculated according to equation (12) and (13). The specific capacitances (areal capacitances) of  $\text{Co}_3\text{O}_4$ ,  $\text{FeCo}_2\text{O}_4$  were  $680.5 \text{ F g}^{-1}$  ( $1.64 \text{ F cm}^{-2}$ ),  $1281.0 \text{ F g}^{-1}$  ( $1.96 \text{ F cm}^{-2}$ ), respectively, at a current density of  $2 \text{ mA cm}^{-2}$ . With the increase of current density, the specific capacitance of  $M\text{Co}_2\text{O}_4$  decayed in varying degrees, which could be attributed to the limitation of ions diffusion and migration within the electrode at a higher discharge current density. When the current density increased to  $40 \text{ mA cm}^{-2}$  (20-fold of  $2 \text{ mA cm}^{-2}$ ), the capacitance of  $M\text{Co}_2\text{O}_4$  ( $M = \text{Co}, \text{Mn}, \text{Fe}, \text{Mg}$  and  $\text{Zn}$ ) remained about 45.1% and 23.5% of their initial values, respectively (Figure 13 e and f).

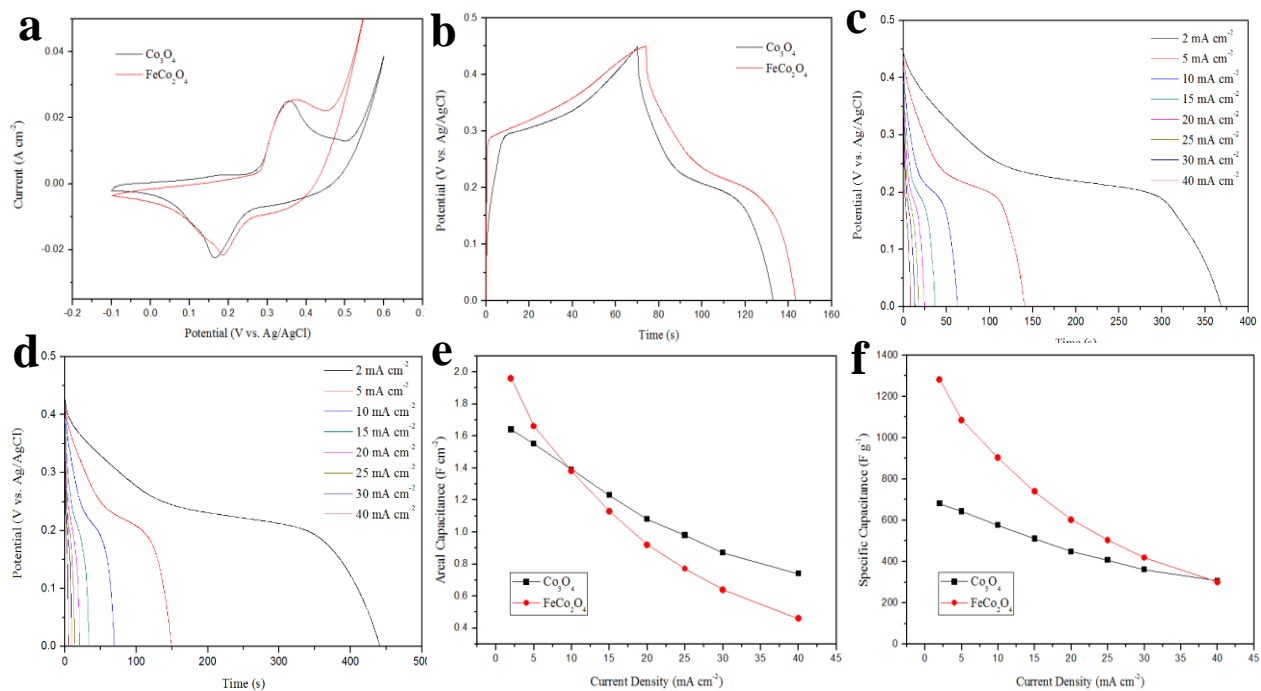


**Figure 13.** (a) CV curves of  $MCo_2O_4$  (M= Co, Fe) SMPs at a scan rate of  $5 \text{ mV s}^{-1}$ ; (b) GCD curves of  $MCo_2O_4$  (M= Co, Fe) SMPs at a current density of  $10 \text{ mA cm}^{-2}$ ; Discharge curves of (c)  $Co_3O_4$ , (d)  $FeCo_2O_4$  SMPs at different current densities. (e) areal capacitance and (f) specific capacitance of  $MCo_2O_4$  (M= Co, Fe) SMPs at different current densities.

The pseudocapacitive behavior of  $MCo_2O_4$  (M= Co, Fe) SMPs were also investigated by CV tests at different scan rate. Figure 14a-b describes the CV curves of  $MCo_2O_4$  (M= Co, Fe) at different scan rates from  $5 \text{ mV s}^{-1}$  to  $50 \text{ mV s}^{-1}$ , respectively. Obviously, the overall shapes of all  $MCo_2O_4$  (M= Co, Fe) CV curves can be well retained at different scan rates with slight shifts in the redox peak positions, indicating their excellent charge transfer and good reversibility features. In order to determine whether the capacitance originated

from surface redox reactions or bulk diffusion, the relationship of scan rate and voltammetric current were investigated. Figure 14c plots the anodic peak currents of  $\text{MCo}_2\text{O}_4$  (M= Co, Fe) against the square root of the scan rates, a linear dependency were obtained, implying the redox reactions of  $\text{MCo}_2\text{O}_4$  (M= Co, Fe) were controlled by the bulk diffusion rather than surface redox reaction. The diffusion coefficients of all materials were proportional to the slopes of the  $j_p$  vs.  $\nu^{1/2}$  according to the Randles-Sevcik equation:<sup>66</sup>

$$j_p = (0.446 C \cdot D^{1/2} \cdot \nu^{1/2} (n \cdot F/R) \cdot T)^{1/2} \quad (17)$$

where  $j_p$  is the anodic peak current in  $\text{A cm}^{-2}$ ,  $C$  is the solution bulk concentration,  $D$  is the diffusion coefficient,  $\nu$  is the scan rate in  $\text{mV s}^{-1}$ ,  $n$  is the number of exchanged electrons involved in the reaction,  $F$  is the Faraday's constant,  $R$  is the gas constant and  $T$  is the absolute temperature, respectively. After plotting the  $j_p$  of  $\text{MCo}_2\text{O}_4$  (M= Co, Fe) against  $\nu^{1/2}$ , the  $\text{Co}_3\text{O}_4$  exhibited higher slope than  $\text{FeCo}_2\text{O}_4$ , indicating its greater diffusion coefficient.

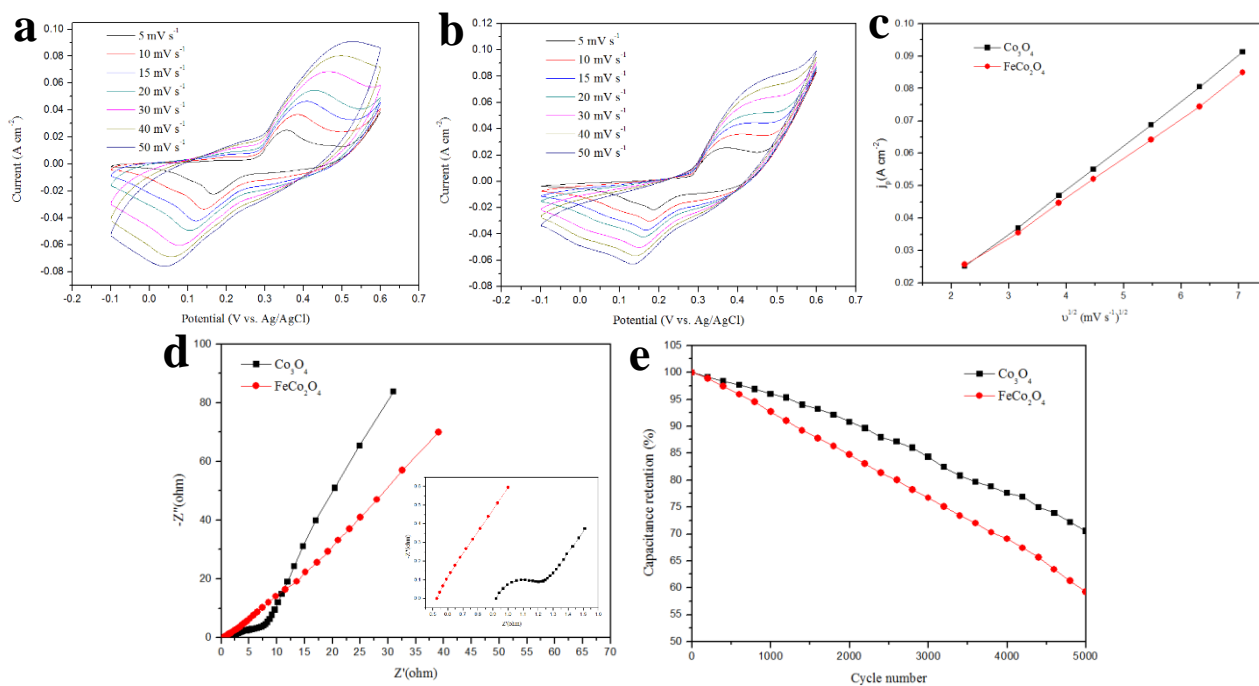


**Figure 14.** CV curves of (a)  $\text{Co}_3\text{O}_4$ , (b)  $\text{FeCo}_2\text{O}_4$  SMPs at different scan rates. (c) Relationship between the anodic peak current densities and square root of scan rates for the  $\text{MCo}_2\text{O}_4$  ( $\text{M} = \text{Co}, \text{Fe}$ ) SMPs electrodes; (b) EIS curves (inset shows the EIS curves at the high frequency) and (c) cycling stability of  $\text{MCo}_2\text{O}_4$  ( $\text{M} = \text{Co}, \text{Fe}$ ) SMPs electrodes.

In order to further evaluate the ion transport kinetics and the conductivities of  $\text{MCo}_2\text{O}_4$  ( $\text{M} = \text{Co}, \text{Fe}$ ) SMPs, EIS measurements were conducted. Figure 14d shows the Nyquist plots of the  $\text{MCo}_2\text{O}_4$  ( $\text{M} = \text{Co}, \text{Fe}$ ) SMPs electrodes (inset shows the EIS curves at high frequency). As shown in Figure 14d, the EIS curves of all  $\text{MCo}_2\text{O}_4$  SMPs electrodes can be divided into three sections: (1) the intersection of the curve on the real axis represents the series resistance ( $R_s$ ) at the high-frequency region; (2) the diameter of semicircle at the intermediate frequency represents the Faradaic charge transfer resistance ( $R_{ct}$ ); (3)



the slope of straight line at the low frequency region represents the Warburg impedance. The series resistance is the combination of inherent active material resistance, electrolyte resistance and contact resistance and can be calculated from the EIS curves. The  $R_s$   $\text{Co}_3\text{O}_4$ ,  $\text{FeCo}_2\text{O}_4$ , SMPs were  $0.92 \Omega$  and  $0.527 \Omega$ , respectively. The bimetallic oxides  $\text{FeCo}_2\text{O}_4$  SMPs exhibited better conductivities than monometallic oxide  $\text{Co}_3\text{O}_4$ , which should be attributed to the synergistic effect of two different cations in a single crystal structure. Warburg impedance, reflecting the resistance behaviour caused by the diffusion of  $\text{OH}^-$  within electrode materials during redox reactions, is associated with the slope of straight line at the low-frequency region in the EIS curves. Remarkably, the slopes of  $\text{MCo}_2\text{O}_4$  (M= Co, Fe) SMPs in their EIS curves demonstrated that the order of slopes were  $\text{Co}_3\text{O}_4 > \text{FeCo}_2\text{O}_4$ , which was well consistent with the results obtained from the Randles-Sevcik theory. This result further conveyed the redox reactions of  $\text{MCo}_2\text{O}_4$  (M= Co, Fe) SMPs were dominated by the  $\text{OH}^-$  diffusion within electrode materials.

The stability of electrodes during continuous charge-discharge cycles was studied by long-term cycling test at a high current density of  $20 \text{ mA cm}^{-2}$ . Figure 14e shows the capacitance retention of  $\text{MCo}_2\text{O}_4$  (M= Co, Fe) SMPs electrodes. The specific capacitances of  $\text{MCo}_2\text{O}_4$  (M= Co, Fe) SMPs were about 70.55 % and 59.3 % of their initial values after 5000 cycles. Figure 14 a-d show the first and last ten GCD tests of  $\text{MCo}_2\text{O}_4$  (M= Co, Fe) SMPs, respectively. The shapes of their GCD curves remained undistorted except for the start potentials of charge and discharge plateaus. In order to investigate the possible reasons for the loss of capacitance, the morphologies of  $\text{MCo}_2\text{O}_4$  (M= Co, Fe) SMPs after

cycling were analysed by SEM. The high-magnification SEM images of  $M\text{Co}_2\text{O}_4$  ( $M = \text{Co}, \text{Fe}$ ) SMPs in Figure 15e and g still maintained their original morphologies, indicating their highly mechanical stabilities. The decay of specific capacitance of  $M\text{Co}_2\text{O}_4$  electrodes should be attributed to the loss of active materials from NFs during cycling test in three-electrode system according to the low-magnification SEM images in Figure 15f and h.

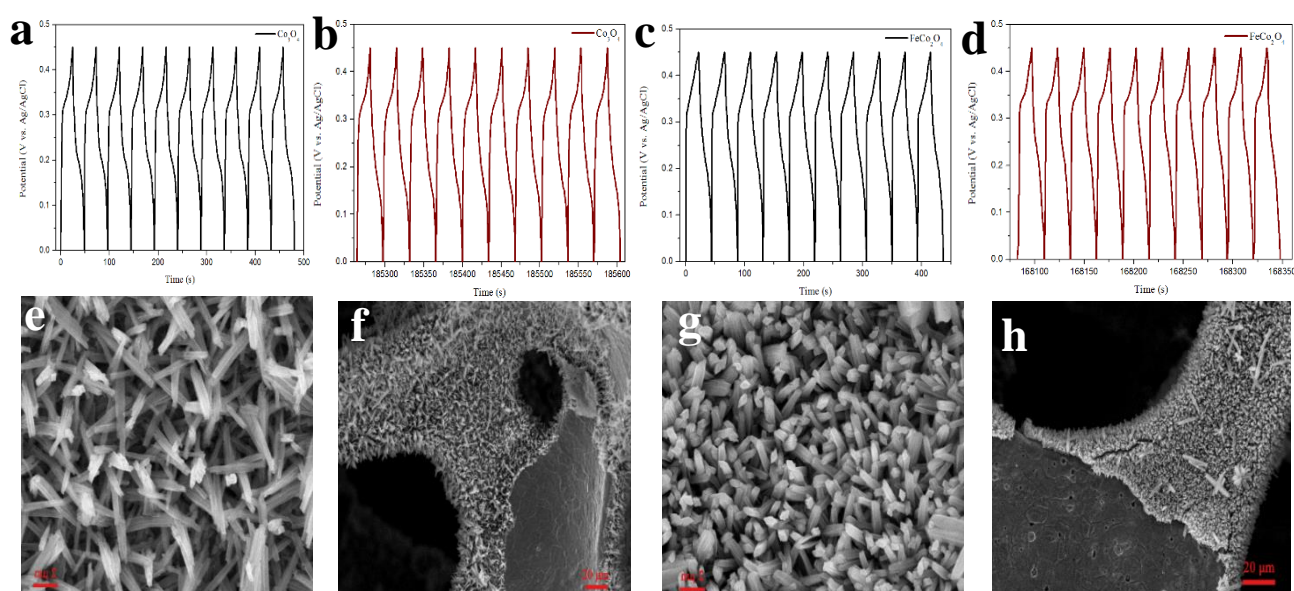


**Figure 15.** (a and c) First ten GCD curves and (b and d) last ten GCD curves for  $M\text{Co}_2\text{O}_4$  ( $M = \text{Co}, \text{Fe}$ ). SEM images of (e-f) for  $\text{Co}_3\text{O}_4$ , (g-h) for  $\text{FeCo}_2\text{O}_4$ , after 5000 cycling tests in three-electrode system.

### 3.3 Hierarchical core-shell nanosheet arrays with MnO<sub>2</sub> grown on mesoporous CoFe<sub>2</sub>O<sub>4</sub> support for high-performance asymmetric supercapacitors

#### 3.3.1 Material Characterization

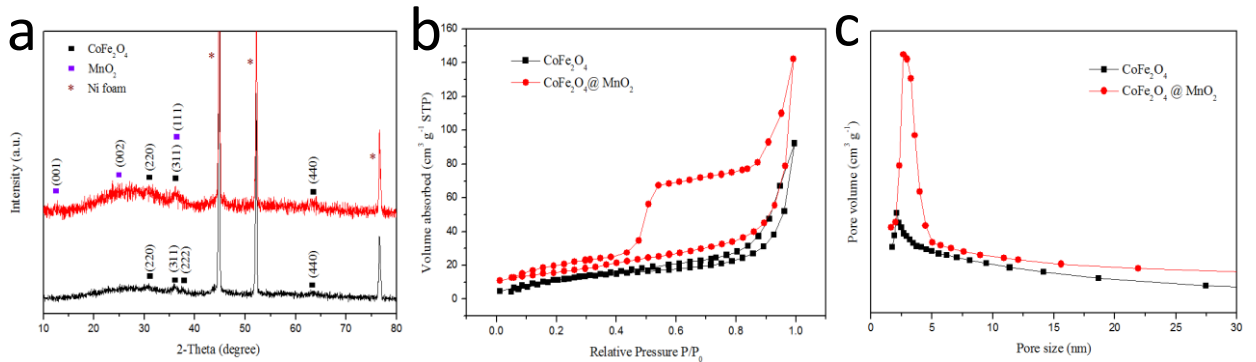


**Figure 16.** (a) XRD patterns of CoFe<sub>2</sub>O<sub>4</sub> nanosheets on Ni foam before (black curve) and after MnO<sub>2</sub> covering (red curve). (b) N<sub>2</sub> adsorption-desorption isotherms and (c) pore-size distribution of CoFe<sub>2</sub>O<sub>4</sub> and CoFe<sub>2</sub>O<sub>4</sub>@MnO<sub>2</sub> core-shell NSAs.

The crystal structures of the as-fabricated samples were characterized using XRD. The black curve in Figure 16a shows the XRD diffraction peaks of CoFe<sub>2</sub>O<sub>4</sub> NSs on the Ni foam before the MnO<sub>2</sub> growth. Except for the peaks at 44.5°, 52.1° and 76.5° corresponding to Ni foam, the remaining peaks at 2θ = 30.5°, 36.0°, 37.8° and 63.2° can be assigned to the (220), (311), (222) and (440) reflections of spinel CoFe<sub>2</sub>O<sub>4</sub> with the space group of Fd3m (JCPDS No: 22-1086). The diffraction pattern clearly confirm the phase purity of synthesized CoFe<sub>2</sub>O<sub>4</sub> and was in good accordance to those in previous reports.<sup>43, 67</sup> After the growth of MnO<sub>2</sub> on CoFe<sub>2</sub>O<sub>4</sub> NSs (red curve), most CoFe<sub>2</sub>O<sub>4</sub>

diffraction peaks still existed except for the reflection of (222) at  $37.8^\circ$ , which may be attributed to partly overlapping the (111) reflection in  $\text{MnO}_2$  and (311) reflection in  $\text{CoFe}_2\text{O}_4$ . The new peaks at  $12.3^\circ$  and  $25.0^\circ$  can be indexed to (001) and (002) reflections of birnessite-type  $\delta\text{-MnO}_2$  (JCPDS No: 86-0666). The XRD results revealed the co-existence of  $\delta\text{-MnO}_2$  and  $\text{CoFe}_2\text{O}_4$  on the Ni foam. The mesoporous properties of the as-fabricated samples were investigated by the surface area and the pore size distribution analysis. As shown in Figure 16b, the  $\text{N}_2$  adsorption-desorption isotherms of the  $\text{CoFe}_2\text{O}_4$  and  $\text{CoFe}_2\text{O}_4@\text{MnO}_2$  NSAs demonstrated distinct hysteresis loops in the range of 0.5-1.0  $P/P_0$ , indicating the mesoporous properties of  $\text{CoFe}_2\text{O}_4$  and  $\text{CoFe}_2\text{O}_4@\text{MnO}_2$  NSAs. The Brunauer-Emmett-Teller (BET) surface area values of  $\text{CoFe}_2\text{O}_4$  and  $\text{CoFe}_2\text{O}_4@\text{MnO}_2$  NSAs were calculated to be about 68 and  $156 \text{ m}^2 \text{ g}^{-1}$ , respectively. After the deposition of  $\text{MnO}_2$  nanosheets on the  $\text{CoFe}_2\text{O}_4$ , the surface area of active materials was dramatically enlarged which could provide more active sites for the redox reaction. The incremental pore-size distribution of the samples is shown in Figure 16c. Both the  $\text{CoFe}_2\text{O}_4@\text{MnO}_2$  NSAs and  $\text{CoFe}_2\text{O}_4$  nanosheets exhibited a pore-size distribution at 2-4 nm, further supporting the mesoporous properties of the prepared samples.

The morphologies of  $\text{CoFe}_2\text{O}_4$  NSs and  $\text{CoFe}_2\text{O}_4@\text{MnO}_2$  core-shell NSAs on Ni foam were investigated by the SEM in Figure 17. Panels a and b show SEM images of  $\text{CoFe}_2\text{O}_4$  NSs at different magnifications. After hydrothermal growth and post-annealing process, uniform  $\text{CoFe}_2\text{O}_4$  NSs with an average width about  $3 \mu\text{m}$  grown on the Ni foam and tended to interconnect with each other forming a three-dimensional porous structure. The

thickness of  $\text{CoFe}_2\text{O}_4$  NSs was found around 30 nm in the high magnification SEM image (Figure 17b). The porous and ultrathin  $\text{CoFe}_2\text{O}_4$  NSs provided a favorable condition for the growth of  $\text{MnO}_2$  NSs. The typical images of  $\text{CoFe}_2\text{O}_4@\text{MnO}_2$  core-shell NSAs are presented in Figure 17c and d. The  $\text{MnO}_2$  NSs with high density were scarcely packed in the space between  $\text{CoFe}_2\text{O}_4$  NSs, indicating  $\text{MnO}_2$  NSs tended to grow on the surface of  $\text{CoFe}_2\text{O}_4$  NSs. A high magnification SEM image of  $\text{CoFe}_2\text{O}_4@\text{MnO}_2$  core-shell NSAs is shown in Figure 17d. It was clear to see  $\text{MnO}_2$  in a mean thickness of about 20nm were vertically grown on the surface of  $\text{CoFe}_2\text{O}_4$  NSs, favoring for the exposure of more active  $\text{MnO}_2$  site for electrochemical reaction. In addition, there were a lot of pores existed between core-shell NSAs which can shorten the diffusion distance from the external electrolyte to interior surface and improved the utilization rate of electrode material. Such ultrathin feature and porous structure are beneficial to an efficient, reversible faradaic redox reaction and short ionic diffusion path during the charge-discharge process.<sup>46</sup> The components of  $\text{CoFe}_2\text{O}_4$  NSs and  $\text{CoFe}_2\text{O}_4@\text{MnO}_2$  NSAs were confirmed by the EDX spectroscopy (Figure S2a-b). The phase and elements in the final product were investigated by SEM and its corresponding element mapping. Figure 17e demonstrated that uniformly distributed elements of Mn, Fe and Co in the whole investigation region. The EDX data (Figure 17f) of the element mapping revealed that the atomic ratio of Fe/Co was about 2:1, and the co-existence of Mn further confirmed the formation of  $\text{CoFe}_2\text{O}_4@\text{MnO}_2$ .

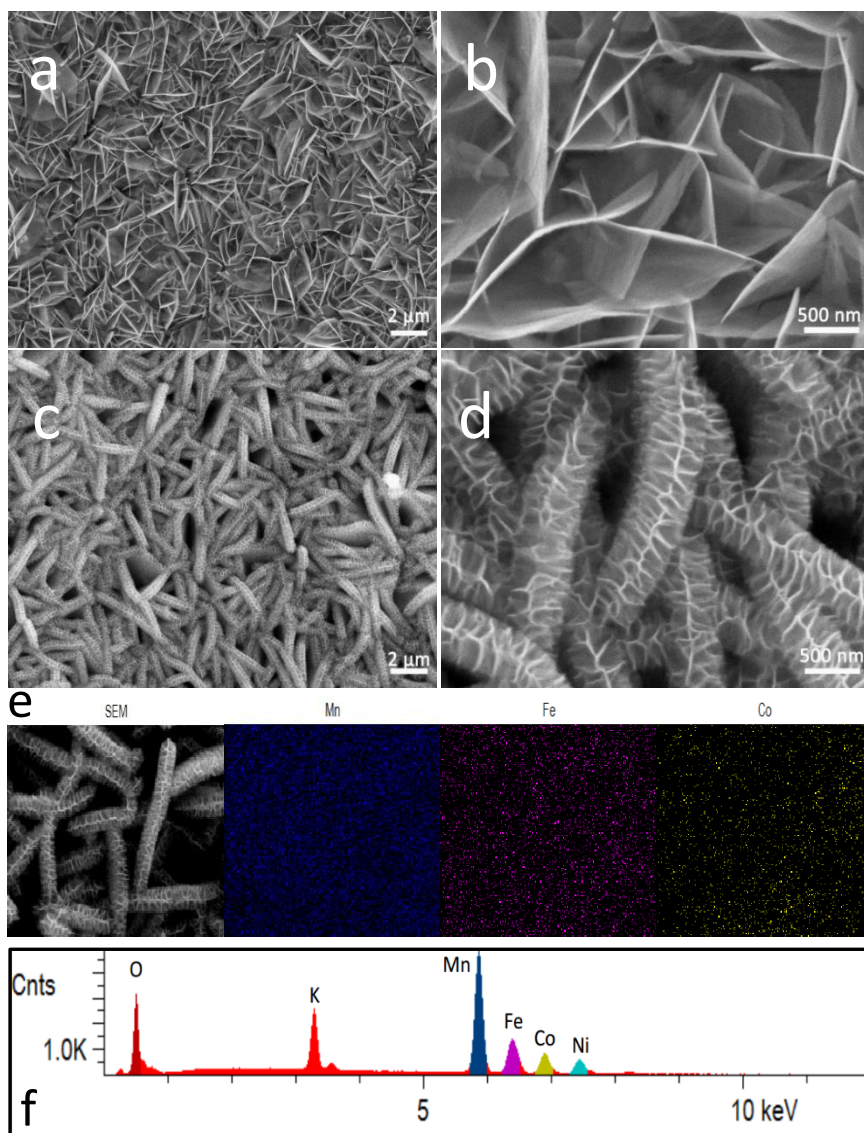


**Figure 17.** (a-b) SEM images of typical  $\text{CoFe}_2\text{O}_4$  nanosheets on Ni foam. (c-d) SEM images of typical  $\text{CoFe}_2\text{O}_4 @ \text{MnO}_2$  core-shell NSAs on Ni foam. (e) SEM image and the corresponding element (Mn, Fe and Co) mapping of the  $\text{CoFe}_2\text{O}_4 @ \text{MnO}_2$  core-shell NSAs. (f) EDX data of  $\text{CoFe}_2\text{O}_4 @ \text{MnO}_2$  core-shell nanosheet arrays obtained from element mapping.

The nanostructures of the  $\text{CoFe}_2\text{O}_4$  NSs and  $\text{CoFe}_2\text{O}_4 @ \text{MnO}_2$  NSAs were further

investigated by TEM. Figure 18a revealed the  $\text{CoFe}_2\text{O}_4$  NSs with a quasi-rectangular shape corresponding to the SEM image. Importantly, the TEM image also revealed the porous texture and ultrathin feature of the  $\text{CoFe}_2\text{O}_4$  NSs. The magnified TEM (Figure 18b) clearly showed the uniform mesopores distribution on  $\text{CoFe}_2\text{O}_4$  NSs, which could likely be caused by the liberation of gases during the decomposition of the precursors. The HRTEM image (Figure 18c) of  $\text{CoFe}_2\text{O}_4$  NSs shows that the lattice spacing was 0.26 nm, measured from the lattice fringe, which corresponded to the (311) plane of  $\text{CoFe}_2\text{O}_4$ . The corresponding SAED pattern (inset of Figure 18b) clearly showed the well-defined rings which could be readily ascribed to the (220), (311), (222) (400) and (440) planes of spinel  $\text{CoFe}_2\text{O}_4$ , respectively. After the growth of  $\text{MnO}_2$  NSs on  $\text{CoFe}_2\text{O}_4$  NSs, the surface of  $\text{CoFe}_2\text{O}_4$  NSs were covered by  $\text{MnO}_2$  NSs. In the Figure 18d, the  $\text{CoFe}_2\text{O}_4@ \text{MnO}_2$  NSAs nanostructure did not show any noticeable separation of  $\text{MnO}_2$ , indicating the adhesion of  $\text{MnO}_2$  NSs to  $\text{CoFe}_2\text{O}_4$  NSs could be really firm. The ultrathin property of  $\text{MnO}_2$  NSs exhibited in Figure 18e was consistent with those in the SEM observation. The freestanding  $\text{MnO}_2$  NSs partly overlapped with each other to form a wrinkled nanostructure. The HRTEM image (Figure 18f) of  $\text{CoFe}_2\text{O}_4@ \text{MnO}_2$  NSAs clearly showed that the lattice fringe spaces of 0.19 nm, corresponding to the (111) planes of the birnessite-type  $\delta\text{-MnO}_2$ . The SAED pattern (inset of Figure 18e) of the nanosheets manifested the polycrystalline feature of  $\delta\text{-MnO}_2$ . In order to further confirm the core-shell nanostructure of  $\text{CoFe}_2\text{O}_4@ \text{MnO}_2$  NSAs, the STEM-EDX mapping of the as fabricated material was performed. Figure 18g shows the EDX mapping analysis of a single  $\text{CoFe}_2\text{O}_4@ \text{MnO}_2$  NSA. The co-existence and similar shapes of Mn, O,

Fe and Co signals verified the successful fabrication of  $\text{CoFe}_2\text{O}_4@\text{MnO}_2$  core-shell NSAs.

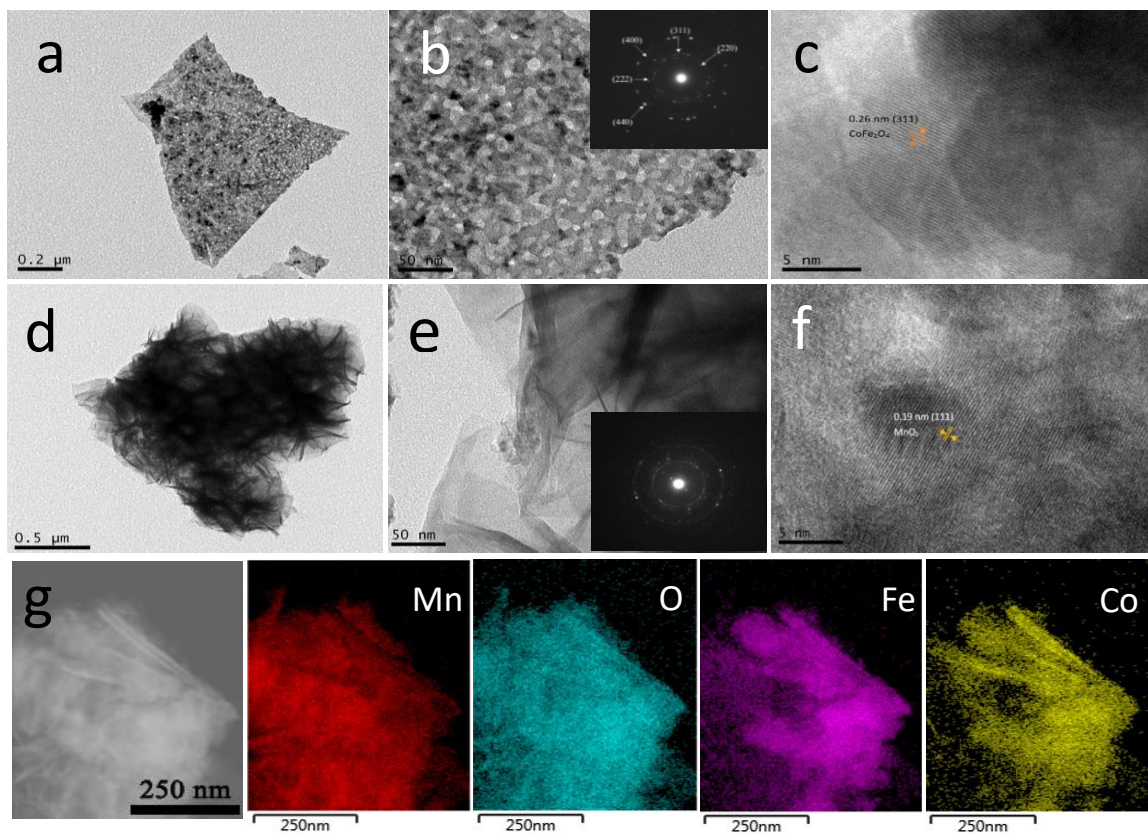


**Figure 18.** TEM images of (a-c)  $\text{CoFe}_2\text{O}_4$  nanosheets and (c-f)  $\text{CoFe}_2\text{O}_4 @ \text{MnO}_2$  NSAs scratched from Ni foam. The insets in Figure b and e are the corresponding SAED patterns of  $\text{CoFe}_2\text{O}_4$  nanosheets and  $\text{CoFe}_2\text{O}_4@\text{MnO}_2$  NSAs, respectively. (g) STEM-EDX mapping of an individual  $\text{CoFe}_2\text{O}_4 @ \text{MnO}_2$  core-shell NSA.

The investigation of elemental chemical state and chemical composition on the surfaces of samples helped the further understandings of its pseudocapacitors mechanism. Figure 19a shows the XPS spectra of Co 2p of  $\text{CoFe}_2\text{O}_4$  NSs in the binding energy between 773 and 813 eV. There were two main peaks corresponding to Co 2p<sub>3/2</sub> and Co 2p<sub>1/2</sub>. The Co 2p<sub>3/2</sub> can be divided into two subpeaks after fitting. The fitting peaks at 779.9 eV and the



satellite peak of 786.7 eV were indexed to  $\text{Co}^{3+}$ , while the fitting peaks at 781.6 eV and 795.8 eV with the satellite peak of 802.9 eV were associated with  $\text{Co}^{2+}$ .<sup>68</sup> The spin-orbit splitting was approximately 15eV, suggesting these peaks were attributed to  $\text{Co } 2p_{3/2}$  and  $\text{Co } 2p_{1/2}$ . Figure 19b elucidated the Fe 2p photoionization region between 703 and 741 eV. The Fe  $2p_{3/2}$  yielded two subpeaks after fitting at 710.2 and 712.1 eV (main peaks,  $\text{Fe}^{3+}$ ) with a “shoulder” satellite peak at 717.4 eV (satellite peaks,  $\text{Fe}^{2+}$ ).<sup>50</sup> The fitting peak of Fe  $2p_{1/2}$  at 724.6 eV was indexed to  $\text{Fe}^{3+}$ , while the satellite peak at 733.4 eV was corresponded to  $\text{Fe}^{2+}$ .<sup>37</sup> The XPS characterization clearly revealed the as-prepared  $\text{CoFe}_2\text{O}_4$  NSs belonged to the mixed valence compounds, which contained  $\text{Co}^{3+}$ ,  $\text{Co}^{2+}$ ,  $\text{Fe}^{3+}$ , and  $\text{Fe}^{2+}$ . The XPS spectra of Mn 2p and O 1s of the deposited  $\text{MnO}_2$  are shown in Figure 19c-d, respectively. As shown in Figure 19c, the Mn  $2p_{3/2}$  and Mn  $2p_{1/2}$  spin-orbit peaks were located at 642.3 and 654.2 eV, which were in good agreement with the typical  $\text{MnO}_2$ , implying its +4 oxidation state.<sup>69</sup> By using the fitting method, the O 1s spectra was well-fitted to be divided into two fitting peaks, representing two kinds of oxygen states named as O1 and O2. The O1 peak at a binding energy of 529.8 eV can be assigned to a typical metal-oxygen bond. Besides, the fitting O2 peak at a binding energy of 531.8 eV was caused by the physic- or chemisorbed water at the surface.<sup>70</sup>

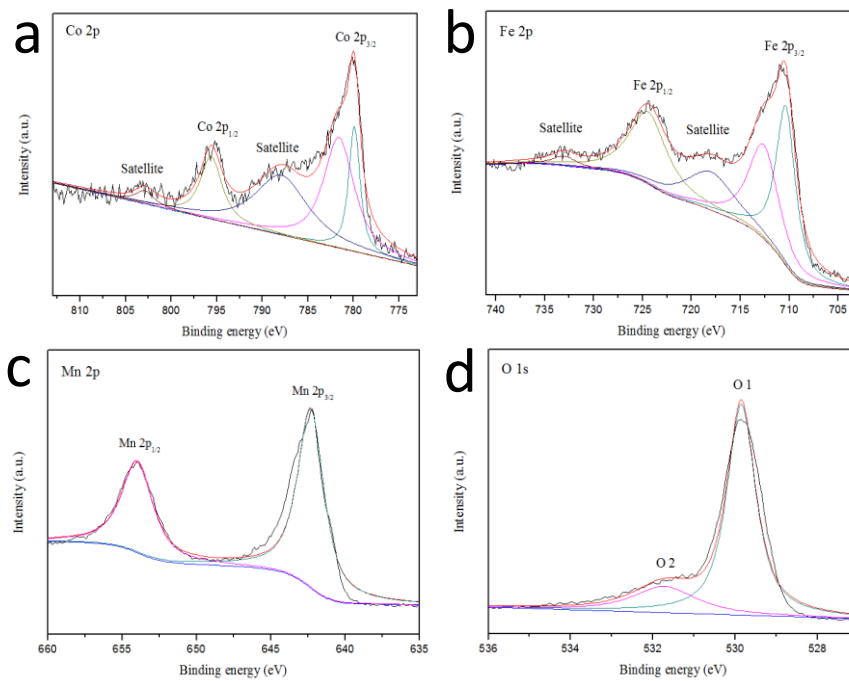


**Figure 19.** XPS spectra of the (a) Co 2p and (b) Fe 2p regions of CoFe<sub>2</sub>O<sub>4</sub> nanosheets. XPS spectra of the (c) Mn 2p and (d) O 1s of CoFe<sub>2</sub>O<sub>4</sub> @ MnO<sub>2</sub> core-shell NSAs.

### 3.3.2 Electrochemical properties of $\text{CoFe}_2\text{O}_4@\text{MnO}_2$ electrode

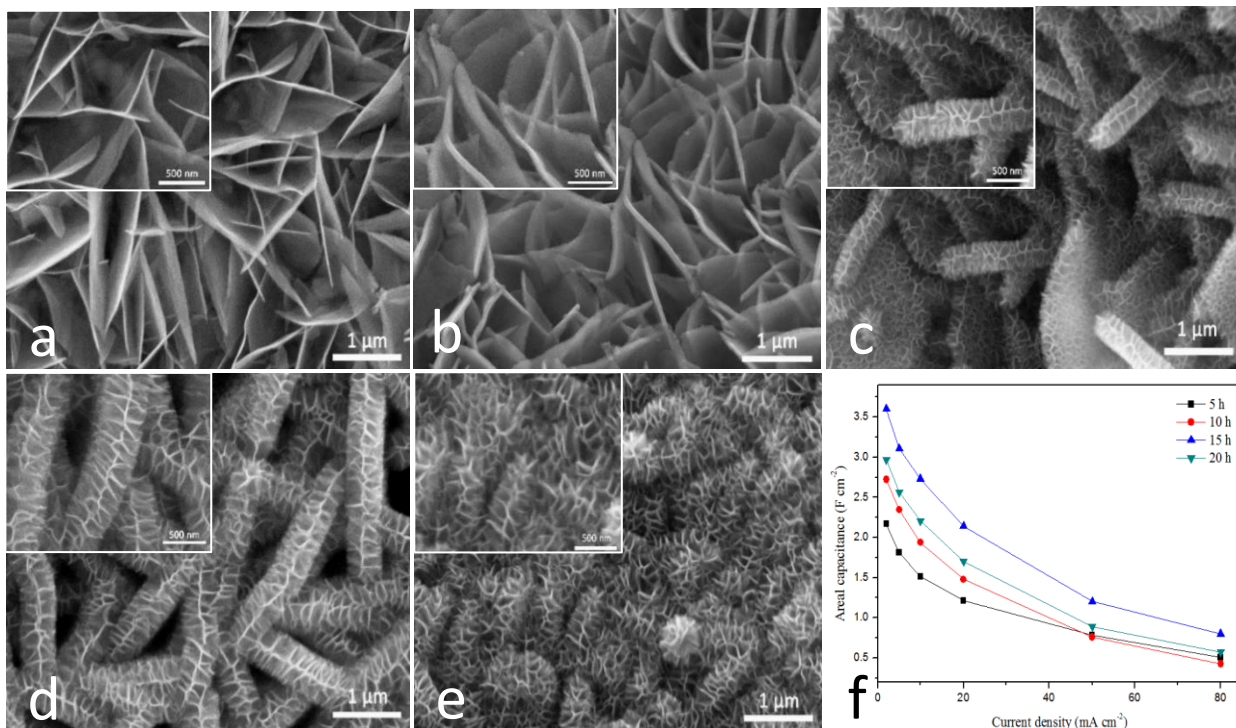


**Figure 20.** SEM images of the  $\text{CoFe}_2\text{O}_4 @ \text{MnO}_2$  core-shell NSAs obtained at different reaction times: (a) 0h; (b) 5h; (c) 10h; (d) 15h; and (e) 20h. Insets show the high-magnification SEM images. (f) Areal capacitances of  $\text{CoFe}_2\text{O}_4 @ \text{MnO}_2$  core-shell NSAs electrodes obtained at different reaction times and at different current densities.

Composite engineering of materials is an important strategy to form high-performance electrode materials for supercapacitors. However, it is worth to point out the adverse effects may also arise during the process of fabricating novel composites. There should be an optimal structure and constituent among the composition of individual substances.<sup>17</sup> In order to optimize performance of  $\text{CoFe}_2\text{O}_4@\text{MnO}_2$  core-shell NSAs, the thickness of  $\text{CoFe}_2\text{O}_4@\text{MnO}_2$  NSAs was tailored by adjusting the hydrothermal reaction time. Figure

20 shows the SEM images of  $\text{CoFe}_2\text{O}_4@\text{MnO}_2$  NSAs obtained at different reaction times. At the first 5h (Figure 20b), the average thickness of  $\text{CoFe}_2\text{O}_4$  NSs changes from 25 nm to 70nm, but that of  $\text{MnO}_2$  nanosheets were not obvious. Interestingly, the tiny “buds” began to grow on the surface of  $\text{CoFe}_2\text{O}_4$  NSs according to the high-magnification SEM image. When the reaction time was prolonged to 10 h, the thickness of  $\text{CoFe}_2\text{O}_4@\text{MnO}_2$  NSs increased to about 250 nm which was much thicker than that of the 5h test. This enlighten that the tiny “buds” may guide the growth of ultrathin  $\text{MnO}_2$  NSs. With the reaction time was prolonged to 20h, the space between core-shell NSAs seemed to be completely occupied by  $\text{MnO}_2$  NSs. Smaller pores resulted from thicker covers may restrict the access of electrolyte during charging-discharging, implying an adverse effect for prolonged retention time. This was confirmed in the electrochemical performance of  $\text{CoFe}_2\text{O}_4@\text{MnO}_2$  NSAs with different reaction times in Figure 21a, showing the CV curves of these electrodes at  $10 \text{ mV s}^{-1}$ . The largest area under the blue curve indicated that  $\text{CoFe}_2\text{O}_4@\text{MnO}_2$  NSAs for the retention time at 15h was in the highest capacitance. The GCD tests further claimed that the specific capacitance increased initially and then decreased with the increase of the reaction time as shown in Figure 5f. The GCD curves of 5h, 10h and 20h at different current densities are shown in Figure 21b-d.

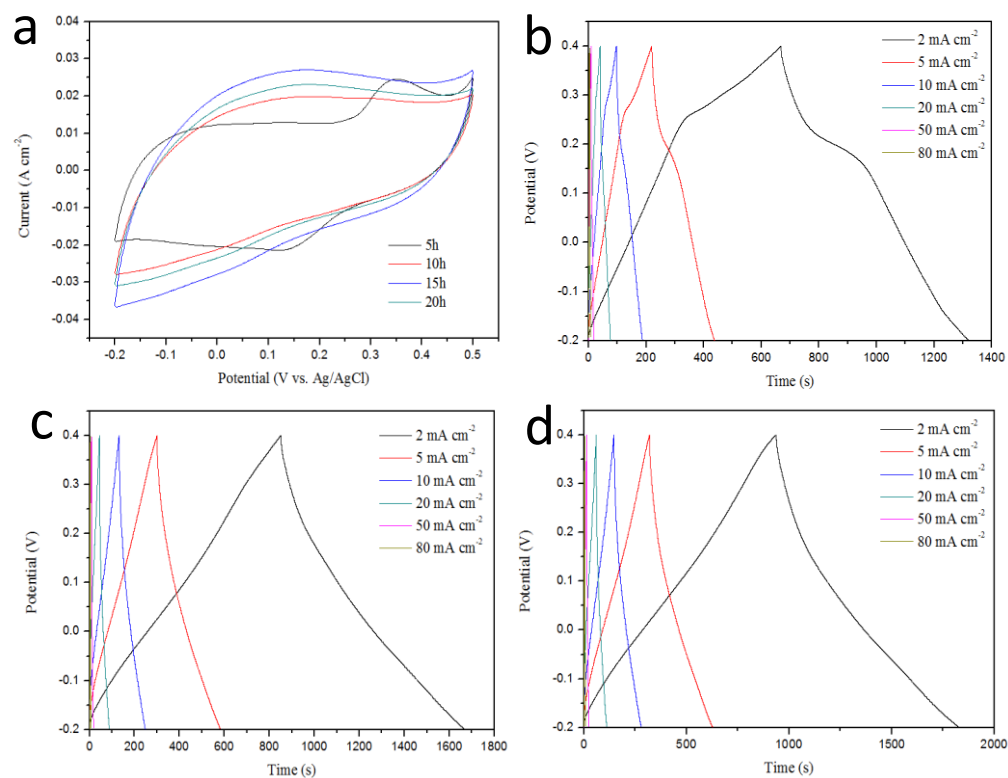


**Figure 21.** (a) CV curves of CoFe<sub>2</sub>O<sub>4</sub> @ MnO<sub>2</sub> core-shell arrays fabricated with different reaction times at a scan rate of 10 mV s<sup>-1</sup>. (b-d) Galvanostatic charge-discharge of the CoFe<sub>2</sub>O<sub>4</sub> @ MnO<sub>2</sub> core-shell arrays fabricated with different reaction times at various current densities. (b) 5h; (c) 10h; (d) 20h.

The electrochemical performance of as-fabricated samples were first conducted in a three-electrode electrochemical system by testing them as working electrodes for supercapacitors. Figure 22a shows CV curves of CoFe<sub>2</sub>O<sub>4</sub>@MnO<sub>2</sub> NSAs at various scan rates ranging from 5 to 80 mV s<sup>-1</sup>. With the increasing of scan rates, all CV curves presented a similar shape which deviated from rectangular-like character, demonstrating the

pseudocapacitive behavior of the electrode and the excellent interlayer charge transfer and good reversibility features.<sup>71</sup> Figure 22b shows the typically GCD curves of CoFe<sub>2</sub>O<sub>4</sub>@MnO<sub>2</sub> NSAs at different current densities. The linear slopes and symmetry triangular shapes of the CV curves indicate reversible charge-discharge behavior. The specific area capacitances of the CoFe<sub>2</sub>O<sub>4</sub>@MnO<sub>2</sub> NSAs electrode were calculated to be 3.59, 3.11, 2.73, 2.14, 1.20, 0.81 F cm<sup>-2</sup> at current densities of 2, 5, 10, 20, 50, 80 mA cm<sup>-2</sup>, respectively, according to equation (12) (The corresponding specific capacitances were 1994.4, 1727.8, 1516.7, 1188.9, 666.7 and 450 F g<sup>-1</sup>). In order to investigate the enhanced performance of unique CoFe<sub>2</sub>O<sub>4</sub>@MnO<sub>2</sub> core-shell NSAs, we compared the electrochemical properties of CoFe<sub>2</sub>O<sub>4</sub> NSs, MnO<sub>2</sub> NSs and CoFe<sub>2</sub>O<sub>4</sub>@MnO<sub>2</sub> core-shell NSAs. Figure 20 c and d present the CV curves at 20 mV s<sup>-1</sup> and GCD curve at 5 mA cm<sup>-2</sup> of aforementioned three samples, respectively. The CV shapes of the individual components NSs indicated the pseudocapacitive property of CoFe<sub>2</sub>O<sub>4</sub> NSs and MnO<sub>2</sub> which based on the Faradic redox reaction in their energy storage processes. However, The CV shape of CoFe<sub>2</sub>O<sub>4</sub>@MnO<sub>2</sub> NSAs was different from those of CoFe<sub>2</sub>O<sub>4</sub> and MnO<sub>2</sub> and its area was much larger than those of both individual substances, indicating the electrochemical properties of CoFe<sub>2</sub>O<sub>4</sub> and MnO<sub>2</sub> can be changed by the formation of CoFe<sub>2</sub>O<sub>4</sub>@MnO<sub>2</sub> NSAs. The absence of obvious redox peak in CoFe<sub>2</sub>O<sub>4</sub>@MnO<sub>2</sub> NSAs can be attributed to the change of morphologies and sizes after the deposition of MnO<sub>2</sub> NSs on the CoFe<sub>2</sub>O<sub>4</sub> NSs.<sup>72</sup> A comparison of the GCD curves at 5 mA cm<sup>-2</sup> is illustrated in Figure 20d. Obviously, the charge-discharge time of CoFe<sub>2</sub>O<sub>4</sub>@MnO<sub>2</sub> NSAs was much

longer than those of CoFe<sub>2</sub>O<sub>4</sub> and MnO<sub>2</sub> NSs electrodes which indicated a much improved capacitance. It can also be seen that the charge-discharge curves of all samples were almost symmetric, suggesting their excellent columbic efficiencies. In order to evaluate the rate capability of CoFe<sub>2</sub>O<sub>4</sub>@MnO<sub>2</sub> NSAs electrode, we compared the specific area capacitance of all samples at different current densities. When the current density increased to 20 mA cm<sup>-2</sup>, which was 10-fold of the initial one, the capacitance CoFe<sub>2</sub>O<sub>4</sub>@MnO<sub>2</sub> NSAs still remained 2.14 F cm<sup>-2</sup> (Figure 22e). The capacitance retention was about 60% of the original value which was higher than 50% for CoFe<sub>2</sub>O<sub>4</sub> NSs and 43.8% for MnO<sub>2</sub> NSs at 20 mA cm<sup>-2</sup>, showing the remarkable rate capability of the CoFe<sub>2</sub>O<sub>4</sub>@MnO<sub>2</sub> NSAs electrode. In addition, we can see all the specific area capacitances of CoFe<sub>2</sub>O<sub>4</sub>@MnO<sub>2</sub> NSAs at different current densities were much higher than the sum of CoFe<sub>2</sub>O<sub>4</sub> and MnO<sub>2</sub> NSs which further manifest the formation of core-shell nanostructure was an efficient strategy to enhance the performance of electrode materials.

Electrochemical impedance spectroscopy (EIS) was carried out to study the ion-transport behavior of CoFe<sub>2</sub>O<sub>4</sub> NSs, MnO<sub>2</sub> NSs and CoFe<sub>2</sub>O<sub>4</sub>@MnO<sub>2</sub> NSAs electrodes. As shown in Figure 20f, all samples presented similar shapes in a semicircle at a higher frequency region and a straight line at lower frequency. At the high frequency, the intersection of the curve on the real axis represents the series resistance ( $R_s$ , representing the inherent active material resistance, electrolyte resistance and contact resistance) and the semicircle diameter represents the Faradaic charge transfer resistance ( $R_{ct}$ ).<sup>73</sup>  $R_s$  values of 0.63  $\Omega$ , 0.53  $\Omega$  and 0.78  $\Omega$  can be calculated from EIS curves of the CoFe<sub>2</sub>O<sub>4</sub>@MnO<sub>2</sub>

NSAs,  $\text{CoFe}_2\text{O}_4$  NSs and  $\text{MnO}_2$  NSs electrodes, respectively. The increased  $R_s$  should be attributed to the poor conductivity of  $\text{MnO}_2$ . Impressively, the  $\text{CoFe}_2\text{O}_4@\text{MnO}_2$  NSAs exhibited a smaller semicircle in EIS than  $\text{MnO}_2$  NSs electrodes, indicating the faster ion insertion/extraction during electrochemical reactions. The near linear EIS plots of these samples at the low frequency are the characteristic of Warburg impedance (W, reflecting the resistance behavior caused by the diffusion of  $\text{OH}^-$  within electrode materials during redox reaction).<sup>74</sup> The more perpendicular line leaning to the real axis of  $\text{CoFe}_2\text{O}_4@\text{MnO}_2$  NSAs electrode, suggesting more facile electrolyte diffusion to the surface and the ideal capacitive behavior.



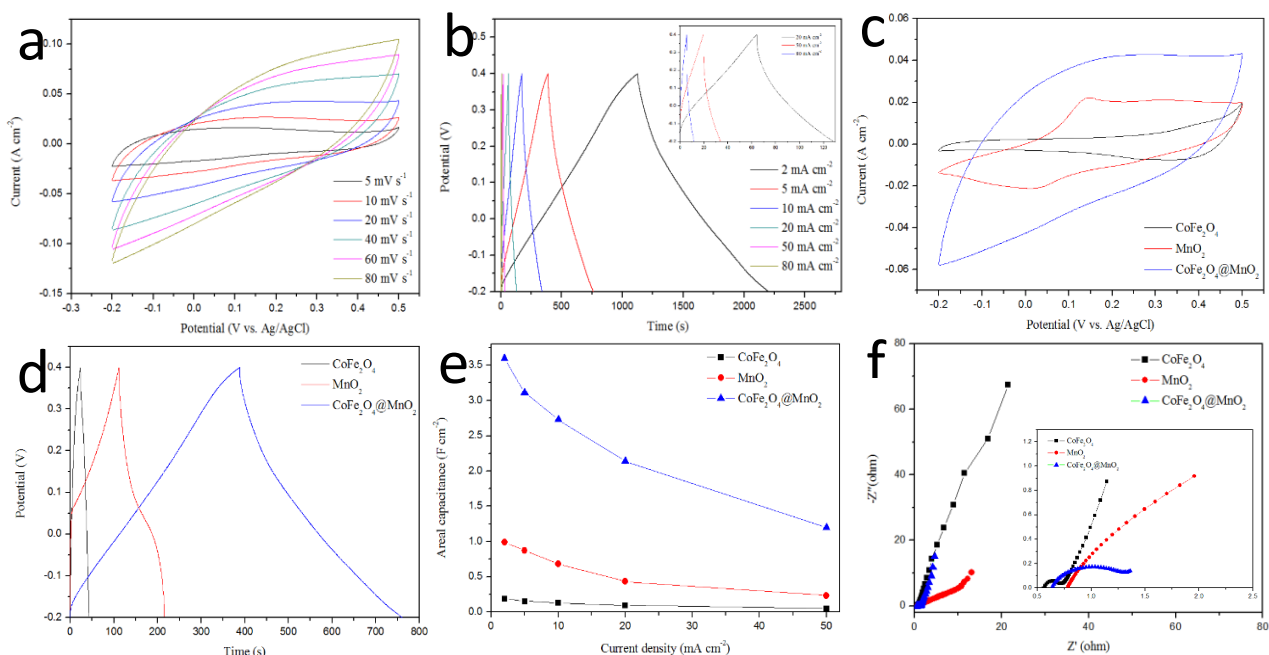


**Figure 22.** (a) CV curves of  $\text{CoFe}_2\text{O}_4 @ \text{MnO}_2$  core-shell NSAs at different scan rates. (b) Galvanostatic charge-discharge of the  $\text{CoFe}_2\text{O}_4 @ \text{MnO}_2$  core-shell NSAs at various current densities. (c-f) Comparing bare  $\text{CoFe}_2\text{O}_4$  electrode (black), bare  $\text{MnO}_2$  electrode (red) and optimal  $\text{CoFe}_2\text{O}_4 @ \text{MnO}_2$  electrode (blue), all grown on Ni foam: (c) CV curves at  $20 \text{ mV s}^{-1}$ , (d) galvanostatic charge-discharge at  $5 \text{ mA cm}^{-2}$ , (e) areal specific capacitances versus discharge current density, and (f) EIS curves (inset shows the EIS curves at high frequency).

### 3.3.3 Electrochemical performance of CoFe<sub>2</sub>O<sub>4</sub>@MnO<sub>2</sub>//AC asymmetric supercapacitor

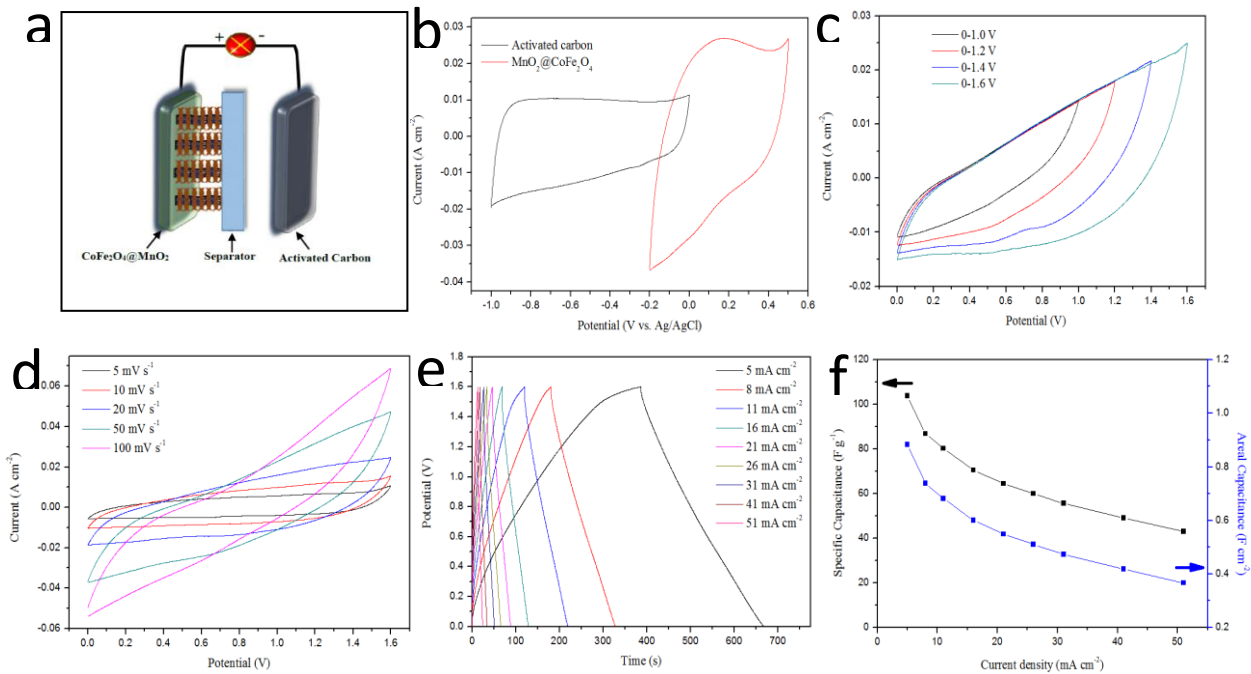


**Figure 23.** (a) Schematic illustration of the as-fabricated CoFe<sub>2</sub>O<sub>4</sub> @ MnO<sub>2</sub>//AC-ASC device. (b) Comparative CV curves of the activated carbon electrode and CoFe<sub>2</sub>O<sub>4</sub> @ MnO<sub>2</sub> electrode at 10 mV s<sup>-1</sup>. (c) CV curves at different cell voltages at a scan rate of 20 mV s<sup>-1</sup> and (d) different scan rates for CoFe<sub>2</sub>O<sub>4</sub> @ MnO<sub>2</sub>// AC-ASC device. (e) Galvanostatic charge-discharge curves at different current densities. (f) Specific capacitances of the CoFe<sub>2</sub>O<sub>4</sub> @ MnO<sub>2</sub>// AC-ASC device at different current densities.

To further evaluate the possibility of the as-fabricated CoFe<sub>2</sub>O<sub>4</sub>@MnO<sub>2</sub> core-shell NSAs for practical application, an asymmetric supercapacitor was assembled using CoFe<sub>2</sub>O<sub>4</sub>@MnO<sub>2</sub> NSAs electrode as the anode and AC as the cathode. Figure 23a shows a schematic illusion of this ASC. Figure 23b shows CV curves of both AC and

CoFe<sub>2</sub>O<sub>4</sub>@MnO<sub>2</sub> NSAs electrodes at a scan rate of 10 mV s<sup>-1</sup>. The AC electrode revealed excellent electrochemical double layer capacitance performance between -1.0 and 0.0 V in view of the close-to-rectangular CV curve (black curve). In order to determine the working potential window of the full cell, we carried out the CV tests of the ASCs within different cell voltages varying from 0-1 V to 0-1.6 V (Figure 23c). The stable potential window for the assembled ASC can be extended to 1.6 V where the CV curve still maintained a rectangle-like shape. Therefore, the working potential window of 0-1.6 V was chosen to investigate the electrochemical performance of CoFe<sub>2</sub>O<sub>4</sub>@MnO<sub>2</sub> // AC ASC. With the increase of scan rates in CV tests, the CV profiles (Figure 23d) of the ASC still remained the rectangular-like shape without any redox peaks, indicating good charge-discharge property and rate capability of the ASC device. Figure 23e exhibits the GCD curves of the ASC device in a voltage window of 0-1.6 V at different current densities. The charge curves of the ASC device were almost symmetric to its corresponding discharge counterpart, confirming the excellent capacitive character of CoFe<sub>2</sub>O<sub>4</sub>@MnO<sub>2</sub> // AC ASC. The calculation of the specific capacitances of the ASC was based on the GCD tests. Figure 23f presents the mass and areal specific capacitances of CoFe<sub>2</sub>O<sub>4</sub>@MnO<sub>2</sub> //AC ASC at different current densities. The specific capacitance of the full cell can achieve 103.86 F g<sup>-1</sup> (0.883 F cm<sup>-2</sup>) at 5 mA cm<sup>-2</sup>, and still retained 43.12 F g<sup>-1</sup> (0.367 F cm<sup>-2</sup>) at a high current density of 51 mA cm<sup>-2</sup>.

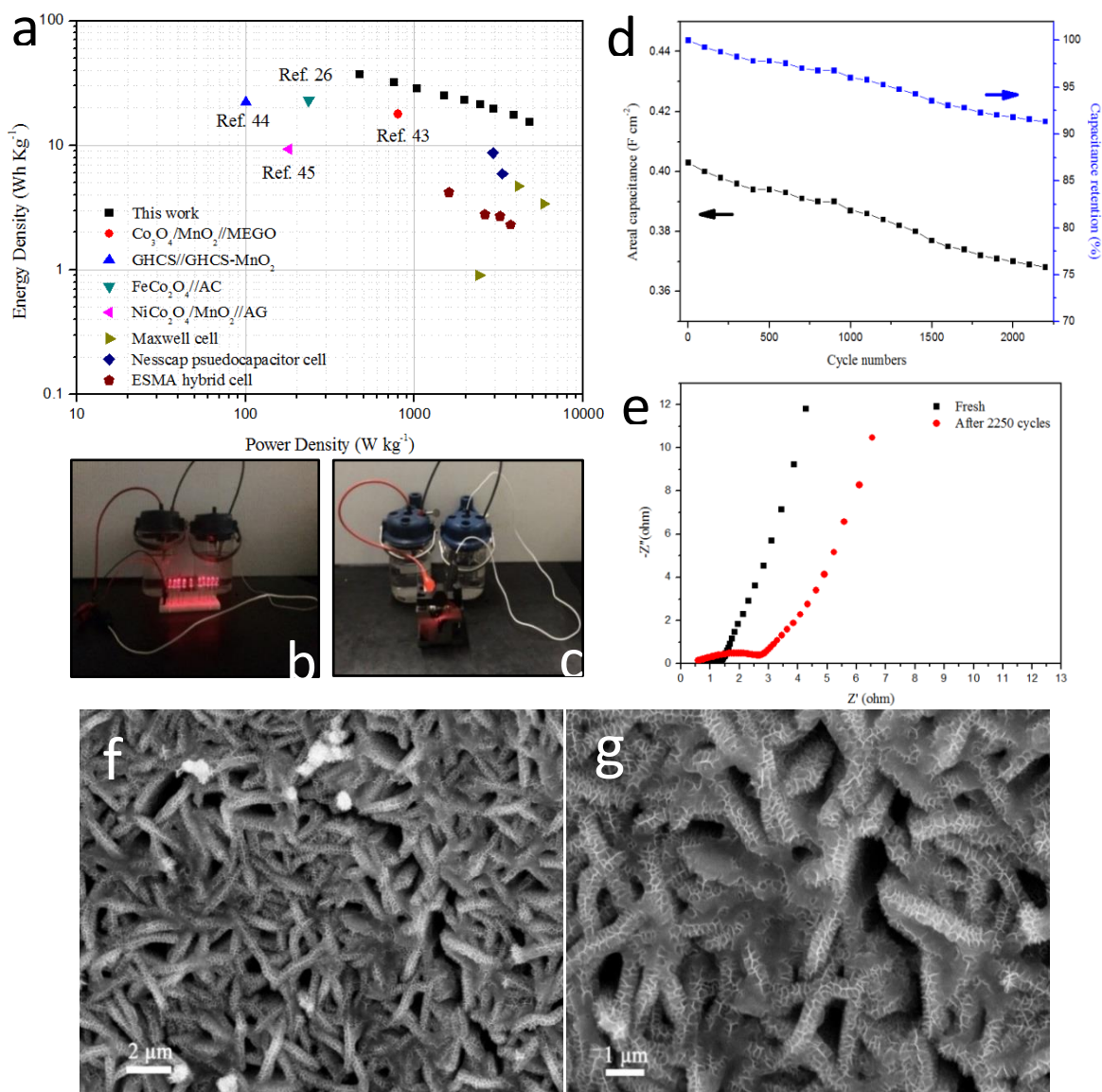


**Figure 24.** (a) Ragone plot of the  $\text{CoFe}_2\text{O}_4 @ \text{MnO}_2//\text{AC}$ -ASC device. The values reported for others devices and some commercial supercapacitors are given here for a comparison. (b) A digital image showing the two ASC devices in series can light up ten red LED indicators. (c) A rotating motor derived by two supercapacitors in series. (d) Cycling stability of  $\text{CoFe}_2\text{O}_4 @ \text{MnO}_2//\text{AC}$ -ASC device at a current density of  $41 \text{ mA cm}^{-2}$ . (e) EIS curves of the fresh  $\text{CoFe}_2\text{O}_4 @ \text{MnO}_2$  electrode and after 2250th cycle. (f-g) SEM images of  $\text{CoFe}_2\text{O}_4 @ \text{MnO}_2$  NSAs after cycling test.

Energy density and power density are two critical parameters to evaluate the electrochemical performance of supercapacitors. Figure 24a shows the Ragone plot of the  $\text{CoFe}_2\text{O}_4@\text{MnO}_2//\text{AC}$  ASC based on GCD tests. The maximum energy density of the ASC was  $37 \text{ W h kg}^{-1}$  at a power density of  $470 \text{ W kg}^{-1}$  based on total mass of active materials. The energy density gradually decreased to  $15.3 \text{ W h kg}^{-1}$  with the increase of power density from  $470 \text{ W kg}^{-1}$  to  $4800 \text{ W kg}^{-1}$ . The energy densities and power densities of  $\text{CoFe}_2\text{O}_4@\text{MnO}_2//\text{AC}$  ASC were compared to those of reported hybrid supercapacitors similarly based on  $\text{MnO}_2$  and transition metal oxides (Figure 24a). Obviously, the energy density in this study was higher than that of  $\text{Co}_3\text{O}_4/\text{MnO}_2//\text{MEGO}$  ( $17.7 \text{ W h kg}^{-1}$ ),<sup>75</sup>  $\text{GHCS}/\text{GHCS-MnO}_2$  ( $22.1 \text{ W h kg}^{-1}$ ),<sup>76</sup>  $\text{FeCo}_2\text{O}_4//\text{AC}$  ( $23 \text{ W h kg}^{-1}$ )<sup>18</sup> and  $\text{NiCo}_2\text{O}_4/\text{MnO}_2//\text{AG}$  ( $9.4 \text{ W h kg}^{-1}$ ).<sup>77</sup> Significantly, the highest energy density of the  $\text{CoFe}_2\text{O}_4@\text{MnO}_2//\text{AC}$  ASC exceeded those of most of the commercial cells such as Maxwell, Nesscap and ESMA and their power densities are comparable. Two  $\text{CoFe}_2\text{O}_4@\text{MnO}_2//\text{AC}$  ASC devices were further assembled in series. After charged for 20s to about 3.2 V, the connected devices efficiently powered a 10-LEDs (red, 1.8 V, 20mA for each) (Figure 24b). More impressively, the device drove a motor (2.8V) more than 30 sec without the loss of rotational speed (Figure 24c). A long-term cycle stability of the  $\text{CoFe}_2\text{O}_4@\text{MnO}_2//\text{AC}$  ASC was tested by repeating GCD tests at a high current density of  $41 \text{ mA cm}^{-2}$  for 2250 cycles. As shown in Figure 24d, the specific capacitance of  $\text{CoFe}_2\text{O}_4@\text{MnO}_2//\text{AC}$  ASC still remained 91.5% of its initial capacitance after cycling test. The EIS spectra of  $\text{CoFe}_2\text{O}_4@\text{MnO}_2$  NSAs electrode after cycling test was recorded in

order to investigate the change of interfacial electrochemical behaviors of the electrode after cycling test. As shown in Figure 24e, the EIS spectra showed similar curve shape except for the change of  $R_{ct}$ . Based on this result, the conclusion was drawn that the decrease of capacitance after long-term cycle stability test was likely attributed to the increase of Faradaic charge transfer resistance. Figure S8 shows the SEM image of  $\text{CoFe}_2\text{O}_4@ \text{MnO}_2$  core-shell NSAs after 2250 cycling tests. The morphology of  $\text{CoFe}_2\text{O}_4@ \text{MnO}_2$  still maintained the core-shell nanosheet arrays and almost the same as that before cycling test (Figure S8a) except for a small collapse of vertically aligned  $\text{MnO}_2$  nanosheets (Figure 24f-g), which further indicated its highly mechanical stability.

The high capacitance and excellent cycling stability of  $\text{CoFe}_2\text{O}_4@ \text{MnO}_2$  NSAs electrode can be attributed to the hierarchical core-shell nanostructure. The unique core-shell nanostructure has many apparent advantages as follows: (1) The mesoporous and highly conductive  $\text{CoFe}_2\text{O}_4$  nanosheets grown directly on the Ni foam can provide an electron “superhighway” for charge storage and delivery, which neutralized the intrinsic poor conductivity of  $\text{MnO}_2$ . (2) Ultrathin  $\text{MnO}_2$  nanosheets supported on  $\text{CoFe}_2\text{O}_4$  nanosheets provided a large specific area facilitating a better electrode/electrolyte contact and an increased electroactive sites for redox reaction compared to the individual  $\text{CoFe}_2\text{O}_4$  and  $\text{MnO}_2$  nanosheets. (3) Both of the  $\text{CoFe}_2\text{O}_4$  and  $\text{MnO}_2$  were potential pseudocapacitive electrode materials, hence jointly contributed to the total capacitance of  $\text{CoFe}_2\text{O}_4@ \text{MnO}_2$  NSAs. (4) The good mechanical adhesion between  $\text{CoFe}_2\text{O}_4$  and  $\text{MnO}_2$  and electrical connection of the electrode materials to the Ni foam without any binder or conductive

agents enhanced the long-term performance and improved the utilization of the hybrid electrode.

### 3.4 Controlled synthesis of MnO<sub>2</sub> nanosheets vertically covered FeCo<sub>2</sub>O<sub>4</sub> nanosheets as binder-free electrode durable asymmetric supercapacitor

#### 3.4.1 Material Characterization

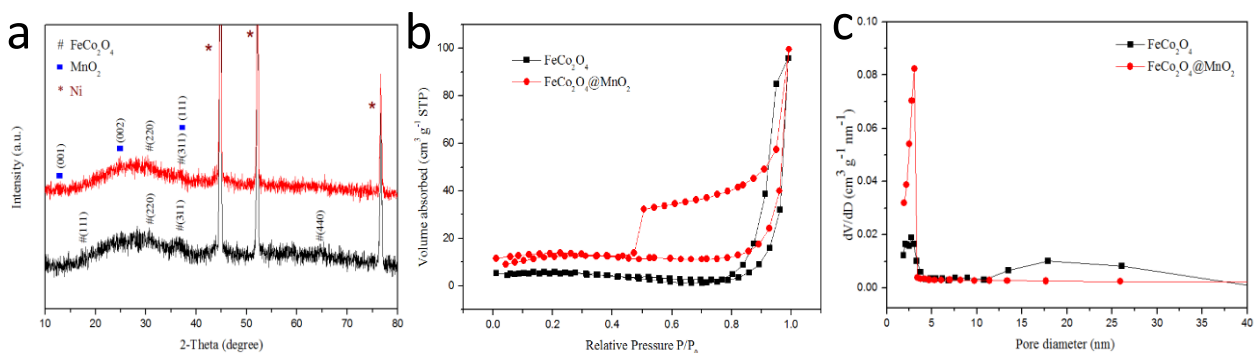


**Figure 25.** (a) XRD patterns of FeCo<sub>2</sub>O<sub>4</sub> nanosheets on the Ni foam before (black curve) and after the growth of MnO<sub>2</sub> (red curve). (b) The nitrogen adsorption-desorption isotherms and (c) the corresponding BJH pore-size distribution of FeCo<sub>2</sub>O<sub>4</sub> and FeCo<sub>2</sub>O<sub>4</sub>@MnO<sub>2</sub> NSAs.

XRD was applied to analysis the crystal structures of the as-prepared samples. In the XRD pattern of FeCo<sub>2</sub>O<sub>4</sub> (black curve in Figure 25a), the diffraction peaks at 44.5°, 52.1° and 76.5° could be assigned to Ni foam (JCPDF card No. 04-0850), the remaining peaks at  $2\theta = 17.3^\circ, 30.7^\circ, 37.0^\circ$  and  $64.5^\circ$  corresponded to the (111), (220), (311), and (440). The diffraction peaks in the FeCo<sub>2</sub>O<sub>4</sub> XRD pattern was indexed to spinel FeCo<sub>2</sub>O<sub>4</sub> phase with the space group of *Fd3m*, which was in good agreement with the previous investigations<sup>78-79</sup>. As for the deposition of MnO<sub>2</sub> on FeCo<sub>2</sub>O<sub>4</sub> nanosheets, some of the



FeCo<sub>2</sub>O<sub>4</sub> diffraction peaks largely diminished except for the reflection of (220), (311), which should be attributed to the ultrathin FeCo<sub>2</sub>O<sub>4</sub> nanosheets covered by relatively thick MnO<sub>2</sub> layer. The new peaks at 12.3°, 25.0° and 37.0° were related to (001), (002) and (111) reflections of MnO<sub>2</sub> (JCPDS card No: 86-0666)<sup>80</sup>. The XRD results confirmed the co-existence of MnO<sub>2</sub> and FeCo<sub>2</sub>O<sub>4</sub> on the Ni foam. The mesoporous properties of the as-fabricated samples were investigated by the surface area analysis and the pore size distribution analysis. As shown in Figure 25b, the N<sub>2</sub> adsorption-desorption isotherms of the FeCo<sub>2</sub>O<sub>4</sub> and FeCo<sub>2</sub>O<sub>4</sub>@MnO<sub>2</sub> NSAs revealed distinct hysteresis loops in the range of 0.8-1.0 P/P<sub>0</sub> and 0.5-1.0 P/P<sub>0</sub>, respectively, indicating the mesoporous properties of FeCo<sub>2</sub>O<sub>4</sub> and FeCo<sub>2</sub>O<sub>4</sub>@MnO<sub>2</sub> NSAs. The presence of the hysteresis loop at higher relative pressures in FeCo<sub>2</sub>O<sub>4</sub> originated from the larger mesopores size.<sup>81</sup> The Brunauer-Emmett-Teller (BET) surface area values of FeCo<sub>2</sub>O<sub>4</sub> and FeCo<sub>2</sub>O<sub>4</sub>@MnO<sub>2</sub> NSAs were calculated to be about 45 and 104 m<sup>2</sup> g<sup>-1</sup>, respectively. The pore-size distribution of the samples is shown in Figure 25c. The FeCo<sub>2</sub>O<sub>4</sub>@MnO<sub>2</sub> NSAs exhibited a narrow pore-size distribution at about 3 nm while the FeCo<sub>2</sub>O<sub>4</sub> nanosheets manifested a sharp peak at 3 nm and wide peaks at 13.4 and 25.9 nm, which were in agreement with the conclusion obtained from the N<sub>2</sub> adsorption-desorption isotherms. The change of pore-size distribution can be attributed to the reconstruction of the composite by the deposited MnO<sub>2</sub> nanosheets on FeCo<sub>2</sub>O<sub>4</sub> nanosheets.

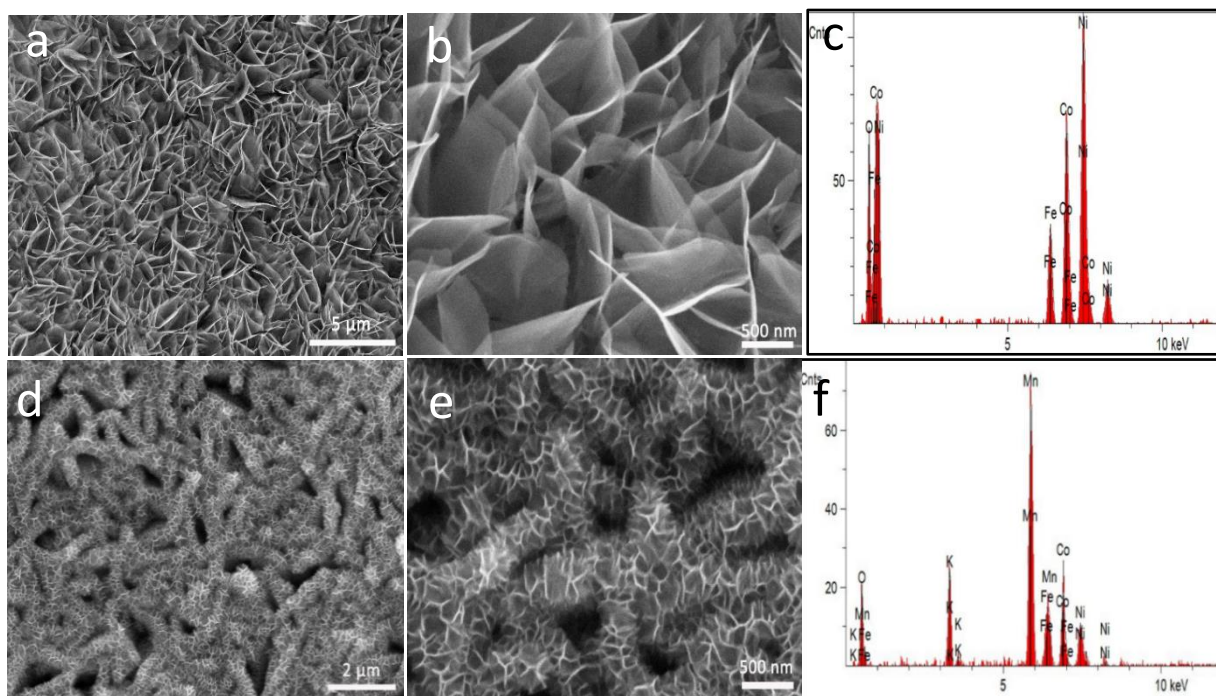


**Figure 26.** (a-b) SEM images of typical  $\text{FeCo}_2\text{O}_4$  nanosheets on Ni foam. (d-e) SEM images of typical  $\text{FeCo}_2\text{O}_4@MnO_2$  NSAs on Ni foam. EDX analysis of (c)  $\text{FeCo}_2\text{O}_4$  nanosheets on the Ni foam and (f)  $\text{FeCo}_2\text{O}_4@MnO_2$  NSA on the Ni foam.

The morphologies and nanostructures of  $\text{FeCo}_2\text{O}_4$  nanosheets and  $\text{FeCo}_2\text{O}_4@MnO_2$  NSAs on Ni foams were investigated by SEM in Figure 26. It revealed that  $\text{FeCo}_2\text{O}_4$  nanosheets vertically and densely grown on Ni foam. The vertically aligned  $\text{FeCo}_2\text{O}_4$  nanosheets with an average thickness of 10 nm interconnected with each other to form a wall-like structure (Figure 26a-b). Remarkably, the smooth surface of ultrathin  $\text{FeCo}_2\text{O}_4$  nanosheets and the space between them provided a favorable substrate for the growth of  $MnO_2$ . Figure 2d-e show the typical morphology of  $\text{FeCo}_2\text{O}_4@MnO_2$ . The framework of

FeCo<sub>2</sub>O<sub>4</sub> nanosheets was not deteriorated during the high temperature hydrothermal MnO<sub>2</sub> growth condition, indicating the excellent mechanical stability between FeCo<sub>2</sub>O<sub>4</sub> nanosheets and the Ni foam. It's interesting that MnO<sub>2</sub> nanosheets, in a thickness about 20 nm, were vertically grown on the FeCo<sub>2</sub>O<sub>4</sub> nanosheets rather than face-to-face. MnO<sub>2</sub> nanosheets were also interconnected with each other, forming a highly porous nanoarchitecture for further contacting and diffusion of electrolytes. This hierarchical FeCo<sub>2</sub>O<sub>4</sub>@MnO<sub>2</sub> NSAs led a balance of the enlarged surface area of the active capacitive materials (MnO<sub>2</sub>) and a smaller resistance of ion diffusion. The components of FeCo<sub>2</sub>O<sub>4</sub> nanosheets and FeCo<sub>2</sub>O<sub>4</sub>@MnO<sub>2</sub> NSAs were confirmed by the EDX spectroscopy (Figure 26c and f). The atomic ratio of Fe/Co of both FeCo<sub>2</sub>O<sub>4</sub> nanosheets and FeCo<sub>2</sub>O<sub>4</sub>@MnO<sub>2</sub> NSAs were approximately 1:2 according to EDX data, confirming the formation of FeCo<sub>2</sub>O<sub>4</sub>. The existence of Mn element in Figure 26f also manifested the formation of FeCo<sub>2</sub>O<sub>4</sub>@MnO<sub>2</sub> NSAs. More information about the FeCo<sub>2</sub>O<sub>4</sub> nanosheets and FeCo<sub>2</sub>O<sub>4</sub>@MnO<sub>2</sub> NSAs was recorded by the TEM (Figure 27). Figure 27a-b further revealed the ultrathin and quasi-rectangular features of FeCo<sub>2</sub>O<sub>4</sub> nanosheets. Furthermore, the TEM images of FeCo<sub>2</sub>O<sub>4</sub> nanosheets also exhibited that the mesopores with different diameters uniformly distributed in the FeCo<sub>2</sub>O<sub>4</sub> nanosheets. The HRTEM image of FeCo<sub>2</sub>O<sub>4</sub> nanosheets was presented in Figure 27c. The lattice spacing was 0.296 nm, measured from the lattice fringe, which corresponded to the (220) plane of FeCo<sub>2</sub>O<sub>4</sub>.<sup>41</sup> In addition, the corresponding SAED pattern (inset of Figure 27b) revealed that the FeCo<sub>2</sub>O<sub>4</sub> nanosheets were crystalline in whole. The TEM images of FeCo<sub>2</sub>O<sub>4</sub>@MnO<sub>2</sub> NSAs (Figure

27d-e) clearly confirmed that the  $\text{FeCo}_2\text{O}_4$  nanosheets were totally covered by  $\text{MnO}_2$  nanosheets, and each individual substance components in  $\text{FeCo}_2\text{O}_4@ \text{MnO}_2$  nanostructures were closely packed. The freestanding  $\text{MnO}_2$  nanosheets partly overlapped with each other and formed a wrinkled nanostructure. The HRTEM image (Figure 27f) of  $\text{FeCo}_2\text{O}_4@ \text{MnO}_2$  NSAs clearly shows that the lattice fringe spaces of 0.19 nm, corresponding to the (111) planes of the birnessite-type  $\delta\text{-MnO}_2$ .<sup>82</sup> The obtained SAED pattern (inset of Figure 27e) of the nanosheets was in good agreement with the diffraction peaks of  $\delta\text{-MnO}_2$  obtained by XRD pattern.

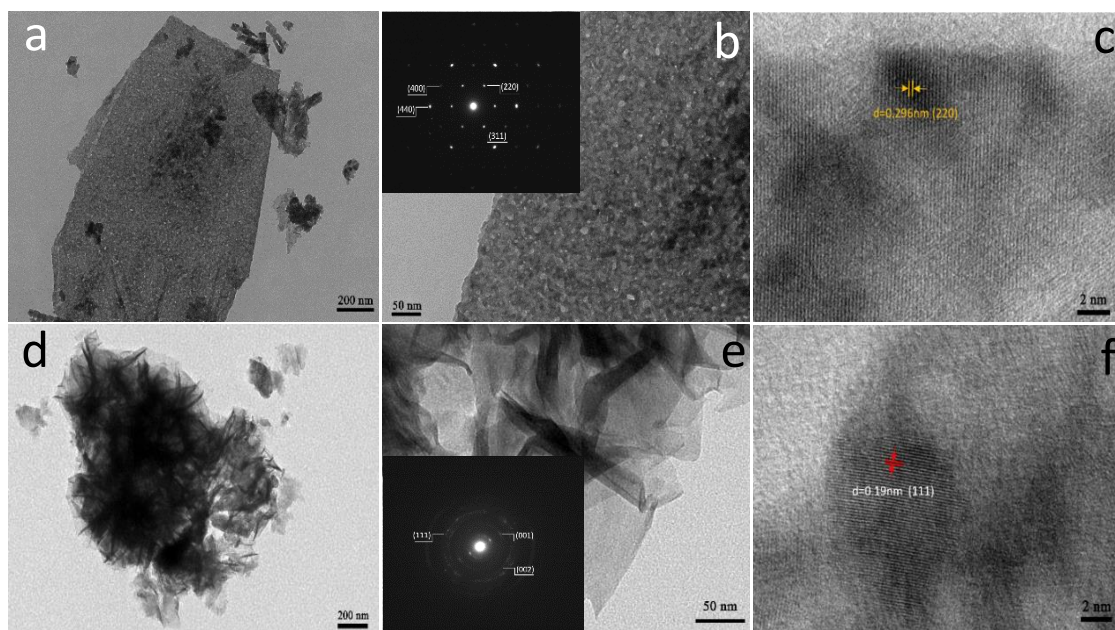


**Figure 27.** TEM images of (a-c)  $\text{FeCo}_2\text{O}_4$  nanosheets and (d-f)  $\text{FeCo}_2\text{O}_4@ \text{MnO}_2$  NSAs scratched from Ni foam. The insets of Figure b and e are the corresponding SAED pattern of  $\text{FeCo}_2\text{O}_4$  nanosheets and  $\text{FeCo}_2\text{O}_4@ \text{MnO}_2$  NSAs, respectively.

XPS tests were applied to further investigate the elemental chemical states and chemical

compositions on the surfaces of samples. Figure 28a exhibits the XPS spectrum of Co 2p, including two main peaks (Co 2p<sub>3/2</sub> and Co 2p<sub>1/2</sub>) and two satellite peaks. After fitting by the Gaussian method, Co 2p<sub>3/2</sub> can be divided into two subpeaks located at 779.7 eV and 781.1 eV and Co 2p<sub>1/2</sub> also split into two peaks at 794.8 eV and 796.0 eV. In addition, two “shoulder” weak satellite peaks were found at 786.6 eV and 804.0 eV, respectively. Among of them, the fitting peaks at 779.7 eV and 794.8 eV with the satellite peak of 786.6 were indexed to Co<sup>3+</sup>, while the other peaks at 781.1 eV, 796.0 eV and 804.0 eV were attributed to the existence of Co<sup>2+</sup> <sup>49, 78</sup>. Likewise, the XPS spectrum of Fe 2p (Figure 28b) also included two main peaks at 711.5 eV and 724.3 eV corresponding to Fe 2p<sub>3/2</sub> and Fe 2p<sub>1/2</sub> and two broad satellite peaks at 716.7 eV and 732.9 eV. The fitting peaks at 711.5 eV and 724.3 eV were associated to Fe<sup>2+</sup> and the two satellite peaks at 716.7 eV and 732.9 eV were related to Fe<sup>3+</sup> <sup>83-84</sup>. The XPS characterization clearly revealed that the FeCo<sub>2</sub>O<sub>4</sub> nanosheets belonged to the mixed valence compounds, which contained Co<sup>3+</sup>, Co<sup>2+</sup>, Fe<sup>3+</sup>, and Fe<sup>2+</sup>. The XPS spectrum of Mn 2p and O 1s of FeCo<sub>2</sub>O<sub>4</sub>@MnO<sub>2</sub> NSAs are shown in Figure 28c-d, respectively. Two main peaks at 642.5 eV and 650.0 eV belonged to Mn 2p<sub>3/2</sub> and Mn 2p<sub>1/2</sub>, indicating the chemical state of Mn in FeCo<sub>2</sub>O<sub>4</sub>@MnO<sub>2</sub> NSAs was +4 <sup>69</sup>. After fitting, the O 1s spectrum was divided into two fitting peaks, corresponding to two types of oxygen states named as O1 and O2. The O1 peak at 529.8 eV can be assigned to a typical metal-oxygen bond. Besides, the fitting O2 peak at 531.7 eV was caused by the physic- or

chemisorbed water at the surface<sup>48</sup>.

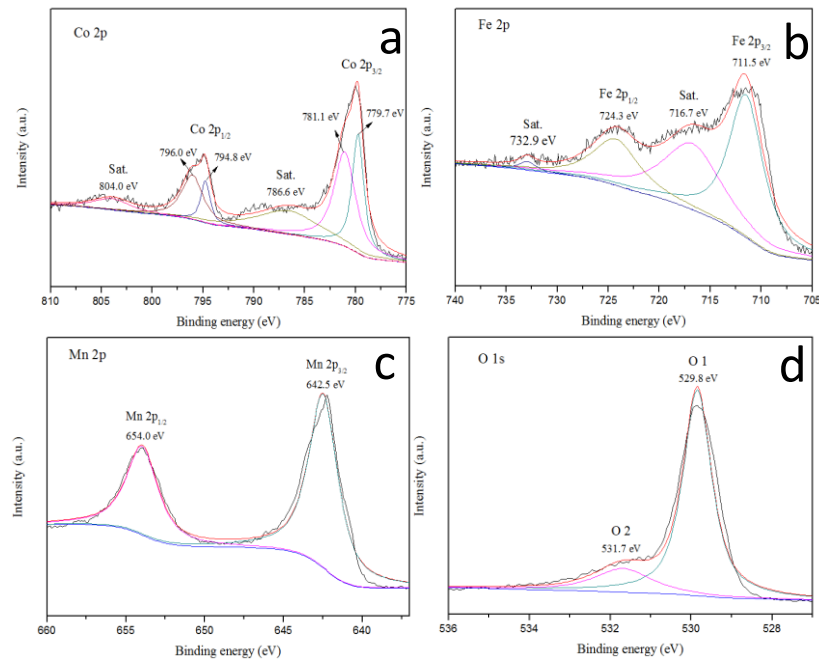


**Figure 28.** XPS spectra of the (a) Co 2p and (b) Fe 2p regions of FeCo<sub>2</sub>O<sub>4</sub> nanosheets. XPS spectra of the (c) Mn 2p and (d) O 1s of FeCo<sub>2</sub>O<sub>4</sub>@MnO<sub>2</sub> NSAs.

### 3.4.2 Electrochemical properties of $\text{FeCo}_2\text{O}_4@\text{MnO}_2$ electrode

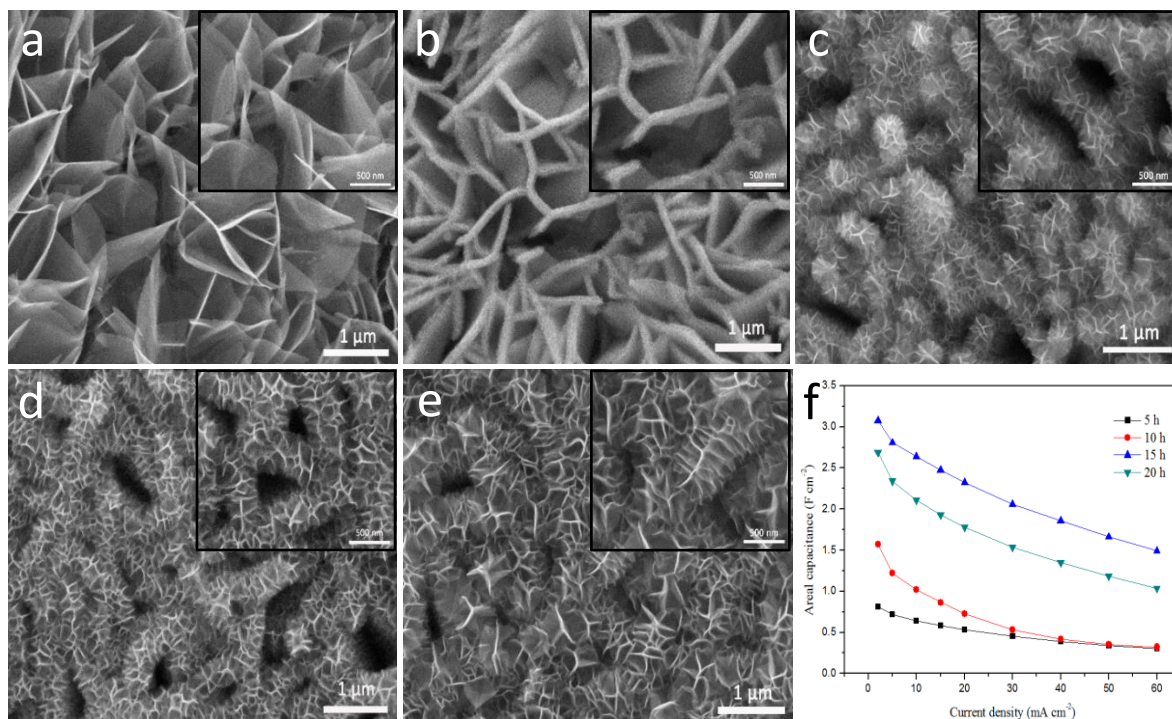


**Figure 29.** SEM images of the  $\text{FeCo}_2\text{O}_4@\text{MnO}_2$  NSAs obtained at different reaction times: (a) 0h; (b) 5h; (c) 10h; (d) 15h; and (e) 20h. Insets show the high-magnification SEM images. (f) Areal capacitances of  $\text{FeCo}_2\text{O}_4@\text{MnO}_2$  NSAs electrodes obtained at different reaction times and at different current densities.

In order to learn the effect of the proportion and size of each component on performance of electrode, different  $\text{FeCo}_2\text{O}_4@\text{MnO}_2$  composites with various thicknesses were synthesized. The thickness of  $\text{FeCo}_2\text{O}_4@\text{MnO}_2$  NSAs was controlled by different hydrothermal times for the  $\text{MnO}_2$  growth. Figure 29. presents the morphologies of  $\text{FeCo}_2\text{O}_4@\text{MnO}_2$  NSAs at different growth stages. As shown in Figure 29a, the smooth bare  $\text{FeCo}_2\text{O}_4$  nanosheets was vertically standing on the Ni foam, and its average thickness

was 10 nm. When the hydrothermal time reached 5h, the thickness of nanomaterial increased from 10 nm to 80 nm and tiny MnO<sub>2</sub> “buds” began to deposit on the surface of FeCo<sub>2</sub>O<sub>4</sub> nanosheets, as shown in the inset of Figure 29b. With the elongation of hydrothermal time, the thickness of FeCo<sub>2</sub>O<sub>4</sub>@MnO<sub>2</sub> NSAs changed to 250 nm at 10 h (Figure 29c), 400 nm at 15 h (Figure 29d) and 550 nm at 20 h (Figure 29e). It was clear that all the space between FeCo<sub>2</sub>O<sub>4</sub>@MnO<sub>2</sub> NSAs was almost occupied by MnO<sub>2</sub> nanosheets at 20h. The smaller inter-sheet space of prepared nanostructures obtained at 20 h may restrict the penetration of electrolytes into the inner of the NSAs structure.<sup>85</sup> Thus, FeCo<sub>2</sub>O<sub>4</sub>@MnO<sub>2</sub> NSAs electrodes at different growing stages were further tested by their electrochemical performance. Figure 30a shows the CV curves at 20 mV s<sup>-1</sup> of FeCo<sub>2</sub>O<sub>4</sub>@MnO<sub>2</sub> NSAs electrodes coming from different hydrothermal times. It indicated that the largest area of CV curve (the highest capacitance) referred to the FeCo<sub>2</sub>O<sub>4</sub>@MnO<sub>2</sub> NSAs of the hydrothermal time at 15h was (marked in blue). The areal capacitances at different current density of prepared electrodes was shown in Figure 29f, which further confirmed that the electrochemical performance was enhanced by increasing by the hydrothermal times until 15 h and decreased at 20 h. The corresponding discharge curves of 5 h, 10 h and 20 h were listed in Figure 30b-d, respectively. In addition, to better understand the function of FeCo<sub>2</sub>O<sub>4</sub> nanosheets in the construction of FeCo<sub>2</sub>O<sub>4</sub>@MnO<sub>2</sub> NSAs, the MnO<sub>2</sub> sample grown on the Ni foam was also prepared (Figure 30e-f). Without the well-oriented FeCo<sub>2</sub>O<sub>4</sub> nanosheets, stacked MnO<sub>2</sub> nanosheets can only be grown on the Ni foam irregularly.



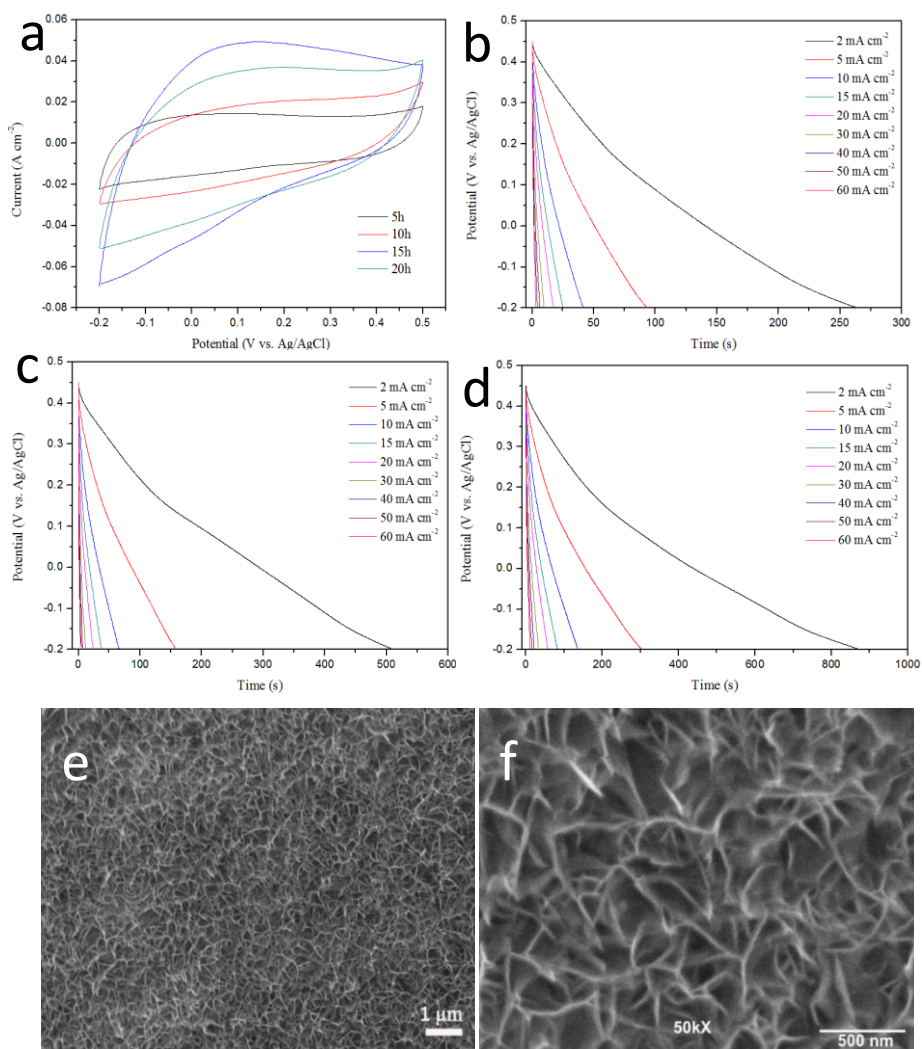


**Figure 30.** (a) CV curves of  $\text{FeCo}_2\text{O}_4@\text{MnO}_2$  NSAs fabricated with different reaction times at a scan rate of  $20 \text{ mV s}^{-1}$ . (b-d) Galvanostatic charge-discharge of the  $\text{FeCo}_2\text{O}_4@\text{MnO}_2$  NSAs fabricated with different reaction times at various current densities. (b) 5h; (c) 10h; (d) 20h. (e) Low- and (f) high-magnification SEM images of  $\text{MnO}_2$  nanosheets on the Ni foam prepared by the same hydrothermal synthesis (without pre-grown  $\text{FeCo}_2\text{O}_4$  nanosheets)

The electrochemical performance of FeCo<sub>2</sub>O<sub>4</sub>@MnO<sub>2</sub> NSAs was first investigated in a traditional three electrodes system. Figure 31a shows the CV curves of FeCo<sub>2</sub>O<sub>4</sub>@MnO<sub>2</sub> NSAs at different scan rates in a potential range of -0.2-0.5 V. The shapes of CV curves deviated from the rectangular character, indicating the pseudocapacitive behavior of the electrode. When the scan rate increased to 100 mV s<sup>-1</sup>, the shape of CV curve did not show much change, suggesting the good reversibility feature. Figure 31b exhibits the typical GCD profiles of FeCo<sub>2</sub>O<sub>4</sub>@MnO<sub>2</sub> NSAs at different current densities. According to equation (12), the areal capacitances of the FeCo<sub>2</sub>O<sub>4</sub>@MnO<sub>2</sub> NSAs were 3.077, 2.808, 2.642, 2.472, 2.323, 2.058, 1.860, 1.661 and 1.495 F cm<sup>-2</sup> at current densities of 2, 5, 10, 15, 20, 30, 40, 50 and 60 mA cm<sup>-2</sup>, respectively. (The corresponding specific capacitances were 1810.0, 1651.8, 1554.1, 1454.1, 1366.5, 1210.6, 1094.1, 977.1 and 879.4 F g<sup>-1</sup>) The confirmation of the enhanced performance of the FeCo<sub>2</sub>O<sub>4</sub>@MnO<sub>2</sub> NSAs was revealed in the comparison the electrochemical properties of the FeCo<sub>2</sub>O<sub>4</sub> nanosheets, the MnO<sub>2</sub> nanosheets and the FeCo<sub>2</sub>O<sub>4</sub>@MnO<sub>2</sub> NSAs. Figure 31c and d show the CV curves at 20 mV s<sup>-1</sup> and GCD curves at 5 mA cm<sup>-2</sup> of all samples of all three electrodes, respectively. The CV shape of the FeCo<sub>2</sub>O<sub>4</sub>@MnO<sub>2</sub> NSAs was completely different from those of FeCo<sub>2</sub>O<sub>4</sub> nanosheets and MnO<sub>2</sub> nanosheets and the coverage area of its CV curve was also much larger than both of other two electrodes. It implied that both FeCo<sub>2</sub>O<sub>4</sub> and MnO<sub>2</sub> were active pseudocapacitor materials which based on the reversible Faradic redox reaction in their energy storage mechanism. The CV curve of FeCo<sub>2</sub>O<sub>4</sub>@MnO<sub>2</sub> did not show obvious redox peak, indicating that the electrochemical properties of CoFe<sub>2</sub>O<sub>4</sub> and MnO<sub>2</sub> has been

changed upon the formation of the new  $\text{CoFe}_2\text{O}_4@\text{MnO}_2$  core-shell nanoarchitecture. A comparison of three GCD curves of electrodes at  $5 \text{ mA cm}^{-2}$  is illustrated in Figure 31d. Obviously, the charge-discharge time of  $\text{FeCo}_2\text{O}_4@\text{MnO}_2$  was much longer than those of  $\text{FeCo}_2\text{O}_4$  and  $\text{MnO}_2$  electrodes, corresponding to a much improved capacitance of the  $\text{FeCo}_2\text{O}_4@\text{MnO}_2$  electrode. It can also be seen that the charge-discharge curves of all three samples were in the symmetric status, suggesting their excellent columbic efficiencies.

In order to evaluate the rate capability of the  $\text{FeCo}_2\text{O}_4@\text{MnO}_2$  NSAs electrode, the specific areal capacitance of all three electrodes were compared at different current densities. When the current density increased to  $30 \text{ mA cm}^{-2}$ , which was 15-fold of the initial one, the capacitance of the  $\text{FeCo}_2\text{O}_4@\text{MnO}_2$  still remained  $2.058 \text{ F cm}^{-2}$  (Figure 31e). The capacitance retention was about 66.9% of the original value at  $2 \text{ mA cm}^{-2}$  of the  $\text{FeCo}_2\text{O}_4@\text{MnO}_2$  electrode, which was higher than the  $\text{FeCo}_2\text{O}_4$  electrode (51.5%) and the  $\text{MnO}_2$  electrode (33%) at  $30 \text{ mA cm}^{-2}$ , showing the remarkable rate capability of the  $\text{FeCo}_2\text{O}_4@\text{MnO}_2$  NSAs electrode. The GCD curves of  $\text{FeCo}_2\text{O}_4$  and  $\text{MnO}_2$  at different current densities are shown in the Figure 31f-g. In addition, we can see all the specific areal capacitances of  $\text{FeCo}_2\text{O}_4@\text{MnO}_2$  NSAs at different current densities were much higher than the sum of  $\text{CoFe}_2\text{O}_4$  and  $\text{MnO}_2$  NSs, further manifesting that the formation of an integrated core-shell nanoarchitecture was an efficient strategy to enhance the performance of electrode materials.

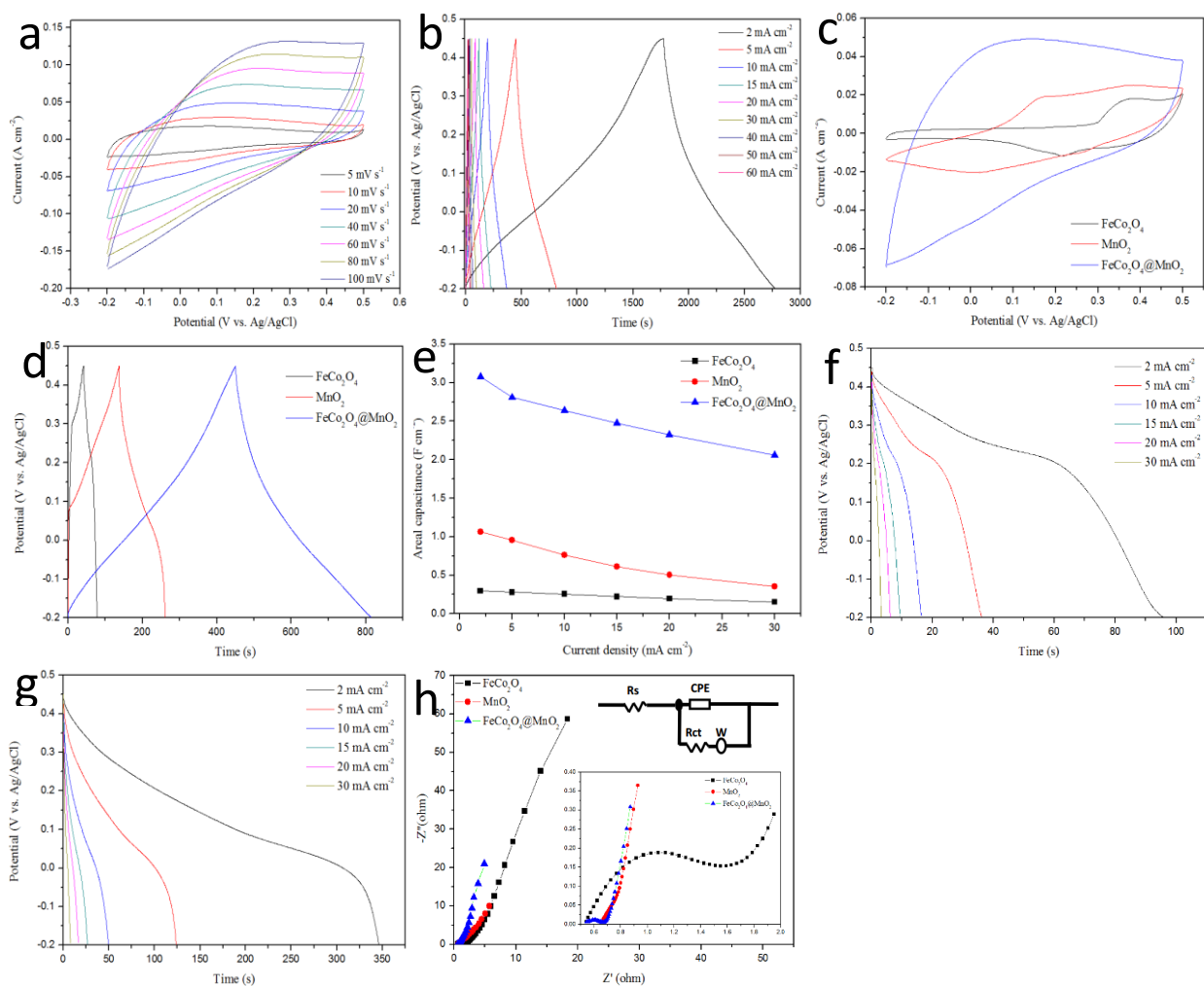


**Figure 31.** (a) CV curves of  $\text{FeCo}_2\text{O}_4@\text{MnO}_2$  NSAs at different scan rates. (b) Galvanostatic charge-discharge of the  $\text{FeCo}_2\text{O}_4@\text{MnO}_2$  NSAs at various current densities. (c-f) Comparing bare  $\text{FeCo}_2\text{O}_4$  electrode (black), bare  $\text{MnO}_2$  electrode (red) and optimal  $\text{FeCo}_2\text{O}_4@\text{MnO}_2$  NSAs electrode (blue), all grown on Ni foam: (c) CV curves at  $20 \text{ mV s}^{-1}$ , (d) galvanostatic charge-discharge at  $5 \text{ mA cm}^{-2}$ , (e) areal specific capacitances versus discharge current density, and (h) EIS curves (inset shows the EIS curves at high frequency, the equivalent circuit model is shown on the top right). Galvanostatic charge-discharge of the (f)  $\text{FeCo}_2\text{O}_4$  nanosheets and (g)  $\text{MnO}_2$  nanosheets on nickel foam at various current densities.

EIS tests were also conducted to learn the ion-transport behavior of all three prepared electrodes. The EIS spectra (Figure 31h) of all samples consisted of a semicircle at the high-frequency region and a straight line at the low-frequency region. The high-frequency intercept of the semicircle on the real axis represents the series resistance ( $R_s$ ) and its diameter represents the charge-transfer resistance ( $R_{ct}$ ) of the Faradaic process. Contrasting, the linear part in the low-frequency area is associated with the resistance (Warburg resistance  $W$ ) of electrolyte and ionic diffusion/transport into the electrode surface<sup>52-53</sup>. In the high-frequency region, the  $\text{FeCo}_2\text{O}_4@\text{MnO}_2$  demonstrated a similar  $R_s$  with pristine  $\text{FeCo}_2\text{O}_4$  nanosheets ( $0.54 \Omega$ ) which was smaller than that of bare  $\text{MnO}_2$  nanosheets ( $0.67\Omega$ ), indicating an improved electrical conductivity caused by the improved conductive  $\text{FeCo}_2\text{O}_4$  nanosheets. Remarkably, the smaller diameter of semicircle and the larger slope of the  $\text{FeCo}_2\text{O}_4@\text{MnO}_2$  than those of  $\text{FeCo}_2\text{O}_4$  nanosheets and  $\text{MnO}_2$  nanosheets also manifested its relatively smaller charge-transfer resistance and diffusive resistance caused by the intercalation and deintercalation of cations. The larger slope of  $\text{FeCo}_2\text{O}_4@\text{MnO}_2$  in the low-frequency region revealed its smaller diffusive resistance, indicating the vertically aligned  $\text{MnO}_2$  grown on  $\text{FeCo}_2\text{O}_4$  nanosheets could enhance the contact of active material and electrolyte as well as ion diffusion in the nanocomposite.

### **3.4.3 Electrochemical performance of $\text{FeCo}_2\text{O}_4@\text{MnO}_2//\text{AC}$ asymmetric supercapacitor**

In order to explore the practical application of the  $\text{FeCo}_2\text{O}_4@\text{MnO}_2$  NSAs electrode, an

aqueous asymmetric supercapacitor was further assembled using  $\text{FeCo}_2\text{O}_4@\text{MnO}_2$  NSAs as its positive electrode and AC as its negative electrode. Figure 32a exhibits CV curves of AC electrode and  $\text{FeCo}_2\text{O}_4@\text{MnO}_2$  NSAs electrode at  $10 \text{ mV s}^{-1}$ . The rectangular shape of AC in its CV curve revealed electrochemical double layer capacitive property, while the trapeziform shape of  $\text{FeCo}_2\text{O}_4@\text{MnO}_2$  in its CV indicated its pseudocapacitive property. The stable working potential window of the  $\text{FeCo}_2\text{O}_4@\text{MnO}_2//\text{AC}$  ASC was investigated by the increase of CV range progressively (Figure 32b) to determine a proper range of voltage window to be 0-1.65 V. With the increase of scan rates in CV experiments, the shape of CV curves (Figure 32c) tended to be more quasi-rectangular and didn't show any redox peaks, indicating excellent charge-discharge property and rate capability of the ASC device. The absence of obvious redox peaks should be attributed to the combination of  $\text{FeCo}_2\text{O}_4@\text{MnO}_2$  NSAs electrode and the AC electrode, the same phenomena also observed in other pseudocapacitive ASC.<sup>86</sup> The capacitances of full cell were investigated by GCD experiments (Figure 32d). The charge-discharge curves of the  $\text{FeCo}_2\text{O}_4@\text{MnO}_2//\text{AC}$  ASC remained nearly symmetric suggesting the excellent capacitive behavior of the device in 0-1.65 V. Figure 32e shows the areal capacitances at different current density and corresponding capacitance retention.  $\text{FeCo}_2\text{O}_4@\text{MnO}_2//\text{AC}$  ASC achieved an areal capacitance of  $0.646 \text{ F cm}^{-2}$  ( $80.75 \text{ F g}^{-1}$ ) at  $5 \text{ mA cm}^{-2}$  and still remained  $0.28 \text{ F cm}^{-2}$  ( $35.0 \text{ F g}^{-1}$ ) (43.4% of its initial value) even at a high current density of  $60 \text{ mA cm}^{-2}$ . Besides, the self-discharge property of the device was performed under open-circuit voltage conditions. As shown in Figure 32f, after charging to 1.65 V, the ASC device

showed a voltage drop about 50% after 4 h and almost stabilized at 30% of the initial charge potential after 15 h, which was similar to the previously reported values.<sup>87</sup>

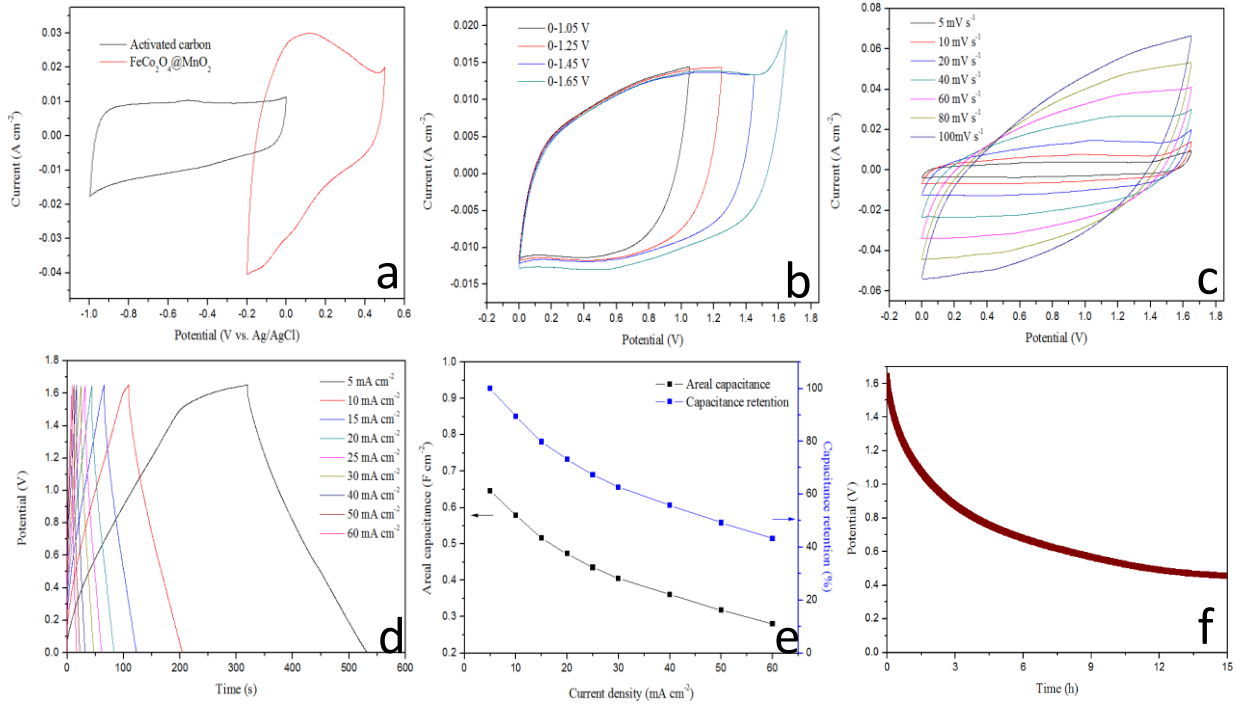


**Figure 32.** (a) Comparative CV curves of the activated carbon electrode and  $\text{FeCo}_2\text{O}_4@\text{MnO}_2$  NSAs electrode at  $10 \text{ mV s}^{-1}$ . (b) CV curves at different cell voltages at a scan rate of  $20 \text{ mV s}^{-1}$  and (c) different scan rates for  $\text{FeCo}_2\text{O}_4@\text{MnO}_2//\text{AC}$  ASC device. (d) Galvanostatic charge-discharge curves at different current densities. (e) Specific capacitances of the  $\text{FeCo}_2\text{O}_4@\text{MnO}_2//\text{AC}$  ASC device at different current densities. (f) Self-discharge curve of the  $\text{FeCo}_2\text{O}_4@\text{MnO}_2//\text{AC}$  ASC device.

Energy density and power density are two essential parameters to evaluate the performance of supercapacitors. Figure 33 shows the Ragone plot of  $\text{FeCo}_2\text{O}_4@\text{MnO}_2//\text{AC}$  ASC calculated from GCD tests. The maximum energy density of the ASC was  $0.23 \text{ mWh cm}^{-2}$  ( $30.55 \text{ W h kg}^{-1}$ ) at a power density of  $3.88 \text{ mW cm}^{-2}$  ( $515.6 \text{ W kg}^{-1}$ ) and decreased to

0.1 mWh cm<sup>-2</sup> (13.2 W h kg<sup>-1</sup>) at a power density of 46.5 mW cm<sup>-2</sup> (6187.5 W kg<sup>-1</sup>). These values are significantly superior to the previous reported ASCs, such as NiCo<sub>2</sub>S<sub>4</sub>@Ni-Mn LDH/GS//VN/GS ASC (0.156 mWh cm<sup>-2</sup> at a power density of 3.76 mW cm<sup>-2</sup>)<sup>88</sup>, Ni, Co-HC//HPC ASC (0.137 mWh cm<sup>-2</sup> at a power density of 3.51 mW cm<sup>-2</sup>)<sup>89</sup>, CW/PNC/PEDOT//CW/CMK-3 ASC (0.011 mWh cm<sup>-2</sup> at a power density of 0.33 mW cm<sup>-2</sup>)<sup>90</sup> and Ni(OH)<sub>2</sub> NW//OMC ASC (0.01 mWh cm<sup>-2</sup> at a power density of 7.3 mW cm<sup>-2</sup>)<sup>91</sup>. More impressively, the excellent cycling stability of the FeCo<sub>2</sub>O<sub>4</sub>@MnO<sub>2</sub>//AC ASC also can promote its practical application. A long-term cycling test was recorded at a current density of 40 mA cm<sup>-2</sup>. As shown in Figure 33b, the capacitance of the FeCo<sub>2</sub>O<sub>4</sub>@MnO<sub>2</sub>//AC ASC still retained 99.1% of its original capacitance even after 5000 cycles. The increased capacitance during the first 1000 cycles should be attributed to the activation of electrode material. In general, only a portion of material can be activated and take part in the charge-discharge process in the beginning. Complying with the penetration of electrolyte, more of the electrode materials became activated and contributed to the increase of capacitance.<sup>92</sup> Figure 33c-d show the typical first and last ten charge-discharge cycles and the CD curves still remained undistorted and almost symmetric, indicating the excellent stability of FeCo<sub>2</sub>O<sub>4</sub>@MnO<sub>2</sub>//AC ASC. Two FeCo<sub>2</sub>O<sub>4</sub>@MnO<sub>2</sub>//AC ASC devices were further assembled in series. After charged for 30s to about 3.3 V, the connected devices efficiently powered 10 light-emitting diode (LED) indicators (green, 2.3 V, 20mA for each) (Inset of Figure 34a) and lasted for about 6 minutes (Figure 33e).



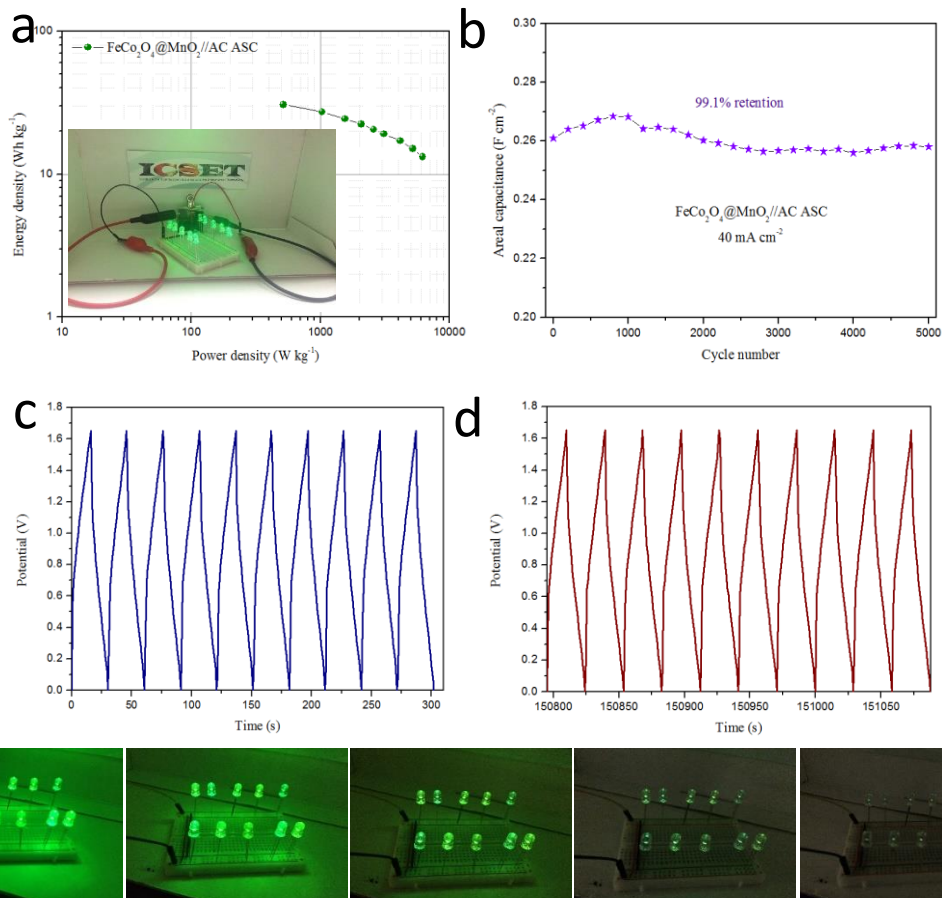


**Figure 33.** (a) Ragone plot of the FeCo<sub>2</sub>O<sub>4</sub>@MnO<sub>2</sub>//AC ASC device. Inset shows a digital image of two ASC devices in series which can light up ten green LED indicators. (b) Cycling stability of FeCo<sub>2</sub>O<sub>4</sub>@MnO<sub>2</sub>//AC ASC device at a current density of 40 mA cm<sup>-2</sup>. (c) First and (d) last 10 charge-discharge curves of FeCo<sub>2</sub>O<sub>4</sub>@MnO<sub>2</sub>//AC-ASC device at 40 mA cm<sup>-2</sup> current density in the potential range between 0-1.65 V for 5000 cycles. (e) Images of the green LEDs at different stages.

## IV. CONCLUSION

Due to the renewable energy resources are unstable and sporadic, suggesting that energy storage devices must be coexisted to keep them in reserve and use them in demands. Supercapacitor is one of the most promising devices for energy storage and has attracted considerable interest in recent years because of its high power density, fast charging-discharging rate and long lifespan. In this study, we synthesized several type bimetallic iron cobalt oxides based materials and applied them as the electrodes for supercapacitor.

Firstly,  $\text{CoFe}_2\text{O}_4$  and  $\text{FeCo}_2\text{O}_4$  nanosheets were grown on Ni foam by hydrothermal and post-annealing process. Amongst, the interconnected  $\text{CoFe}_2\text{O}_4$  nanosheets supported on Ni foam was fabricated for the first time. The as-fabricated  $\text{CoFe}_2\text{O}_4$  nanosheets, as a positive supercapacitor electrodes, exhibited a high capacitance of  $503 \text{ F g}^{-1}$  at a current density of  $2 \text{ A g}^{-1}$  which was higher than its corresponding monometallic transition oxides. An aqueous  $\text{CoFe}_2\text{O}_4//\text{AC}$  ASC was further assembled and achieved high specific capacitance of  $73.12 \text{ F g}^{-1}$  at  $1.2 \text{ A g}^{-1}$  and long lifespan of 98% retention of its original specific capacitance after 5000cycles. The maximum energy density and power density can be up to  $22.85 \text{ W h kg}^{-1}$  and  $6000 \text{ W kg}^{-1}$ , respectively.

Then, we developed a facile and short-term route to synthesize the binder-additive-free  $\text{MCo}_2\text{O}_4$  (M=Co and Fe) submicron-structured prisms grown on the nickel foam via the hydrothermal assisted co-precipitation method. The electrochemical properties of  $\text{MCo}_2\text{O}_4$  SMPs electrodes were first investigated in three-electrode system. It was found that all the

MCo<sub>2</sub>O<sub>4</sub> SMPs exhibited the OH<sup>-</sup> diffusion-controlled characteristic of the redox reactions. The MCo<sub>2</sub>O<sub>4</sub> (M= Co and Fe) SMPs achieved specific capacitances of 680.5 F g<sup>-1</sup> (1.64 F cm<sup>-2</sup>), 1281.0 F g<sup>-1</sup> (1.96 F cm<sup>-2</sup>), respectively, at a current density of 2 mA cm<sup>-2</sup>. Between these two submicron prisms, Co<sub>3</sub>O<sub>4</sub> exhibited a better diffusion coefficient but lower series resistance.

Moreover, the bare CoFe<sub>2</sub>O<sub>4</sub> and FeCo<sub>2</sub>O<sub>4</sub> nanosheets were served as the scaffold for the deposition of MnO<sub>2</sub>. We developed a facial, tunable hydrothermal method to fabricate hierarchical CoFe<sub>2</sub>O<sub>4</sub>@ MnO<sub>2</sub> and FeCo<sub>2</sub>O<sub>4</sub>@ MnO<sub>2</sub> nanosheets arrays on Ni foam. The CoFe<sub>2</sub>O<sub>4</sub>@ MnO<sub>2</sub> NSAs exhibited a high specific capacitance of 3.59 F cm<sup>-2</sup> (1994.4 F g<sup>-1</sup>) at a current density of 2 mA cm<sup>-2</sup> within -0.2-0.4 V (vs. Ag/AgCl), which was much higher than bare CoFe<sub>2</sub>O<sub>4</sub> and MnO<sub>2</sub> nanosheets. The excellent performance exhibited by CoFe<sub>2</sub>O<sub>4</sub>@MnO<sub>2</sub> NSAs was likely attributed to the synergetic effects between the properties of two components and their unique core-shell nanostructure. In addition, the assembled CoFe<sub>2</sub>O<sub>4</sub>@MnO<sub>2</sub>//AC ASC could be operated within a voltage window of 0-1.6 V and achieved a high specific capacitance of 103.86 F g<sup>-1</sup> (0.883 F cm<sup>-2</sup>) at 5 mA cm<sup>-2</sup>, and still retained 43.12 F g<sup>-1</sup> (0.367 F cm<sup>-2</sup>) at a high current density of 51 mA cm<sup>-2</sup>. A maximum energy density was 37 W h kg<sup>-1</sup>, and the cycling stability reached 91.4% retention after 2250 cycles.

The FeCo<sub>2</sub>O<sub>4</sub>@ MnO<sub>2</sub> nanocomposite were prepared by similar strategy, the thickness of nanocomposite could be adjusted by the deposition time of MnO<sub>2</sub>. An optimal FeCo<sub>2</sub>O<sub>4</sub>@MnO<sub>2</sub> CSN electrode obtained at 15 h exhibited an areal capacitance 3.077 F

$\text{cm}^{-2}$  ( $1810 \text{ F g}^{-1}$ ) at  $2 \text{ mA cm}^{-2}$ . Also, an asymmetric supercapacitor  $\text{FeCo}_2\text{O}_4@\text{MnO}_2//\text{AC}$  ASC were further assembled for the first time. The as-assembled  $\text{FeCo}_2\text{O}_4@\text{MnO}_2//\text{AC}$  ASC could be operated within a large potential window of 0-1.65 V and delivered a high areal capacitance of  $0.646 \text{ F cm}^{-2}$  ( $80.75 \text{ F g}^{-1}$ ) at  $5 \text{ mA cm}^{-2}$  and excellent cycling stability with a 99.1% retention after 5000 cycles. In addition, the  $\text{FeCo}_2\text{O}_4@\text{MnO}_2//\text{AC}$  ASC achieved a maximum energy density of  $0.23 \text{ mWh cm}^{-2}$  ( $30.53 \text{ Wh kg}^{-1}$ ) at a power density of  $3.88 \text{ mW cm}^{-2}$  ( $515.6 \text{ W kg}^{-1}$ ), which was smaller than  $\text{CoFe}_2\text{O}_4@\text{MnO}_2//\text{AC}$  ASC.

In conclusion, we designed and fabricated a series of iron cobalt oxides based materials which could be applied as the positive electrode materials for supercapacitor for the first time. The influences of morphologies and the ratio of components were investigated. Given the low cost, facile process and the excellent electrochemical performance, the as-fabricated samples are expected to be novel electrode materials for the next generation energy storage devices.

## V. LITERATURE CITED

1. Miller, J. R.; Simon, P., Electrochemical capacitors for energy management. *Science Magazine* **2008**, *321* (5889), 651-652.
2. Zhao, X.; Johnston, C.; Grant, P. S., A novel hybrid supercapacitor with a carbon nanotube cathode and an iron oxide/carbon nanotube composite anode. *Journal of Materials Chemistry* **2009**, *19* (46), 8755-8760.
3. Sharma, C. S.; Awasthi, R.; Singh, R. N.; Sinha, A. S. K., Graphene–cobaltite–Pd hybrid materials for use as efficient bifunctional electrocatalysts in alkaline direct methanol fuel cells. *Physical Chemistry Chemical Physics* **2013**, *15* (46), 20333-20344.
4. Winter, M.; Brodd, R. J., What are batteries, fuel cells, and supercapacitors? ACS Publications: 2004.
5. Spinner, N.; Mustain, W. E., Effect of nickel oxide synthesis conditions on its physical properties and electrocatalytic oxidation of methanol. *Electrochimica Acta* **2011**, *56* (16), 5656-5666.
6. Liang, K.; Tang, X.; Hu, W., High-performance three-dimensional nanoporous NiO film as a supercapacitor electrode. *Journal of Materials Chemistry* **2012**, *22* (22), 11062-11067.
7. Gao, Y.; Chen, S.; Cao, D.; Wang, G.; Yin, J., Electrochemical capacitance of Co<sub>3</sub>O<sub>4</sub> nanowire arrays supported on nickel foam. *Journal of Power Sources* **2010**, *195* (6), 1757-1760.

8. Cheng, K.; Cao, D.; Yang, F.; Xu, Y.; Sun, G.; Ye, K.; Yin, J.; Wang, G., Facile synthesis of morphology-controlled  $\text{Co}_3\text{O}_4$  nanostructures through solvothermal method with enhanced catalytic activity for  $\text{H}_2\text{O}_2$  electroreduction. *Journal of Power Sources* **2014**, *253*, 214-223.
9. Guo, B.; Li, C.; Yuan, Z.-Y., Nanostructured  $\text{Co}_3\text{O}_4$  materials: synthesis, characterization, and electrochemical behaviors as anode reactants in rechargeable lithium ion batteries. *The Journal of Physical Chemistry C* **2010**, *114* (29), 12805-12817.
10. Chen, S.; Zhu, J.; Wu, X.; Han, Q.; Wang, X., Graphene oxide– $\text{MnO}_2$  nanocomposites for supercapacitors. *ACS nano* **2010**, *4* (5), 2822-2830.
11. He, Y.; Chen, W.; Li, X.; Zhang, Z.; Fu, J.; Zhao, C.; Xie, E., Freestanding three-dimensional graphene/ $\text{MnO}_2$  composite networks as ultralight and flexible supercapacitor electrodes. *ACS nano* **2012**, *7* (1), 174-182.
12. Yu, M.; Chen, J.; Liu, J.; Li, S.; Ma, Y.; Zhang, J.; An, J., Mesoporous  $\text{NiCo}_2\text{O}_4$  nanoneedles grown on 3D graphene-nickel foam for supercapacitor and methanol electro-oxidation. *Electrochimica Acta* **2015**, *151*, 99-108.
13. Chen, Y.; Zhu, J.; Qu, B.; Lu, B.; Xu, Z., Graphene improving lithium-ion battery performance by construction of  $\text{NiCo}_2\text{O}_4$ /graphene hybrid nanosheet arrays. *Nano Energy* **2014**, *3*, 88-94.
14. Kang, W.; Tang, Y.; Li, W.; Li, Z.; Yang, X.; Xu, J.; Lee, C.-S., Porous  $\text{CuCo}_2\text{O}_4$  nanocubes wrapped by reduced graphene oxide as high-performance lithium-ion battery anodes. *Nanoscale* **2014**, *6* (12), 6551-6556.

15. Simon, P.; Gogotsi, Y., Materials for electrochemical capacitors. *Nature materials* **2008**, 7 (11), 845-854.
16. Zhang, L. L.; Zhao, X. S., Carbon-based materials as supercapacitor electrodes. *Chemical Society Reviews* **2009**, 38 (9), 2520-2531.
17. Wang, G.; Zhang, L.; Zhang, J., A review of electrode materials for electrochemical supercapacitors. *Chemical Society Reviews* **2012**, 41 (2), 797-828.
18. Pendashteh, A.; Palma, J.; Anderson, M.; Marcilla, R., Nanostructured porous wires of iron cobaltite: novel positive electrode for high-performance hybrid energy storage devices. *Journal of Materials Chemistry A* **2015**, 3 (32), 16849-16859.
19. Zhu, B.; Tang, S.; Vongehr, S.; Xie, H.; Meng, X., Hierarchically MnO<sub>2</sub>-nanosheet covered submicrometer-FeCo<sub>2</sub>O<sub>4</sub>-tube forest as binder-free electrodes for high energy density all-solid-state supercapacitors. *ACS applied materials & interfaces* **2016**, 8 (7), 4762-4770.
20. Ji, L.; Lin, Z.; Alcoutlabi, M.; Zhang, X., Recent developments in nanostructured anode materials for rechargeable lithium-ion batteries. *Energy & Environmental Science* **2011**, 4 (8), 2682-2699.
21. Tarascon, J. M.; Armand, M., Issues and challenges facing rechargeable lithium batteries. *Nature* **2001**, 414 (6861), 359-367.
22. Li, Z. H.; Zhao, T. P.; Zhan, X. Y.; Gao, D. S.; Xiao, Q. Z.; Lei, G. T., High capacity three-dimensional ordered macroporous CoFe<sub>2</sub>O<sub>4</sub> as anode material for lithium ion batteries. *Electrochimica Acta* **2010**, 55 (15), 4594-4598.

23. Zhou, G.; Wang, D.-W.; Li, F.; Zhang, L.; Li, N.; Wu, Z.-S.; Wen, L.; Lu, G. Q.; Cheng, H.-M., Graphene-wrapped Fe<sub>3</sub>O<sub>4</sub> anode material with improved reversible capacity and cyclic stability for lithium ion batteries. *Chemistry of Materials* **2010**, 22 (18), 5306-5313.
24. Cabana, J.; Monconduit, L.; Larcher, D.; Palacin, M. R., Beyond Intercalation-Based Li-Ion Batteries: The State of the Art and Challenges of Electrode Materials Reacting Through Conversion Reactions. *Advanced Materials* **2010**, 22 (35).
25. Li, S.; Wang, B.; Liu, J.; Yu, M., In situ one-step synthesis of CoFe<sub>2</sub>O<sub>4</sub>/graphene nanocomposites as high-performance anode for lithium-ion batteries. *Electrochimica Acta* **2014**, 129, 33-39.
26. Lavela, P.; Tirado, J. L., CoFe<sub>2</sub>O<sub>4</sub> and NiFe<sub>2</sub>O<sub>4</sub> synthesized by sol-gel procedures for their use as anode materials for Li ion batteries. *Journal of power sources* **2007**, 172 (1), 379-387.
27. Sharma, Y.; Sharma, N.; Rao, G. V. S.; Chowdari, B. V. R., Studies on spinel cobaltites, FeCo<sub>2</sub>O<sub>4</sub> and MgCo<sub>2</sub>O<sub>4</sub> as anodes for Li-ion batteries. *Solid State Ionics* **2008**, 179 (15), 587-597.
28. Nam, K. T.; Kim, D.-W.; Yoo, P. J.; Chiang, C.-Y.; Meethong, N.; Hammond, P. T.; Chiang, Y.-M.; Belcher, A. M., Virus-enabled synthesis and assembly of nanowires for lithium ion battery electrodes. *science* **2006**, 312 (5775), 885-888.
29. Lou, X. W.; Deng, D.; Lee, J. Y.; Feng, J.; Archer, L. A., Self-supported formation of needlelike Co<sub>3</sub>O<sub>4</sub> nanotubes and their application as lithium-ion battery electrodes. *Advanced Materials* **2008**, 20 (2), 258-262.



30. Shi, Y.; Guo, B.; Corr, S. A.; Shi, Q.; Hu, Y.-S.; Heier, K. R.; Chen, L.; Seshadri, R.; Stucky, G. D., Ordered mesoporous metallic MoO<sub>2</sub> materials with highly reversible lithium storage capacity. *Nano letters* **2009**, *9* (12), 4215-4220.
31. Guo, H.; Li, T.; Chen, W.; Liu, L.; Yang, X.; Wang, Y.; Guo, Y., General design of hollow porous CoFe<sub>2</sub>O<sub>4</sub> nanocubes from metal–organic frameworks with extraordinary lithium storage. *Nanoscale* **2014**, *6* (24), 15168-15174.
32. Kirubakaran, A.; Jain, S.; Nema, R. K., A review on fuel cell technologies and power electronic interface. *Renewable and Sustainable Energy Reviews* **2009**, *13* (9), 2430-2440.
33. Li, Y. S.; Zhao, T. S.; Liang, Z. X., Effect of polymer binders in anode catalyst layer on performance of alkaline direct ethanol fuel cells. *Journal of Power Sources* **2009**, *190* (2), 223-229.
34. Zheng, Y.; Jiao, Y.; Jaroniec, M.; Jin, Y.; Qiao, S. Z., Nanostructured Metal-Free Electrochemical Catalysts for Highly Efficient Oxygen Reduction. *Small* **2012**, *8* (23), 3550-3566.
35. Gu, L.; Luo, N.; Miley, G. H., Cathode electrocatalyst selection and deposition for a direct borohydride/hydrogen peroxide fuel cell. *Journal of Power Sources* **2007**, *173* (1), 77-85.
36. Wang, H.; Sun, Z.; Yang, Y.; Su, D., The growth and enhanced catalytic performance of Au@ Pd core–shell nanodendrites. *Nanoscale* **2013**, *5* (1), 139-142.
37. Kua, J.; Goddard, W. A., Oxidation of methanol on 2nd and 3rd row group VIII transition metals (Pt, Ir, Os, Pd, Rh, and Ru): application to direct methanol fuel cells.

*Journal of the American Chemical Society* **1999**, *121* (47), 10928-10941.

38. Xia, B. Y.; Wu, H. B.; Wang, X.; Lou, X. W., One-pot synthesis of cubic PtCu<sub>3</sub> nanocages with enhanced electrocatalytic activity for the methanol oxidation reaction.

*Journal of the American chemical Society* **2012**, *134* (34), 13934-13937.

39. Xu, Y.; Bian, W.; Wu, J.; Tian, J.-H.; Yang, R., Preparation and electrocatalytic activity of 3D hierarchical porous spinel CoFe<sub>2</sub>O<sub>4</sub> hollow nanospheres as efficient catalyst for oxygen reduction reaction and oxygen evolution reaction. *Electrochimica Acta* **2015**, *151*, 276-283.

40. Yan, W.; Cao, X.; Ke, K.; Tian, J.; Jin, C.; Yang, R., One-pot synthesis of monodispersed porous CoFe<sub>2</sub>O<sub>4</sub> nanospheres on graphene as an efficient electrocatalyst for oxygen reduction and evolution reactions. *RSC Advances* **2016**, *6* (1), 307-313.

41. Yan, W.; Yang, Z.; Bian, W.; Yang, R., FeCo<sub>2</sub>O<sub>4</sub>/hollow graphene spheres hybrid with enhanced electrocatalytic activities for oxygen reduction and oxygen evolution reaction. *Carbon* **2015**, *92*, 74-83.

42. Cai, B.; Zhao, M.; Ma, Y.; Ye, Z.; Huang, J., Bioinspired formation of 3D hierarchical CoFe<sub>2</sub>O<sub>4</sub> porous microspheres for magnetic-controlled drug release. *ACS applied materials & interfaces* **2015**, *7* (2), 1327-1333.

43. Kargar, A.; Yavuz, S.; Kim, T. K.; Liu, C.-H.; Kuru, C.; Rustomji, C. S.; Jin, S.; Bandaru, P. R., Solution-processed CoFe<sub>2</sub>O<sub>4</sub> nanoparticles on 3D carbon fiber papers for durable oxygen evolution reaction. *ACS applied materials & interfaces* **2015**, *7* (32), 17851-17856.

44. Da Silva, S. W.; Melo, T. F. O.; Soler, M. A. G.; Lima, E. C. D.; Da Silva, M. F.; Morais, P. C., Stability of citrate-coated magnetite and cobalt-ferrite nanoparticles under laser irradiation: a Raman spectroscopy investigation. *IEEE transactions on magnetics* **2003**, *39* (5), 2645-2647.
45. Soler, M. A. G.; Melo, T. F. O.; Da Silva, S. W.; Lima, E. C. D.; Pimenta, A. C. M.; Garg, V. K.; Oliveira, A. C.; Morais, P. C., Structural stability study of cobalt ferrite-based nanoparticle using micro Raman spectroscopy. *Journal of magnetism and magnetic materials* **2004**, *272*, 2357-2358.
46. Dubal, D. P.; Gomez-Romero, P.; Sankapal, B. R.; Holze, R., Nickel cobaltite as an emerging material for supercapacitors: an overview. *Nano Energy* **2015**, *11*, 377-399.
47. Hu, L.; Zhong, H.; Zheng, X.; Huang, Y.; Zhang, P.; Chen, Q., CoMn<sub>2</sub>O<sub>4</sub> spinel hierarchical microspheres assembled with porous nanosheets as stable anodes for lithium-ion batteries. *Scientific reports* **2012**, *2*, 986.
48. Marco, J. F.; Gancedo, J. R.; Gracia, M.; Gautier, J. L.; Rios, E.; Berry, F. J., Characterization of the nickel cobaltite, NiCo<sub>2</sub>O<sub>4</sub>, prepared by several methods: an XRD, XANES, EXAFS, and XPS study. *Journal of Solid State Chemistry* **2000**, *153* (1), 74-81.
49. Langell, M. A.; Anderson, M. D.; Carson, G. A.; Peng, L.; Smith, S., Valence-band electronic structure of Co<sub>3</sub>O<sub>4</sub> epitaxy on CoO (100). *Physical Review B* **1999**, *59* (7), 4791.
50. Zhou, Z.; Zhang, Y.; Wang, Z.; Wei, W.; Tang, W.; Shi, J.; Xiong, R., Electronic structure studies of the spinel CoFe<sub>2</sub>O<sub>4</sub> by X-ray photoelectron spectroscopy. *Applied Surface Science* **2008**, *254* (21), 6972-6975.

51. Ma, X.-J.; Kong, L.-B.; Zhang, W.-B.; Liu, M.-C.; Luo, Y.-C.; Kang, L., Facile fabrication and perfect cycle stability of 3D NiO@CoMoO<sub>4</sub> nanocomposite on Ni foam for supercapacitors. *RSC Advances* **2014**, *4* (34), 17884-17890.
52. Li, J.; Xie, H.; Li, Y.; Liu, J.; Li, Z., Electrochemical properties of graphene nanosheets/polyaniline nanofibers composites as electrode for supercapacitors. *Journal of Power Sources* **2011**, *196* (24), 10775-10781.
53. Mohamed, S. G.; Hung, T.-F.; Chen, C.-J.; Chen, C. K.; Hu, S.-F.; Liu, R.-S., Efficient energy storage capabilities promoted by hierarchical MnCo<sub>2</sub>O<sub>4</sub> nanowire-based architectures. *RSC Advances* **2014**, *4* (33), 17230-17235.
54. Liu, W.; Li, X.; Zhu, M.; He, X., High-performance all-solid state asymmetric supercapacitor based on Co<sub>3</sub>O<sub>4</sub> nanowires and carbon aerogel. *Journal of Power Sources* **2015**, *282*, 179-186.
55. Lu, X.-F.; Wu, D.-J.; Li, R.-Z.; Li, Q.; Ye, S.-H.; Tong, Y.-X.; Li, G.-R., Hierarchical NiCo<sub>2</sub>O<sub>4</sub> nanosheets@hollow microrod arrays for high-performance asymmetric supercapacitors. *Journal of Materials Chemistry A* **2014**, *2* (13), 4706-4713.
56. Zhang, S.; Yin, B.; Wang, Z.; Peter, F., Super long-life all solid-state asymmetric supercapacitor based on NiO nanosheets and  $\alpha$ -Fe<sub>2</sub>O<sub>3</sub> nanorods. *Chemical Engineering Journal* **2016**, *306*, 193-203.
57. Yang, S.; Cheng, K.; Ye, K.; Li, Y.; Qu, J.; Yin, J.; Wang, G.; Cao, D., A novel asymmetric supercapacitor with buds-like Co(OH)<sub>2</sub> used as cathode materials and activated carbon as anode materials. *Journal of Electroanalytical Chemistry* **2015**, *741*, 93-99.

58. Shanmugavani, A.; Selvan, R. K., Improved electrochemical performances of  $\text{CuCo}_2\text{O}_4/\text{CuO}$  nanocomposites for asymmetric supercapacitors. *Electrochimica Acta* **2016**, *188*, 852-862.
59. Wang, H.; Holt, C. M. B.; Li, Z.; Tan, X.; Amirkhiz, B. S.; Xu, Z.; Olsen, B. C.; Stephenson, T.; Mitlin, D., Graphene-nickel cobaltite nanocomposite asymmetrical supercapacitor with commercial level mass loading. *Nano Research* **2012**, *5* (9), 605-617.
60. Yao, X.; Kong, J.; Tang, X.; Zhou, D.; Zhao, C.; Zhou, R.; Lu, X., Facile synthesis of porous  $\text{CoFe}_2\text{O}_4$  nanosheets for lithium-ion battery anodes with enhanced rate capability and cycling stability. *RSC Advances* **2014**, *4* (52), 27488-27492.
61. Fei, Z.; He, S.; Li, L.; Ji, W.; Au, C.-T., Morphology-directed synthesis of  $\text{Co}_3\text{O}_4$  nanotubes based on modified Kirkendall effect and its application in  $\text{CH}_4$  combustion. *Chemical Communications* **2012**, *48* (6), 853-855.
62. Mohamed, S. G.; Tsai, Y.-Q.; Chen, C.-J.; Tsai, Y.-T.; Hung, T.-F.; Chang, W.-S.; Liu, R.-S., Ternary Spinel  $\text{MCo}_2\text{O}_4$  (M= Mn, Fe, Ni, and Zn) Porous Nanorods as Bifunctional Cathode Materials for Lithium– $\text{O}_2$  Batteries. *ACS applied materials & interfaces* **2015**, *7* (22), 12038-12046.
63. Hongyan, G.; Junjie, X.; Yan, C., Controlled synthesis of  $\text{MnO}_2$  nanosheets vertically covered  $\text{FeCo}_2\text{O}_4$  nanoflakes as a binder-free electrode for a high-power and durable asymmetric supercapacitor. *Nanotechnology* **2017**, *28* (23), 235401.
64. Ma, F.-X.; Yu, L.; Xu, C.-Y.; Lou, X. W. D., Self-supported formation of hierarchical  $\text{NiCo}_2\text{O}_4$  tetragonal microtubes with enhanced electrochemical properties. *Energy &*

*Environmental Science* **2016**, 9 (3), 862-866.

65. Gao, H.; Cao, S.; Cao, Y., Hierarchical Core-Shell Nanosheet Arrays with MnO<sub>2</sub> Grown on Mesoporous CoFe<sub>2</sub>O<sub>4</sub> Support for High-Performance Asymmetric Supercapacitors. *Electrochimica Acta* **2017**, 240, 31-42.

66. Bard, A. J.; Faulkner, L. R.; Leddy, J.; Zoski, C. G., *Electrochemical methods: fundamentals and applications*. Wiley New York: 1980; Vol. 2.

67. Liu, L.; Zhang, H.; Mu, Y.; Bai, Y.; Wang, Y., Binary cobalt ferrite nanomesh arrays as the advanced binder-free electrode for applications in oxygen evolution reaction and supercapacitors. *Journal of Power Sources* **2016**, 327, 599-609.

68. Liu, L.; Zhang, H.; Mu, Y.; Yang, J.; Wang, Y., Porous iron cobaltate nanoneedles array on nickel foam as anode materials for lithium-ion batteries with enhanced electrochemical performance. *ACS applied materials & interfaces* **2016**, 8 (2), 1351-1359.

69. Hu, L.; Chen, W.; Xie, X.; Liu, N.; Yang, Y.; Wu, H.; Yao, Y.; Pasta, M.; Alshareef, H. N.; Cui, Y., Symmetrical MnO<sub>2</sub>-carbon nanotube-textile nanostructures for wearable pseudocapacitors with high mass loading. *Acs Nano* **2011**, 5 (11), 8904-8913.

70. Marco, J. F.; Gancedo, J. R.; Gracia, M.; Gautier, J. L.; Rios, E.; Berry, F. J., Characterization of the nickel cobaltite, NiCo<sub>2</sub>O<sub>4</sub>, prepared by several methods: an XRD, XANES, EXAFS, and XPS study. *Journal of Solid State Chemistry* **2000**, 153 (1), 74-81.

71. Guo, D.; Luo, Y.; Yu, X.; Li, Q.; Wang, T., High performance NiMoO<sub>4</sub> nanowires supported on carbon cloth as advanced electrodes for symmetric supercapacitors. *Nano Energy* **2014**, 8, 174-182.

72. Augustyn, V.; Simon, P.; Dunn, B., Pseudocapacitive oxide materials for high-rate electrochemical energy storage. *Energy & Environmental Science* **2014**, 7 (5), 1597-1614.
73. Chang, B.-Y.; Park, S.-M., Electrochemical impedance spectroscopy. *Annual Review of Analytical Chemistry* **2010**, 3, 207-229.
74. Li, W.; Li, G.; Sun, J.; Zou, R.; Xu, K.; Sun, Y.; Chen, Z.; Yang, J.; Hu, J., Hierarchical heterostructures of MnO<sub>2</sub> nanosheets or nanorods grown on Au-coated Co<sub>3</sub>O<sub>4</sub> porous nanowalls for high-performance pseudocapacitance. *Nanoscale* **2013**, 5 (7), 2901-2908.
75. Huang, M.; Zhang, Y.; Li, F.; Zhang, L.; Wen, Z.; Liu, Q., Facile synthesis of hierarchical Co<sub>3</sub>O<sub>4</sub>@ MnO<sub>2</sub> core-shell arrays on Ni foam for asymmetric supercapacitors. *Journal of Power Sources* **2014**, 252, 98-106.
76. Lei, Z.; Zhang, J.; Zhao, X. S., Ultrathin MnO<sub>2</sub> nanofibers grown on graphitic carbon spheres as high-performance asymmetric supercapacitor electrodes. *Journal of Materials Chemistry* **2012**, 22 (1), 153-160.
77. Kuang, M.; Wen, Z. Q.; Guo, X. L.; Zhang, S. M.; Zhang, Y. X., Engineering firecracker-like beta-manganese dioxides@ spinel nickel cobaltates nanostructures for high-performance supercapacitors. *Journal of Power Sources* **2014**, 270, 426-433.
78. Sharma, Y.; Sharma, N.; Subba Rao, G. V.; Chowdari, B. V. R., Studies on spinel cobaltites, FeCo<sub>2</sub>O<sub>4</sub> and MgCo<sub>2</sub>O<sub>4</sub> as anodes for Li-ion batteries. *Solid State Ionics* **2008**, 179 (15-16), 587-597.
79. Mohamed, S. G.; Chen, C.-J.; Chen, C. K.; Hu, S.-F.; Liu, R.-S., High-performance lithium-ion battery and symmetric supercapacitors based on FeCo<sub>2</sub>O<sub>4</sub> nanoflakes

electrodes. *ACS applied materials & interfaces* **2014**, *6* (24), 22701-22708.

80. Huang, Y.; Li, Y.; Hu, Z.; Wei, G.; Guo, J.; Liu, J., A carbon modified MnO<sub>2</sub> nanosheet array as a stable high-capacitance supercapacitor electrode. *Journal of Materials Chemistry A* **2013**, *1* (34), 9809-9813.

81. Li, B.; Feng, J.; Qian, Y.; Xiong, S., Mesoporous quasi-single-crystalline NiCo<sub>2</sub>O<sub>4</sub> superlattice nanoribbons with optimizable lithium storage properties. *Journal of Materials Chemistry A* **2015**, *3* (19), 10336-10344.

82. Kuang, M.; Liu, X. Y.; Dong, F.; Zhang, Y. X., Tunable design of layered CuCo<sub>2</sub>O<sub>4</sub> nanosheets@MnO<sub>2</sub> nanoflakes core-shell arrays on Ni foam for high-performance supercapacitors. *Journal of Materials Chemistry A* **2015**, *3* (43), 21528-21536.

83. Yamashita, T.; Hayes, P., Analysis of XPS spectra of Fe<sup>2+</sup> and Fe<sup>3+</sup> ions in oxide materials. *Applied Surface Science* **2008**, *254* (8), 2441-2449.

84. Yang, X.; Wang, X.; Zhang, Z., Electrochemical properties of submicron cobalt ferrite spinel through a co-precipitation method. *Journal of crystal growth* **2005**, *277* (1), 467-470.

85. Bao, F.; Zhang, Z.; Guo, W.; Liu, X., Facile synthesis of three dimensional NiCo<sub>2</sub>O<sub>4</sub>@MnO<sub>2</sub> core-shell nanosheet arrays and its supercapacitive performance. *Electrochimica Acta* **2015**, *157*, 31-40.

86. Wang, J.; Liu, S.; Zhang, X.; Liu, X.; Liu, X.; Li, N.; Zhao, J.; Li, Y., A high energy asymmetric supercapacitor based on flower-like CoMoO<sub>4</sub>/MnO<sub>2</sub> heterostructures and activated carbon. *Electrochimica Acta* **2016**, *213*, 663-671.

87. Wang, Q.; Wang, X.; Liu, B.; Yu, G.; Hou, X.; Chen, D.; Shen, G., NiCo<sub>2</sub>O<sub>4</sub> nanowire



arrays supported on Ni foam for high-performance flexible all-solid-state supercapacitors.

*Journal of Materials Chemistry A* **2013**, *1* (7), 2468-2473.

88. Wan, H.; Liu, J.; Ruan, Y.; Lv, L.; Peng, L.; Ji, X.; Miao, L.; Jiang, J., Hierarchical configuration of NiCo<sub>2</sub>S<sub>4</sub> nanotube@ Ni-Mn layered double hydroxide arrays/three-dimensional graphene sponge as electrode materials for high-capacitance supercapacitors.

*ACS applied materials & interfaces* **2015**, *7* (29), 15840-15847.

89. Zhao, Y.; Ma, H.; Huang, S.; Zhang, X.; Xia, M.; Tang, Y.; Ma, Z.-F., Monolayer Nickel Cobalt Hydroxyl Carbonate for High Performance All-Solid-State Asymmetric Supercapacitors. *ACS Applied Materials & Interfaces* **2016**, *8* (35), 22997-23005.

90. Yang, H.; Xu, H.; Li, M.; Zhang, L.; Huang, Y.; Hu, X., Assembly of NiO/Ni(OH)<sub>2</sub>/PEDOT nanocomposites on contra wires for fiber-shaped flexible asymmetric supercapacitors. *ACS applied materials & interfaces* **2016**, *8* (3), 1774-1779.

91. Dong, X.; Guo, Z.; Song, Y.; Hou, M.; Wang, J.; Wang, Y.; Xia, Y., Flexible and Wire-Shaped Micro-Supercapacitor Based on Ni(OH)<sub>2</sub>-Nanowire and Ordered Mesoporous Carbon Electrodes. *Advanced Functional Materials* **2014**, *24* (22), 3405-3412.

92. Xia, X.; Tu, J.; Zhang, Y.; Wang, X.; Gu, C.; Zhao, X.-b.; Fan, H. J., High-quality metal oxide core/shell nanowire arrays on conductive substrates for electrochemical energy storage. *ACS nano* **2012**, *6* (6), 5531-5538.

## VI. ACHIEVEMENT

### Publication

1. **Gao, H.**; Cao, S.; Cao, Y., Hierarchical core-shell nanosheet arrays with MnO<sub>2</sub> grown on mesoporous CoFe<sub>2</sub>O<sub>4</sub> support for high-performance asymmetric supercapacitors. *Electrochimica Acta* **2017**, *240*, 31-42.
2. **Gao, H.**; Xiang, J.; Cao, Y., Controlled synthesis of MnO<sub>2</sub> nanosheets vertically covered FeCo<sub>2</sub>O<sub>4</sub> nanoflakes as a binder-free electrode for a high-power and durable asymmetric supercapacitor. *Nanotechnology* **2017**, *28* (23), 235401. (Featured article)
3. **Gao, H.**; Xiang, J.; Cao, Y., Hierarchically porous CoFe<sub>2</sub>O<sub>4</sub> nanosheets supported on Ni foam with excellent electrochemical properties for asymmetric supercapacitors. *Applied Surface Science* **2017**, *413*, 351-359.
4. **Gao, H.**; Liu, S.; Li, Y.; Conte, E.; Cao, Y., A Critical Review on Spinel Structured Iron Cobalt Oxides Based Materials for Electrochemical Energy Storages and Conversions. *Energies*, accepted.
5. Chen, Y.; **Gao, H.**; Wei, D.; Dong, X.; Cao, Y., Langmuir-Blodgett assembly of visible light responsive TiO<sub>2</sub> nanotube arrays/graphene oxide heterostructure. *Applied Surface Science* **2017**, *392*, 1036-1042.
6. Chen, Y.; **Gao, H.**; Xiang, J.; Dong, X.; Cao, Y., Enhanced photocatalytic activities of TiO<sub>2</sub>-reduced graphene oxide nanocomposites controlled by Ti-O-C interfacial

chemical bond. *Materials Research Bulletin* 2017, in press, accepted.

7. Chen, Y.; Dong, X.; Cao, Y.; Xiang, J.; **Gao, H.**, Enhanced photocatalytic activities of low-bandgap TiO<sub>2</sub>-reduced graphene oxide nanocomposites. *Journal of Nanoparticle Research* 2017, 19:200.
8. **Gao, H.**; Li, Y.; Zhao, H.; Xiang, J.; Cao, Y., A general fabrication approach on spinel MCo<sub>2</sub>O<sub>4</sub> (M=Co, Mn, Fe, Mg, and Zn) submicron prisms as advanced positive materials for supercapacitor. Submitted to *Electrochimica Acta*, under review.

## Conference

1. **Gao, H.**; Cao, Y., Hierarchical core-shell nanosheet arrays with MnO<sub>2</sub> grown on mesoporous CoFe<sub>2</sub>O<sub>4</sub> support for high-performance asymmetric supercapacitors. 47<sup>th</sup> Annual WKU student research conference, March 2017, Bowling Green, KY.
2. **Gao, H.**; Cao, Y., A general fabrication approach on spinel MCo<sub>2</sub>O<sub>4</sub> (M=Co, Mn, Fe, Mg, and Zn) submicron prisms as advanced positive materials for supercapacitor. 2017 Kentucky Academy of Science Annual Meeting, November 2017, Murry, KY.

## Award

1. Western Kentucky University graduate student research grant, 2016.

2. McNally Outstanding Graduate Student Award, 2017, Chemistry Department, WKU.